10-18-2016

High Temperature Oxidation Study of Tantalum Carbide-Hafnium Carbide Solid Solutions Synthesized by Spark Plasma Sintering

Cheng Zhang
Florida International University, czhan009@fiu.edu

FLORIDA INTERNATIONAL UNIVERSITY

Miami, Florida

HIGH TEMPERATURE OXIDATION STUDY OF TANTALUM CARBIDE-

HAFNIUM CARBIDE SOLID SOLUTIONS SYNTHESIZED BY SPARK PLASMA

SINTERING

A dissertation submitted in partial fulfillment of

the requirements for the degree of

DOCTOR OF PHILOSOPHY

in

MATERIALS SCIENCE AND ENGINEERING

by

Cheng Zhang

2016

To: Interim Dean Ranu Jung
      College of Engineering and Computing

This dissertation, written by Cheng Zhang, and entitled High Temperature Oxidation Study of Tantalum Carbide-Hafnium Carbide Solid Solutions Synthesized by Spark Plasma Sintering , having been approved in respect to style and intellectual content, is referred to you for judgment.

We have read this dissertation and recommend that it be approved.

_____
Zhe Cheng

_____
Wenzhi Li

_____
Sudipta Seal

_____
Arvind Agarwal,Co-Major Professor

_____
Benjamin Bosel,Co-Major Professor

Date of Defense: Octobetr 18, 2016

The dissertation of Cheng Zhang is approved.

_____
Interim Dean Ranu Jung
College of Engineering and Computing

_____
Andrés G. Gil
Vice President for Research and Economic Development
and Dean of the University Graduate School

Florida International University, 2016

DEDICATION

I dedicate this dissertation to my wife and my parents. Without their unconditional love, support, and encouragement, it would have been impossible to accomplish this research.

ACKNOWLEDGMENTS

I would like to express my sincerest appreciation to my major adviser, Dr. Benjamin Boesl. Your intriguing ideas and excellent experimental skills make the high load in-situ indention testing possible. The technical suggestions you gave me have always been practical and constructive. You enthusiasm encourages me whenever I slow down on my research.

Special thanks to my co-major adviser, Dr. Arvind Agarwal, for instilling in me the qualities of being a good engineer and scientist. You always try you best to provide me with supports, both technically and financially. You always find time with your students even you are buried with administrative work.

I would like to thank my committee members, Dr. Zhe Cheng, Dr. Wenzi Li, and Dr. Sudipta Seal. Thank you for serving my PhD committee and providing invaluable suggestions throughout my PhD research.

I would like to acknowledge the supports from my research group members. Because of you, my last six years at FIU has been the most unforgettable time of my life. I am thankful to Drs. Anup Kumar Keshri, Debrupa Lahiri, and Srinivasa Rao Bakshi for training me on the lab equipment, providing guidance on research. Drs. Andy Nieto and Christopher Rudolf, you are trustworthy friends, you always have the answers whenever I need them. Ms. Laura Reyes and Melania Antillon, thank you for your time on editing my paper, I know that is not an easy task. Ms. Jennifer Bustillos, my dissertation will not be completed without your help on the schematic drawings. Ms. Archana Loganathan, thank you for the help on the oxidation tests. Mr. Pranjal Nautiyal, the technical discussion with you has always been inspiring.

ABSTRACT OF THE DISSERTATION

HIGH TEMPERATURE OXIDATION STUDY ON THE TANTALUM CARBIDE-

HAFNIUM CARBIDE SOLID SOLUTIONS SYNTHESIZED BY SPARK PLASMA

SINTEIRNG

by

Cheng Zhang

Florida International University, 2016

Miami, Florida

Professor Benjamin Boesl, Co-Major Professor

Professor Arvind Agarwal, Co-Major Professor

Tantalum carbide (TaC) and hafnium carbide (HfC) possess extremely high melting

points, around 3900 °C, which are the highest among the known materials. TaC and HfC

exhibit superior oxidation resistance under oxygen deficient and rich environments,

respectively. A versatile material can be expected by forming solid solutions of TaC and

HfC. However, the synthesis of fully dense solid solution carbide is a challenge due to their

intrinsic covalent bonding which makes sintering challenging.

The aim of the present work is to synthesize full dense TaC-HfC solid solutions by

spark plasma sintering with five compositions: pure HfC, HfC-20 vol.% TaC (T20H80),

HfC- 50 vol.% TaC (T50H50), HfC- 80 vol.% TaC (T80H20), and pure TaC. To evaluate

the oxidation behavior of the solid solutions carbides in an environment that simulates the

various applications, an oxygen rich, plasma assisted flow experiment was developed.

While exposed to the plasma flow, samples were exposed to a temperature of

approximately 2800 °C with a gas flow speed greater than 300 m/s. Density measurements

confirm near full density was achieved for all compositions, with the highest density measured in the HfC-contained samples, all consolidated without sintering aids. Confirmation of solid solution was completed using x-ray diffraction, which had an excellent match with the theoretical values computed using Vegard's Law, which confirmed the formation of the solid solutions. The solid solution samples showed much improved oxidation resistance compared to the pure carbide samples, and the T50H50 samples exhibited the best oxidation resistance of all samples. The thickness of the oxide scales in T50H50 was reduced more than 90% compared to the pure TaC samples, and more than 85% compared to the pure HfC samples after 5 min oxidation tests. A new $Ta_2Hf_6O_{17}$ phase was found to be responsible for the improved oxidation performance. Additionally, the structure of HfO_2 scaffold filled with molten Ta_2O_5 was also beneficial to the oxidation resistance by limiting the availability of oxygen.

TABLE OF CONTENTS

LIST OF TABLES

LIST OF FIGURES

Chapter I: Introduction

The objectives of this work are to synthesize fully dense TaC-HfC solid solutions, and evaluate their oxidation behavior using high temperature plasma flow which simulates rocket propulsion like conditions. This work is inspired by the study on the oxidation of Ta-Hf alloys, in which Ta melted during the oxidation and infiltrated the porous HfO_2 layer resulting in a dense, crack-free oxidation protective layer. The main oxidation product of TaC is Ta_2O_5, and it has a melting point around 1850 °C that is well below the application temperature. A similar liquid (Ta_2O_5) + solid scaffold (HfO_2) structure is expected which would provide exceptional oxidation resistance. This work presents an in-depth discussion on the formation of solid solutions as well as the analysis of the oxidation behaviors of the formed solid solutions under simulated environments.

1.1 UHTCs: Definition, Application, and Limitation

The materials for the next generation space transportation vehicles necessitate withstanding extreme conditions, such as high temperature, chemical reactivity, mechanical wear and stress, and radiation. Rapid heating/cooling rate, aggressive chemical/oxidizing environment or the combination of these conditions eliminates most of the current engineering materials for these purposes. Materials with improved mechanical properties, higher thermal shock resistance, and improved oxidation resistance are required to have satisfactory reliability and safety. Ultrahigh temperature ceramics (UHTCs) attract much interest for being potential candidate materials for the leading edges of the hypersonic reentry vehicles and lining materials of rocket thruster system. UHTCs is a

group of ceramics consisting of carbides, nitrides, and borides of the early transition metals. The meaning of the term "Ultrahigh temperature" is twofold. First of all, the ceramic itself should have a high melting point. As shown in the Figure 1.1, only a few materials have a melting point greater than 3000 °C. Secondly, the candidates should be able to withstand the chemical attack in the case of rocket thrust propellants; more importantly, the candidate's materials should have decent oxidation resistance at high temperature. The definition of high temperature is still vague, but empirically, temperature should be 2000 °C and above.[1-4]
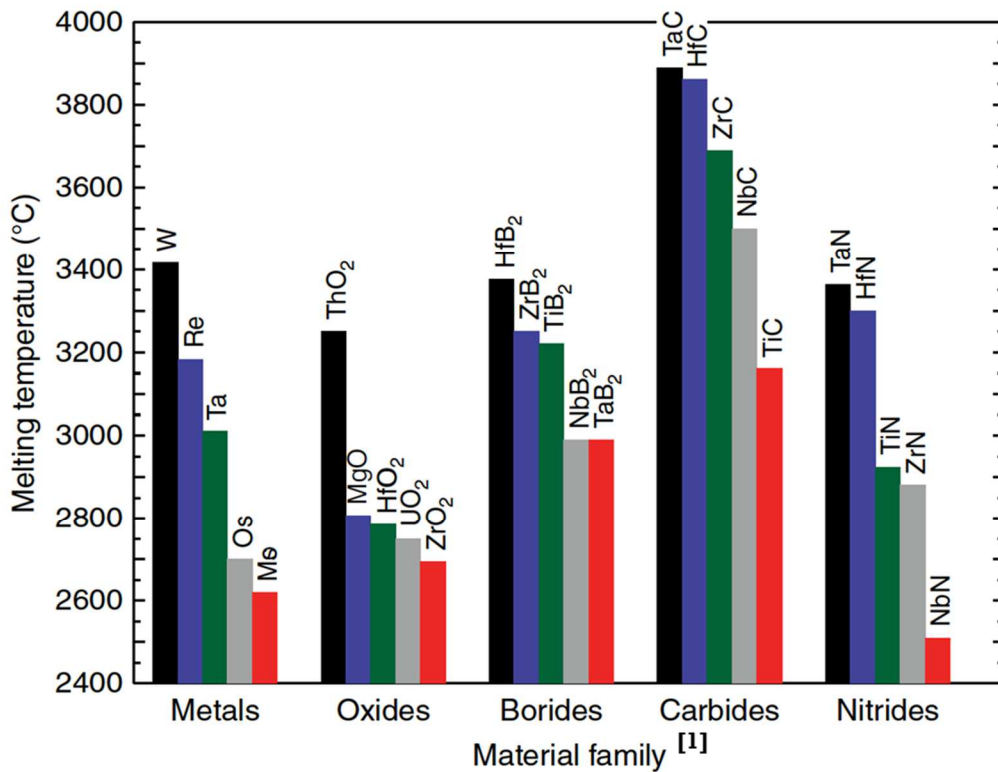
Figure 1.1: Materials with high melting points [1]

1.2 Why Tantalum Carbide and Hafnium Carbide

Tantalum carbide (TaC) has the NaCl-type structure (B1, Fm$\bar{3}$m). The carbon atoms are located at the octahedral interstitial sites. TaC has strong covalent bonding which results in an extremely high melting point of 3880 °C, high hardness, and high modulus. TaC can be used for the cutting tools, wear-resistance parts and rocket propulsion systems, but also has great potential in applications like leading edges of hypersonic vehicles. Some basic properties of TaC have been summarized in Table 1.1.[5, 6]

Table 1.1: Salient Thermophysical properties of Tantalum Carbide (TaC) and Hafnium Carbide (HfC)

	Tantalum carbide (TaC)	Hafnium carbide (HfC)
Melting point	3880 °C	3890 °C
Density	14.65 g/cm^3	12.8 g/cm^3
Crystal structure	FCC	FCC
Lattice parameters	4.44 Å	4.64 Å
Young's Modulus	486-560 GPa	423-500 GPa
Hardness	14.5-18 GPa	19 GPa
Fracture toughness	3.5-4.7 MPa.m$^{-0.5}$	2.5 MPa.m$^{-0.5}$

Hafnium carbide (HfC) has the same crystal structure as tantalum carbide with slightly larger lattice parameter as shown in Table 1.1 [5]. The properties of HfC are also comparable to those of TaC. Due to their similar crystal structure and size, TaC and HfC can form unlimited solid solution above 887 °C as observed in the TaC-HfC phase diagram shown in Figure 1.2.[7-11]
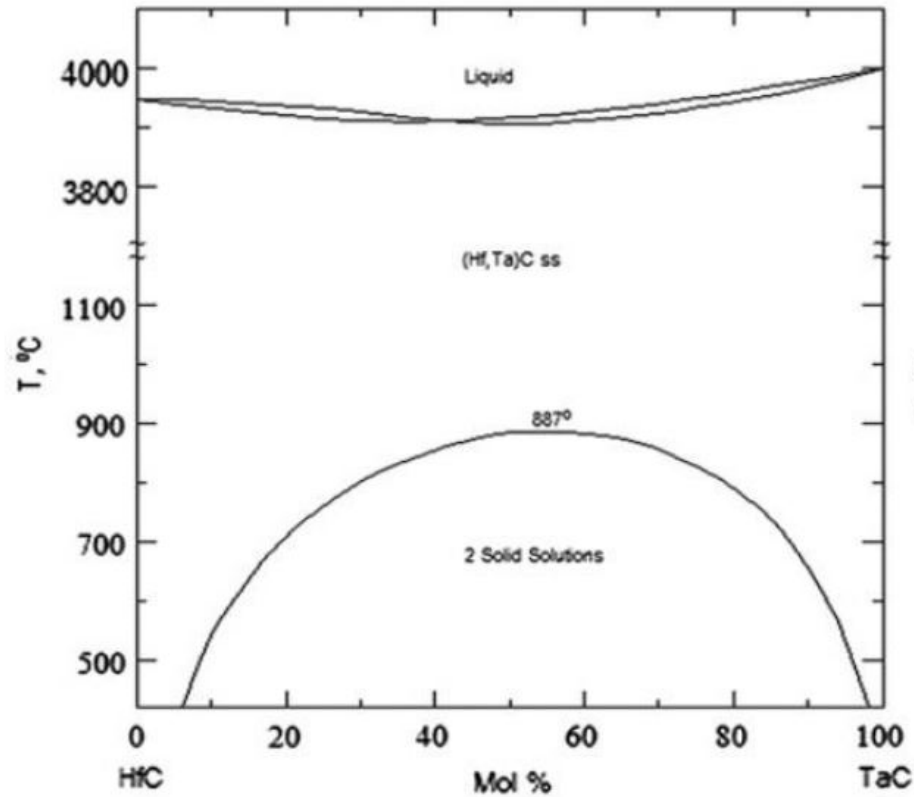
Figure 1.2: Phase diagram of TaC and HfC [7]

In the present study, we propose to combine TaC and HfC in order to achieve a new UHTC that has improved oxidation resistance as compared to pure TaC and pure HfC. The inspiration of this work is threefold. First of all, TaC and HfC have the highest melting points among the UHTCs as shown in Figure 1.1. The solid solution, $TaC_{0.8}HfC_{0.2}$, is arguably the highest melting point among known materials[12]. The strong hybridization of the Hf(Ta) 5d- and C 2p-like states might be the reason for this high melting point[13]. The high melting point enables the mixed carbides sample's survival under extreme conditions. Oxidation is another key factor for designing UHTC for ultrahigh temperature

applications. TaC has a relatively poor oxidation behavior[14-20]; it begins to oxidize at around 400 °C. The melting point of its oxide: Ta_2O_5 is ~1872 °C and will liquefy in oxygen rich environments[14]. However, when TaC is used in an oxygen deficient environment, such as an aluminized propellant solid rocket motor, TaC has been identified as the best performing ceramic lining material[21]. On the other hand, HfC has outstanding high-temperature oxidation resistance in oxygen rich environments. Hafnium dioxide (HfO_2) is stable, and it can form an oxycarbide interlayer during the oxidation process, which serves as an oxygen diffusion barrier and protects the un-oxidized carbide[22, 23]. By combining TaC and HfC, we expect to form a versatile ceramic solid solution that can serve in both oxygen concentration conditions. An early study on the high temperature oxidation behavior of Hf-Ta alloys suggested that the addition of Ta can enhance the oxidation resistance of Hf. The addition of molten Ta stabilized the HfO_2 oxide layer[24]. The resultant oxide layer then became dense and crack-free, and further oxidation was significantly restricted. Since Ta metal does not meet the requirement of UHTCs, TaC can be an excellent Ta source to achieve a dense oxide layer in the present study.

1.3 Oxidation Resistance Evaluation Methods

Different testing methods have been carried out to understand the UHTCs oxidation behavior under high temperature environments. Thermogravimetric analysis (TGA) and differential scanning calorimetry (DSC) are the two most common tests to understand the UHTCs thermal properties. Furnace oxidation tests have often been seen in the evaluation of the oxidation performance of UHTCs. Such tests are readily available and inexpensive. With controlled experimental conditions, such as static air flow and controlled gas

compositions, it is sufficient to recognize the fundamental knowledge of the oxidation mechanisms and provide crucial information on the initial screen of UHTCs. Since the real world application involves not only high temperature but also high velocity, the information obtained from furnace oxidation tests cannot fully predict the material oxidation behavior. Other approaches have been proposed to evaluate the oxidation performance under hypersonic flight conditions. The arc-jet test, laser test, and oxyacetylene torch test are the most popular testing methods.[1, 16, 17, 20, 25-27] Arc jet testing was developed and is widely used by NASA. Ionized atoms of oxygen and nitrogen accelerate to and recombine at the samples surface and release heat. It is designed to simulate the reentry conditions, especially the dissociation of air that occurs behind the bow shock at hypersonic speed for the space vehicles. Most of the arc-jet tests are performed on a flat surface or large-radius conical samples. Testing on shape leading edge geometries has started. However, due to the lack of understanding of the heat flux distribution, the tests have not been successful. The cost of these tests also prohibits it from being used in most studies.

The laser is an alternative heat source with a reasonable cost compared to the arc-jet testing. Laser tests use a prescribed heat flux exposed on a flat surface of the sample for a predetermined time. The test is usually accompanied by an external subsonic tangential gas flow to simulate the reentry dynamic conditions. The laser testing has a high testing efficiency; multiple samples can be tested in a short period. The temperature during the test can be accurately measured by optical pyrometry without the effect of a bright flame from other testing methods. The disadvantage of the laser testing is the difficulty in determining the actual heat flux absorbed by the samples. It varies with the compositions, wavelength

6

of the laser, and the temperature of the sample. To precisely interpret the results, the laser absorbance and emittance of each sample must be measured as a function of temperature. The literature which reports these properties is limited and the sample conditions can also affect the emissivity. The heat flux provided by the laser is constant which also deviates from the real world conditions.

Oxyacetylene torch testing has the lowest cost of the testing above methods. In this test, the sample is exposed to hot combustion gasses of an oxyacetylene flame. Only the temperature of the hottest section of the exposed sample is reported. The heat flux is not measured. The product of combustion, water, is present during the test, which adds the complexity of interpreting the results.

Aside from these common oxidation testing methods, our group started exploring the new testing methods using a plasma gun from plasma spraying system. Some success in the study of the tantalum carbide (TaC) oxidation behavior has been achieved[27]. In the plasma testing, a plasmas gun has been utilized as a heating source, and the setup is similar to the oxyacetylene torch testing. So the cost is still low. Unlike the oxyacetylene torch testing, no combustion reaction occurs during the plasma testing. Hence water is eliminated from the testing system. Similar to the arc-jet testing and combustion testing, the accurate measurement of the front side sample temperature will be challenging. However, since the plasma testing is initially designed for plasma powder spray, the temperature can be deduced from the temperature measurement of the in-flight particles, which has a well-developed measuring system. The correlation of the power input to the plasma spraying system and the resultant temperature has also been thoroughly studied. (The detailed front side temperature determining procedure will be described in the latter

chapter.) The temperature range of the plasma testing methods can go up to 5000K, which creates the opportunity to observe materials oxidation behavior under extreme conditions. The present work proves the feasibility of using the plasma gun as testing methods to evaluate the sample oxidation resistance.

1.3 Objective of the Current Research

1.3.1 Synthesize Fully-Densified TaC-HfC Samples Without Sintering Aids

Owing to the high covalent bonding and low self-diffusivity of TaC and HfC, sintering full, dense TaC and HfC is challenging[5, 28]. Consolidation methods like hot pressing, pressureless sintering, high-frequency induction heating, and spark plasma sintering are employed to sinter TaC and HfC. With the temperature over 2200 °C and several hundred mega Pascal pressure, sintering aids are still necessary. Sintering aids like carbon allotropes, disilicides, and carbides are used in TaC or HfC synthesis [10, 29-33]. Sintering aids additions can improve the overall densification that leads to better mechanical properties, and also introduces new secondary phases. Although secondary phases may not necessarily jeopardize the material properties, they increase the complexity of the system, limiting the actual understanding of the intrinsic properties. Based on this scenario, to fully understand the oxidation behavior of TaC and HfC mixed carbides samples, eliminating the sintering aids is necessary. Thanks to the previous experience in sintering tantalum carbide using spark plasma sintering (SPS), SPS will be chosen as the consolidation method. The parameters and starting powder treatment will be adjusted to synthesize the full, dense samples without sintering aids.

1.3.2 Understand the Oxidation Behavior of Sintered Samples Under the Simulated

Environment.

As mentioned in the previous text, a plasma gun from plasma spraying system will

be employed as the main heat source for oxidation tests. The temperature of the test is set

to be above 2500 $^{\circ}$C. This is one of the highest temperature tests among the oxidation

testing in the literature. The different predetermined length of time is to reveal the evolution

of oxide layers. Five compositions: pure TaC (PT), 80 vol. % TaC- 20 vol. % HfC

(T80H20), 50 vol. % TaC- 50 vol. % HfC (T50H50), 20 vol. % TaC- 80 vol. % HfC

(T20H80) and pure HfC (PH) are selected to cover the whole composition spectrum.

Oxidation behavior is interpreted from the weight changes, oxide layer thickness growth,

oxide layers phase information, the morphology of the oxide layers, and mechanical

properties of the oxide layers. In this study, not only the best oxidation performing

composition out of the five starting compositions will be identified, but also the oxidation

mechanisms will be proposed.

1.3.3 Predict the Optimum Composition of the TaC-HfC Mixed Carbides Samples for the

High Temperature Applications

Based on the oxidation mechanisms we proposed in the work, we can predict the

optimum composition for the high temperature application. The optimization criteria will

be the amount of oxide layer growth, the integrity of the oxide layer, and the mechanical

properties of the oxide layer. The optimum composition should have the least oxide layer

growth. Slow growth rate indicates good stability under high temperature environment.

The resultant oxide layer should be dense and well attached to the un-oxidized carbide so that the oxide layer could serve as a protective layer from oxidation. Mechanical properties assess the reusability of the materials. For reentry vehicles, the high temperature is not the only concern. With a hypersonic speed, any impact from debris would lead to catastrophic structural failure. A strong oxide layer is necessary for the space vehicle. Impact resistance can be evaluated by an in-situ indentation method and Nanoindentation technique. Both methods will be elaborate in the latter chapter.

Chapter 2 details the historic researches on the UHTCs oxidation performance, especially focuses on the hafnium carbide, tantalum carbide, and hafnium-tantalum carbides oxidation behaviors. Chapter 3 contains the materials and methods used in the present study. Results and detailed analysis of the present work can be found in chapter 4. Chapter 5 summarizes the major finding and contribution of the current work, and the future suggestions and work plan are included in chapter 6.

Chapter II Literature Review

2.1 Studies on the Oxidation of UHTCs

Although the term "Ultrahigh Temperature Ceramics" is relatively new, the research on UHTCs carbides and borides started in the late 1800s. In the end of the 1950s and early 1960s, the National Advisory Committee for Aeronautics (NACA) and its follow-on agency the National Aeronautics and Space Administration (NASA) recognized the need for new materials that could be used in rocket nozzles, atmospheric reentry vehicles, and thermal protection systems[1]. NASA began exploring possible materials that were suitable for the extreme conditions. The operating temperature for these applications was predicted to be between 2000-2400 $^{\circ}$C, in some cases, such as rocket motors, the temperature was discovered to go up to 3500 $^{\circ}$C. Oxidation resistance and the oxidized products are key factors when considering materials because hypersonic vehicles and rocket motors are exposed to an oxidizing environment with high temperature and pressure.

2.1.1 Oxidation Studies on the Si-Based Materials

The oxidation study on UHTCs began with SiC and Si_3N_4 in the late 1960s.[1, 34-55] Si contained materials have been employed as either thermal protection coatings on C-C composites or as additives modifying the oxidation resistance of C-C composites. The Si-based compounds possess exceptional oxidation resistance up to 1700 $^{\circ}$C. This is due to the formation of a layer of SiO_2 glass that can be served as a protective passive layer. The oxygen diffusion through this layer is limited, so the parent materials will be well protected from high temperature environments. However, when the environment temperature rises above 1700 $^{\circ}$C, the passive oxidation will convert to active oxidation and the main

11

oxidation product will become SiO (g). Furthermore, the decomposition of the SiO_2 and the reaction between SiO_2 and SiC at the interface at the higher temperature degrades the oxidation resistance and increase the ablation rate of Si contained materials.

2.1.2 Oxidation Studies on Metal Diborides

The investigation on the oxidation resistance of early transition metal diborides has been conducted. Oxidation tests were conducted with a temperature up to 2200 ºC. HfB_2 is identified as the material with most oxidation resistance followed by ZrB_2[6, 56-64]. A small research and development company called Manlabs, Inc. played a major role in carrying out the oxidation studies on UHTCs, especially on HfB_2 and ZrB_2. The projects began in the early 1960s and continued into the 1970s. The project was divided into 3 stages. The first stage was the initial material screening. Numerous metal diborides were selected and studied. The metals included Ti, Zr, Hf, Nb and Ta, and their diborides were considered as potential candidate materials for ultrahigh temperature applications. The thermodynamics, chemical, and physical properties were investigated and published. Among these diborides, HfB_2 and ZrB_2 were taken into further study due to their excellent oxidation rate. This was also the main perspective of the second stage. The relationship between oxidation behavior and boron-to-metal (B/Me) ratio, thermal conductivity, emissivity, and electrical resistivity was thoroughly deliberated. In the second stage, SiC was found to have beneficial effects improving diborides oxidation resistance. Carbon, on the other hand, was proven to have a positive effect on the material's thermal shock resistance. Further studies have identified the 20 volume percent of SiC as the optimal composition based on the mechanical properties and oxidation behavior. The addition of

SiC could also be beneficial to the materials densification by hindering the grain growth during the sintering process. Currently, it can be seen from Figure 2.1, the HfB_2-SiC system is still one of the most popular topics in UHTCs researches. The final stage of the study was focused on the material's response to the extreme environment, such as the flight conditions and reentry conditions of hypersonic vehicles. The goal of these studies was to correlate the laboratory test results from the previous studies with the simulated environments. In their tests, the laboratory testing was referred as the material-centric testing and the simulated testing was called the environment-centric testing. The materials that were considered in this stage of the study were pure diborides, diboride-SiC composites, C-C composites, graphite-based materials, and refractory metal-based materials. In all tests, the Hf contained samples that displayed slightly better oxidation performance than Zr compound. This might be due to the higher refractoriness of the HfO_2 compared to ZrO_2. The most promising results in both recession rate and reusability were achieved in Hf compounds with SiC additions.
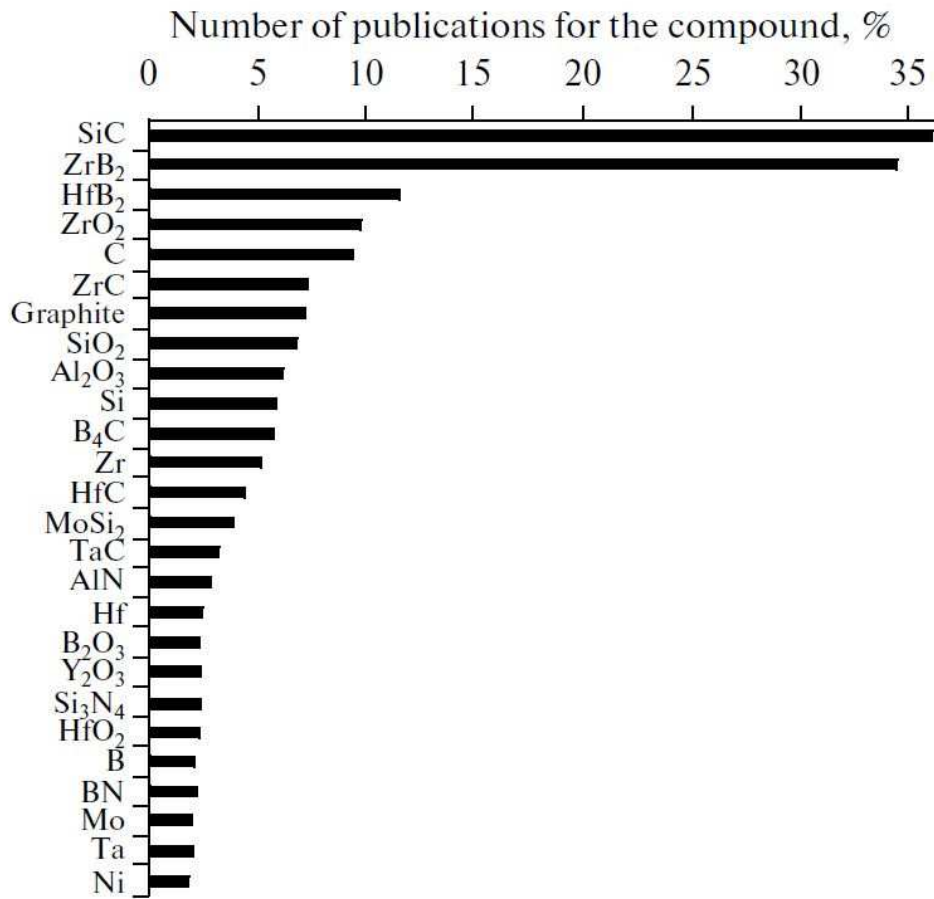
Figure 2.1: Distribution of publications on the UHTCs materials till 2013. [65]

2.1.3 Oxidation Mechanisms of Metal Diborides and Si Contained Materials

Detailed discussions on the oxidation mechanisms have been carried out by different researchers all over the world, and they have also established the guidelines for the future studies. Si contained materials have been extensively studied, and SiC is the most popular refractory carbide which can be seen in Figure 2.1. This is not only because SiC itself has superior oxidation resistance, but also because SiC can be used as an additive to other UHTCs to enhanced the oxidation performance [30, 66-77]. As just mentioned

before, HfB_2- 20 vol. % SiC has been confirmed the best oxidation performing sample to the date. The oxidation mechanism for this composites has been studied both thermodynamically and kinetically. [25, 60, 61, 70, 78-105]

When exposed to the high temperature, HfB_2 reacts with oxygen and forms HfO_2 and B_2O_3 as shown in Equation 2.1:

$$HfB_2 + O_2 \rightarrow HfO_{2(s)} + B_2O_{3(l)} \qquad \text{Eq. 2.1}$$
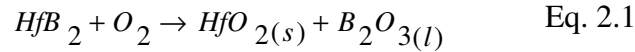
Since the melting point of B_2O_3 is only around 450 °C, the product boria formed as liquid because oxidation temperature is above 1000 °C. The melting point of hafnia is around 2800 °C, so the resultant oxide layer is a porous hafnia structure filled with the liquid boria. The liquid phase serves as an oxygen diffusion barrier and prevents further oxidation. The study shows that oxygen diffusion through boria liquid phase is the rate limiting step associated with oxidation of HfB_2 up to 1200 °C. Above this temperature, the oxygen is transported through the solid oxide, and the oxidation rate constant shows no dependency on oxygen partial pressure. Compared to carbides, boride samples will not generate gaseous products during the oxidation, which is also the main reason that the boride samples show better oxidation resistance. However, the evaporation of boria becomes significant at elevated temperatures. The evaporation of B_2O_3 can not only thin the protective liquid layer but also can disrupt the formed oxide layer and lead to further oxidation. The addition of SiC can improve composites oxidation resistance. Upon oxidation, SiC can form SiO_2, a much stable liquid glass phase; it can stabilize the liquid boria glass phase and form borosilicate glass phase. The reduction of oxidation rate was

observed above 1350 °C. This is because not enough of SiC oxidized when the temperature was lower than 1350 °C.

The microstructural analysis suggested the HfO_2 can provide a stable frame and the boria, silicate, and other glassy phases can fill the pores. Such structure displays outstanding oxidation performance until the glassy phases start evaporating.

2.2 Oxidation Behavior of Tantalum Carbide

The oxidation behavior of tantalum carbide has been investigated in the forms of coatings, additives, and bulk materials. The main oxide of TaC, Ta_2O_5, has a melting point of 1872 °C with two stable phases. The high temperature form, α-Ta_2O_5, has a monoclinic crystal structure with space group C121, (also some reports stated that α-Ta_2O_5 has a triclinic crystal structure.) The low temperature form, β-Ta_2O_5, belongs to space group C2mm which corresponds to the orthorhombic structure. The transition temperature between two phases is around 1320 °C. During the oxidation, tantalum carbide undergoes the following reaction:

$$2TaC + 9/2O_2 \rightarrow Ta_2O_5 + 2CO_2 \quad \text{Eq. 2.2}$$
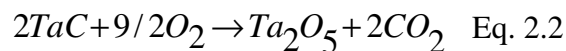
Due to the evolution of gaseous products and large Pilling-Bedworth ratio (2.47)[106], the formed oxide layer is not protective.

2.2.1 Isothermal Furnace Studies on the Oxidation Behavior of TaC

Desmaison-Brut et al. studied the oxidation behavior of hot isostatically pressed TaC and Ta_2C up to 850 °C[14]. The oxidation experiments were carried out in a lab

furnace with a dynamic flow of pure oxygen (5.6×10^{-3} L/s) at atmospheric pressure. Cubic samples were polished and washed before the testing, and a Setaram microbalance was used to monitor the weight changes. Kinetic curves were obtained by plotting the fractional weight change α ($\alpha = \Delta m / \Delta m_\infty$) versus time. The infinite weight gain Δm_∞ was considered the total conversion from TaC to Ta_2O_5 according to Eq. 1. Figure 2.2 was then acquired from the oxidation test with a heating rate of 17×10^{-3} °C/s.
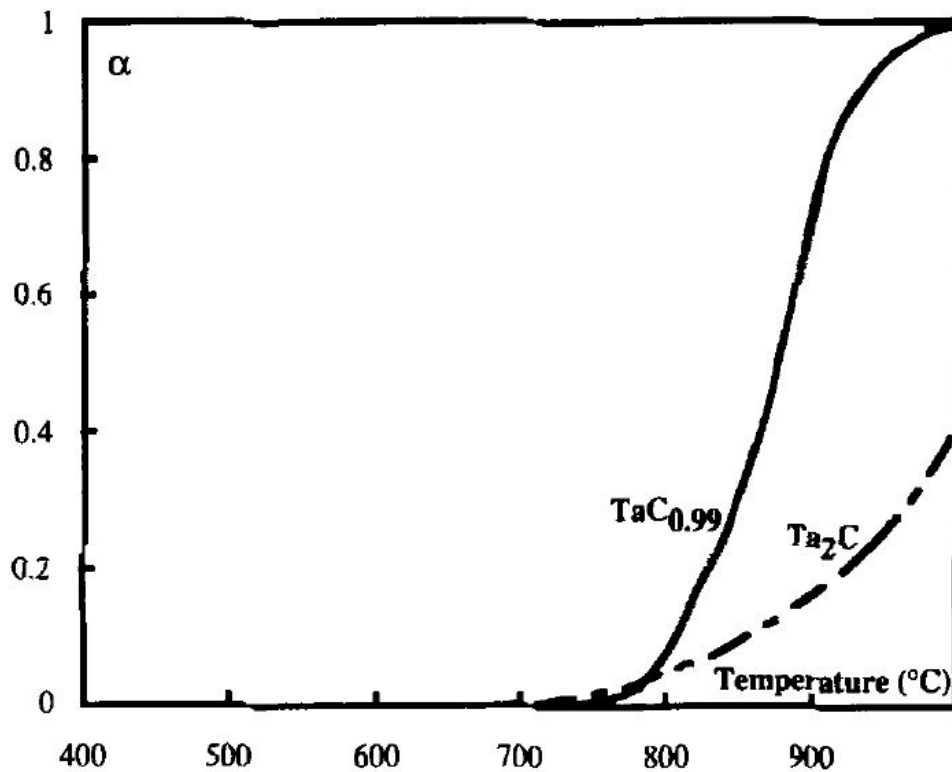
Figure 2.2: Non-isothermal oxidation curves for TaC and Ta_2C. [14]

TaC started oxidizing at the temperature of 700 °C and reached full oxidation at around 1000 °C. The oxide scale was identified as β-Ta_2O_5 by X-ray diffraction. Desmaison-Brut's work included tests that had a temperature range up to 850 °C (isothermal oxidation), whereas most the UHTCs application temperature is above 2000

17

°C. UHTC's application conditions are required to understand the oxidation behavior of tantalum carbide. Additionally, the microstructure information was lacking from his work. Due to the low sinterability, achieving fully dense TaC is always challenging. Different sintering receipts would lead into entirely different microstructures. A detailed characterization is crucial to understand the samples' microstructure properties.

Previous studies on TaC suggested its low sinterability and poor oxidation resistance, Additives were added into TaC system to serve as sintering aids, and reinforcement in both mechanical properties and oxidation resistance. Zhang et al. synthesized TaC-TaB$_2$ mixed ceramics using hot pressing[15]. 10 wt% (11 vol%) of TaB$_2$ was added as a sintering aid, and a final 98.6% relative density was achieved. Improved mechanical properties benefited from the higher densification. An oxidation study was conducted by TGA method in the air up to 1500 °C. The inspiration of TaB$_2$ addition was probably from the superior oxidation resistance of diborides which can form a B$_2$O$_3$ protective layer. Similar temperature versus weighing change curve was obtained as shown in Figure 2.3.
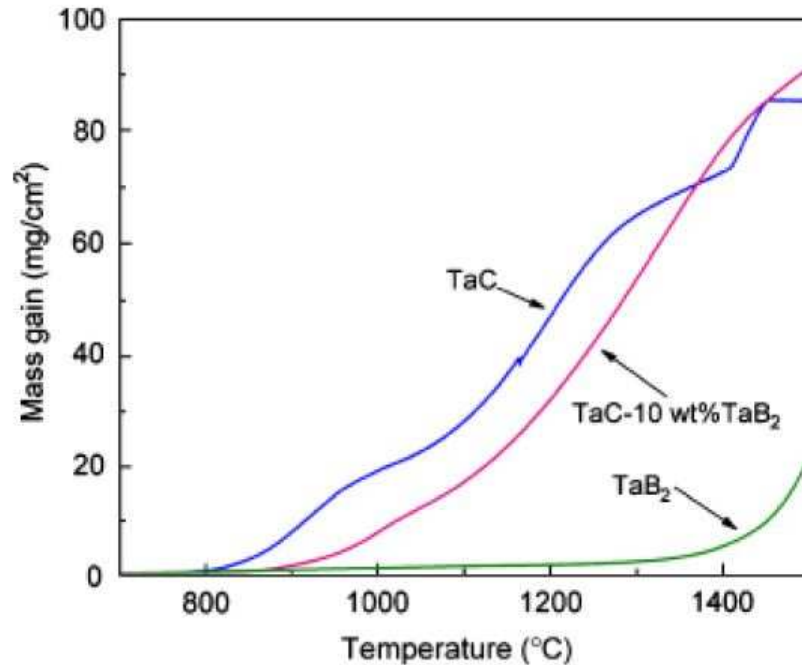
Figure 2.3: Temperature vs. weight change curves for TaC, TaC-TaB$_2$, and TaB$_2$. [15]

Monolithic TaB$_2$ displayed the highest oxidation resistance among the three samples in that study. The mechanism of this superior resistance has been investigated extensively for the diborides. However, oxidation resistance improvement in TaC-TaB$_2$ was only marginal to monolithic TaC. The formed B$_2$O$_3$ layer in the mixed carbides sample was insufficient to protect the carbides from oxidation. The gaseous products from TaC oxidation and maltase crosses resulted from the stress on the surface which provided the pathway for oxygen to penetrate the oxide layer. Aside from the diborides, disilicides were also studied as additives to TaC system. Sciti et al. selected TaSi$_2$ and MoSi$_2$ as reinforcing additives into TaC (TCT and TCM)[107]. The oxidation testing in this study was conducted in static air for 15 min at the temperature of 1600 °C. The XRD results found the only phase on post-oxidation samples was Ta$_2$O$_5$. There was no obvious difference between two

different disilicides, and nominal TaC oxidation results were not reported. The SEM of the fractured cross-section showed the Ta_2O_5 were embedded in a silica-based glassy phase which resulted from the oxidation of disilicides. The Ta_2O_5 and silica glass have immiscibility which caused the phase separation. The resultant Ta_2O_5 crystal presented a preferred 001 orientation. There are some studies that suggest the liquid phase separation caused by the immiscibility can increase the viscosity of the liquid, which can lead to a more stable protective layer against further oxidation. However, in Sciti et al. study, even though the testing temperature was highest among the oxidation study of TaC using lab furnace, the temperature was still not high enough to melt Ta_2O_5, and the protective multiphase layer was not observed.

2.2.2 Simulated Studies on the Oxidation Behavior of TaC

Lashtabeg et al. realized the necessity of higher temperature oxidation study, a series of simulated extreme conditions tests were carried out on pure TaC sintered pellets by an oxyacetylene torch[19]. The torch temperature in the tests was calculated at 3160 ^{o}C, the sample surface temperature was measured at 2100 ^{o}C, and the gas flow was recorded at 200 m/s. The testing conditions were much closer to the real application conditions compared to those testing inside the lab furnace, and the temperature was high enough to melt the Tantalum oxides. XRD results are shown Figure 2.4. The XRD profile in line (a) was taken from the area in the direct flame path. The temperature was estimated around 3000 ^{o}C in this area.
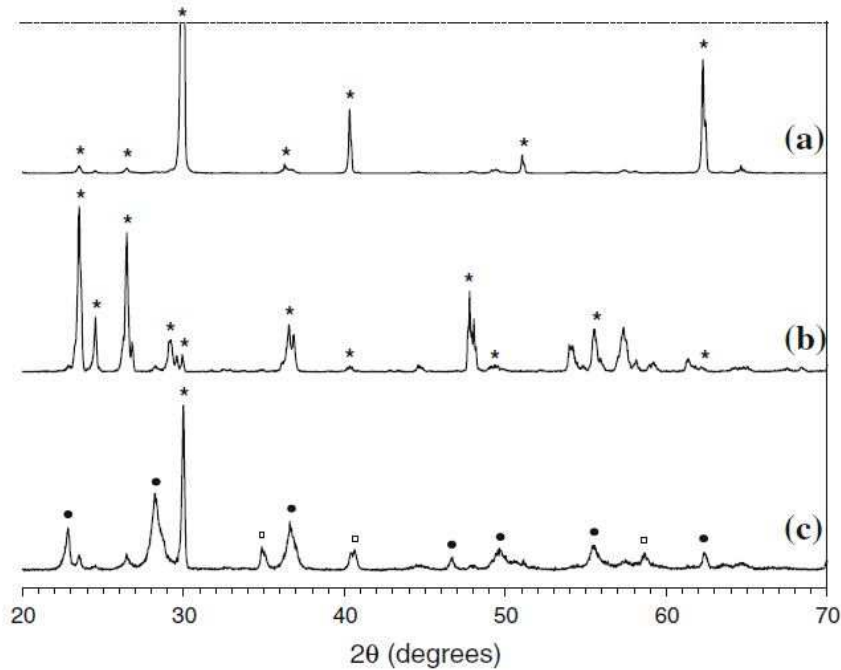
Figure 2.4: XRD results for different regions in the sample after oxidation tests. (a) In direct path, (b) Away from the direct path, (c) From the back side of the sample. (Open square: TaC, filled circle: β-Ta$_2$O$_5$, asterisk: α-Ta$_2$O$_5$.) [19]

As a result, the predominated phase was α-Ta$_2$O$_5$. Although α-Ta$_2$O$_5$ is stable only when the temperature is above 1320 $^{\circ}$C, the α-Ta$_2$O$_5$ was still detected. The transformation was reported as a slow process, and the α-Ta$_2$O$_5$ can be stabilized with other cation. In this case, samples were air quenched after the oxidation test. Large temperature difference led to a high driving force that accelerated the cooling process, and the carbon can be the cation source that can stable the α-Ta$_2$O$_5$ phase. The phases away from the flame direct path was detected mainly as β-Ta$_2$O$_5$ with some α-Ta$_2$O$_5$. In the back side of the sample, un-reacted TaC was detected after the oxidation tests. The existence of molten Ta$_2$O$_5$ was confirmed by the post oxidation SEM analysis. Moreover, the author found that the liquid phase that was formed could not serve as a protective layer, but instead it was attacking the carbides

21

during the oxidation. The author proposed that the metal (Ta) would react with oxygen first, and formed Ta_2O_5 would melt and surround the TaC surface. When the temperature was above 2500 ^oC, the reaction between TaC and Ta_2O_5 becomes favorable and generates tantalum oxycarbide. Further oxidation would transform the oxycarbides into oxides and gaseous products. Paul and his team conducted the oxyacetylene oxidation test on the TaC at almost the same time. The variable in this oxidation testing was the standoff distance from the oxyacetylene torch to the sample. As a result, the peak temperature on the sample surface decreased with increased standoff distance. The highest temperature was measured at 2300 ^oC with a 10 mm standoff distance. Temperatures of 2190 ^oC and 1990 ^oC were measured at 15 mm and 20 mm distance respectively. Two phases, α-Ta_2O_5 and β-Ta_2O_5 (Note: The α-Ta_2O_5 phase in Paul's work was described as a triclinic structure.[26]) were also observed in the XRD analysis from the post-oxidation samples. However, unlike the XRD in the Lashtabeg et al. work, where all peaks belonged to α-Ta_2O_5 in the region exposed to flame directly, the XRD in Paul et al. work showed the mixture of both oxide forms. This may be because the peak temperature in Paul et al. was lower than the one in Lashtabeg's work. This means that the cooling rate was not high enough to preserve the α-Ta_2O_5 form. Delamination of the oxide layer from carbides was observed in Paul's work, which is contributed to the gaseous products and thermal mismatch. The formation of tantalum sub-oxides, including TaO_2 and Ta_2O_3 were also concluded. Big cracks on the samples were noticed. This was due to the stress concentration introduced by screws which were used to hold the sample. The large opening not only enhanced the oxygen inwards flow, but also disturbed the thermal gradient of the sample. A fixture without stress concentration is also critical to a successful oxidation test.

2.2.3 Ablation Evaluation of TaC

Aside from the oxidation testing on the bulk tantalum carbide, ablation evaluation on the TaC as a form of the protective coating has also been conducted. Wang et al. decided to fabricate a uniform, dense, and crack-free TaC coating to provide enough protection.[16] The TaC coating was plasma sprayed on SiC coated C/C substrate. The ablation tests were conducted using an oxyacetylene torch with three different temperatures: 2100, 1900, and 1800 $^{\circ}$C. No new mechanism has been noticed in this study. The best protection was found in the 1800 $^{\circ}$C test since the temperature was below the melting point of tantalum oxide. Higher temperature resulted in liquefied Ta_2O_5 that was blown away during the test and failed to protect the beneath substrate. Owing to its poor oxidation performance of tantalum carbide under the simulated oxidation tests, few studies proposed using reinforcing additives like CNT, SiC, disilicides, and graphene to enhance the TaC oxidation resistance under the simulated conditions. In our previous work, we incorporated graphene nanoplatelets (GNP) with TaC powder, followed by the consolidation using spark plasma sintering (SPS) to achieve near fully dense TaC-GNP composites.[27] The composites were exposed to a high temperature plasma flow of above 2500 $^{\circ}$C. The high temperature plasma flow was created by a SG-100 plasma gun using in plasma spraying system. Compared to the more commonly used oxyacetylene torch, the high temperature plasma flow provides high heat and gas flow without generating byproducts, such as water, which may affect the interpretation of the oxidation performance. The oxidation results showed that the addition of GNP suppressed the oxidation layer formation up to 60%. The addition of GNP was found to be beneficial to the samples' thermal conductivity. As a result, the heat was dissipated more easily from the most intense heating zone, which provided less

energy for the oxidation of TaC. The GNP was visually spotted from the post-oxidation SEM analysis, which suggests its survival from the harsh environment. Moreover, the GNP was proven to be an excellent oxygen shield since it laid at the grain boundaries of TaC. The predominated oxygen diffusion pathway was through grain boundaries, the existence of GNP stopped the oxygen penetration and prevented further oxidation. Very recently, Nisar et al. explored the effects of CNTs, SiC and CNT-SiC additions on the oxidation behavior of TaC under the extreme conditions using plasma torch.[20] Both CNTs and SiC have been proven effective in dissipating the heat away from the hottest zone due to their superior thermal conductivities. The oxidation onset temperature shifted towards higher temperature in TaC-CNT-SiC composite than the monolithic TaC, and the enthalpy of oxide formation decreased compared to TaC. Both observations suggested synergetic reinforcement of SiC and CNT in improving the oxidation resistance of TaC. Disilicides were also employed in reinforcing the oxidation resistance of TaC. The most common disilicides including $MoSi_2$ and $TaSi_2$. Although the experimental methods vary, the results were always as anticipated. The molten Ta_2O_5 cannot provide enough protection and has a high ablation rate. However, the multiphase oxide layer of Ta_2O_5-SiO_2 showed much-improved oxidation resistance. The gaseous products and thermal stresses lead to the delamination of the oxide layer and jeopardize the integrity of the whole sample.

2.2.4 TaC Oxidation Performance in the Rocket Engine Application

After extensive researches on the oxidation performance, TaC does not show promising oxidation resistance under the extreme conditions. However, when it comes to

the aluminum burning rocket engine, tantalum carbide was found to be the best performing lining materials. The candidate materials for such applications should withstand not only high temperatures but also the chemical attacks from the molten alumina. This is the main product of an aluminum burning rocket engine. The thermodynamic calculation showed that the onset temperature of the reaction between TaC and Al_2O_3 occurs around 3000 °C. That is 400 °C higher than hafnium carbide. So tantalum carbide can provide a thermally and chemically stable aluminum burned engine. [21]

2.3 Oxidation Behavior of Hafnium Carbide

There are more precedent studies on the oxidation of hafnium carbide than on oxidation of tantalum carbide. This is probably because the resultant oxide: HfO_2 is a much more stable oxide, so the hafnium carbide presents relatively good oxidation resistance under extreme conditions. Hafnium oxide has an extremely high melting point at around 2800 °C and low vapor pressure. There are three main phases for HfO_2: monoclinic, tetragonal, and cubic. The transition temperatures are 2100, 2793, and 3073K, respectively. The Pilling-Bedworth ratio for hafnium to hafnium oxide is 1.62. Such promising properties make HfC a potential candidate material for UHTCs applications.

2.3.1 Kinetics Studies on the HfC Oxidation Process and Counter-Current Gaseous Diffusion Model

The systematic studies on the oxidation of hafnium carbide began with Courtright et al. work.[108] In their work, hot-pressed hafnium carbide pellets underwent a serial of

oxidation tests with temperatures up to 2200 °C. Thermogravimetric analysis (TGA) was applied to the oxidation temperature from 1200-1530 °C, and a laser heating apparatus was used to conduct the oxidation testing from 1800-2200 °C. (Note: The oxidation temperature was high enough to be considered as ultra-high temperature. However, because there was no strong gas flow, the laser was used purely as a heating source, this series of oxidation tests cannot be considered as simulated testing.) Parabolic growth kinetics were observed for HfC over the entire temperature range so that the growth kinetics can be described by the expression:

$$R = k_p t^{1/2} + R_0 \qquad \text{Eq. 2.3}$$

Figure 2.5 shows the temperature dependence of the oxide growth constant for HfC. A break in the curve was observed at around 1800 °C. Two growth constants were provided for two temperature ranges:

For T= 1473-2073 K, $\qquad k_p = 4.83 \times 10^{-4} \exp(716/T(K))$ cm/s$^{1/2}$

For T= 2073-2473 K, $\qquad k_p = 0.05 \exp(-13700/T(K))$ cm/s$^{1/2}$

After examination of the morphology of post-oxidation samples, pores and cracks were spotted. The oxidation temperature was above 2100K, which is the transition temperature for HfO_2 transforming from monoclinic to tetragonal. The formed HfO_2 was supposed to experience phase transformation accompanied by modest volume change, 12.7% expansion. However, the cracking patterns on the oxidized samples above and below this transition temperature did not display significant difference, suggesting that this transformation was not a major reason for the crack. In fact, at 1700 °C, the plasticity should be able to accommodate the stress caused by the phase transformation.

Another significant contribution from this report was the introduction of a counter-current gaseous diffusion model that describe the oxidation behavior of hafnium carbide. The more detailed description was reported by Holcomb et al. in a separate document.[22] The resultant hafnia scale was observed as a porous layer with interconnection pores. Those interconnected pores provided a pathway for the inward diffusion of oxygen and outward diffusion of CO. At oxidation testing temperature, the CO and O_2 gasses were not compatible and formed CO_2. This reaction created a gas sink (flame front) that resulted in a new gas flow from both sides of the flame front. Figure 2.5 illustrates the chemical reactions, and gas flows at both sides of flame front.
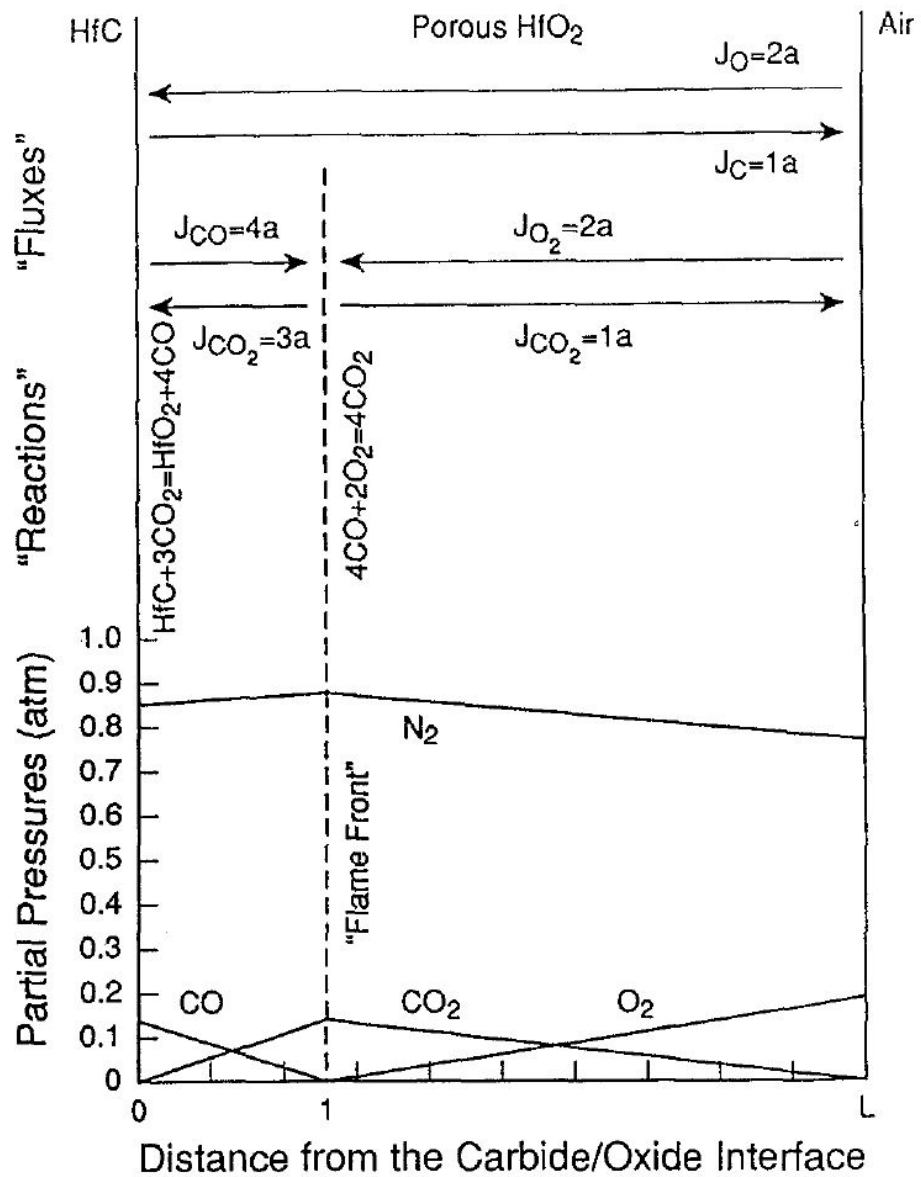
Figure 2.5: Gas flows, reactions, and partial pressures of O_2, CO, and CO_2 across hafnia scale during the oxidation of HfC at 1400 °C. [22]

An approximation of the Stefan-Maxwell equation was adapted to calculate the gaseous concentration profiles across both regions of the porous hafnia scale. The model investigated the effects of porosity, tortuosity, and gas-wall interactions. The predictions on parabolic rate constants in the case of a porosity of 2% and a pore radius of 0.01 μm

28

hafnia scale were close to the constants obtained from the thermogravimetric analysis. Both predicted and measured parabolic rate constants had the same dependence on temperature and oxygen partial pressure.

2.3.2 The Discovery of the Hafnium Oxycarbides Layer

Bargeron et al. conducted the oxidation study on hafnium carbide in the temperature range 1400 ºC to 2060 ºC inside an induction furnace with the gas composition of 93% of argon and 7% oxygen. In their study, three distinct layers were observed.[109] Besides the outermost oxide and inner residual carbide layer, a dense, crack-free interlayer was spotted, which later was confirmed as hafnium oxycarbide. It is a unique feature of hafnium carbide, and it can absorb oxygen into its lattice without disturb the crystal structure. The study showed that the amount of dissolved oxygen could up to 30%. A moving boundary model was also introduced in this study, and a schematic is shown in Figure 2.6.
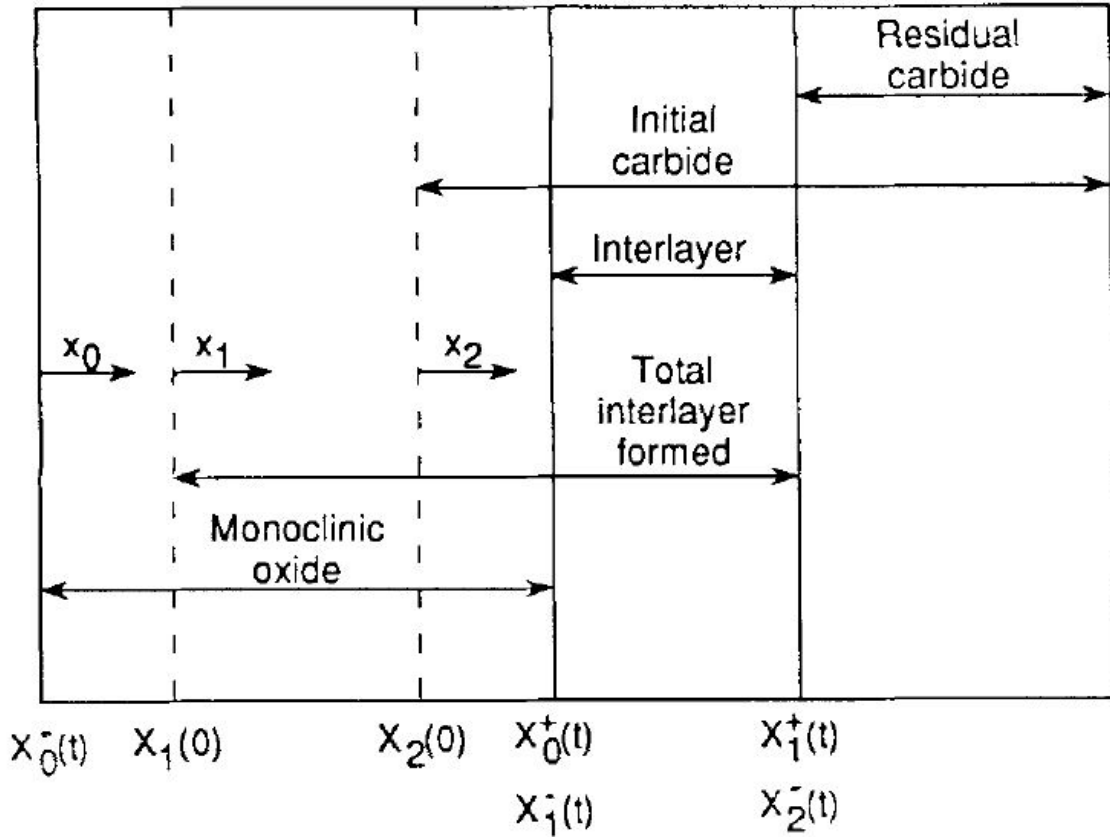
Figure 2.6: Schematic of the moving-boundary model. The subscript "0, 1, 2" represented oxide layer, interlay oxycarbide, and residual carbide layer, respectively. "t" indicated the reaction time. Superscript "+ and -" suggested the growth or recession in layer thickness. [109]

The schematic is self-explanatory, the subscript "0, 1, 2" represents oxide layer, interlay oxycarbide, and residual carbide layer, respectively. "t" indicates the reaction time. Superscript "+ and -" suggestes the growth or recession in layer thickness. The model neglected only the inward diffusion of oxygen, and the oxidation process follows: carbide → oxycarbide → oxide. Oxygen diffusion constants were calculated at a temperature of 1400 °C and 2060 °C; the results showed that the oxygen diffusion in interlayer oxycarbide was one magnitude lower compared to in oxide layer, and more than two magnitudes lower

than in carbide layer. Oxycarbide layer was the main reason for exceptional oxidation performance of HfC as a protective layer against oxidation.

Shimada et al. carried out a series of hafnium carbide oxidation studies in the temperature range of 480 $^{\circ}$C to 600 $^{\circ}$C, and 600 $^{\circ}$C to 900 $^{\circ}$C.[110, 111] In the temperature range of 480 to 600 $^{\circ}$C tests, three oxygen partial pressures were selected: 4, 8, and 16 kPa for isothermal oxidation tests. The results showed that after the initial rapid oxidation with the formation of oxycarbide, the oxidation process could be divided into three stages: (1) diffusion controlled oxidation, (2) phase-boundary controlled process. The activation energies for both stages were the same (~197 kJ·mol^{-1}), and (3) chemical-reaction controlled stage. In the first stage, oxide layer build up at the surface. With the progress of the oxidation, the grains located near the surface area formed a thicker layer of oxides compared to those remote from the surface. When the oxide layer grew thick enough (10 % of the grain size), stress accumulated cracked the oxide layer and provided an easier pathway of oxygen diffusion. This was the sign of the beginning of the second stage oxidation. The newly exposed grains started to oxidize and create a cycle of cracking-rebuilding. Thus, the hafnia scale was a compact but cracked layer. The authors observed that both the oxygen/compact HfO$_2$ interface and HfO$_2$/oxycarbide interface moved at the same speed, which led to a constant thickness of diffusion layer. The time-independent thickness introduced the last stage of the oxidation, chemical-reaction controlled stage. It also appeared that the evolution of gasses did not contribute to the cracked hafnia scale significantly. If all of the carbon was consumed into gaseous products the final weight gain should have been 130 %. However, none of the tests weight gain percentage was close to 130%. This results indicated the retention of carbon. The oxidation temperature in this

work was relatively low; the authors suspected the oxygen potential at the interface between HfO_2 and oxycarbide phase was lower than the oxygen potential in equilibrium with carbon, CO, and CO_2. This differs from other literature where researchers claimed that in order for CO to have a destructive effect on the oxide layer temperature should be as high as 1730 $^{\circ}$C. Unfortunately, in the UHTCs applications, 1730 $^{\circ}$C is considered low. This is the main reason that HfC is not a favorable candidate material to use on the space transportation vehicles, even HfO_2 is a protective oxide layer. However, in our present work, the results indicated otherwise. Detailed discussion can be found in Ch. 4.

2.3.3 Other Isothermal Oxidation Studies of Hafnium Carbide

Later Shimada et al. investigated the isothermal oxidation of HfC single crystals with (100) orientation at temperature 600 to 900 $^{\circ}$C and an oxygen pressure of 2 to 8 kPa for up to 180 h. Two zones were found in the oxide scale, zone 1 and zone 2. Zone 1 was dense and pore-free. This zone contained twice the amount of carbon than zone 2. The thickness of this zone remained constant even after prolonged exposure. Zone 2 was identified as hafnium oxide layer. This layer contained many pores and cracks as observed in the other hafnium carbide oxidation study. The description of this layer matched the characteristics of the oxycarbide layer that can be observed by the previous researchers. It seemed that the formation of the oxycarbide layer is an inevitable step of the hafnium carbide oxidation process. It was widely accepted that the hafnium carbide can dissolve oxygen at its carbon site which was accounted for the formation of this oxycarbide layer. Nevertheless, the carbon retention was observed by multiple researchers. It was proposed

that if the local oxygen potential was low at the carbide surface at relatively low temperature, the oxidation of hafnium carbide became a "displacement reaction" between hafnium carbide and oxygen and formed the amorphous carbon and hafnium oxide. Noted that the carbon content was measured higher than in oxide layer in all the studies. So the retention of carbon is also essential to the formation of oxycarbide.

2.3.4 Simulated Oxidation Studies on the Hafnium Carbide

Savino et al. compared the oxidation behavior of HfB_2 and HfC reinforced by $MoSi_2$ using arc-jet testing.[58] The use of $MoSi_2$ was inspired by its oxidation product: SiO_2 glass phase which can serve as a protective layer. 5 volume percent of $MoSi_2$ was added. The experimental temperature exceeded 2000 ^{o}C. Three different layers of oxides were found. The outer layer displayed silica-based glassy phase partially filled hafnium oxide. The intermediate layer consisted of hafnium oxide layer with fine porosity, and isolated pockets of molybdenum oxide were also observed. The inner layer contained partially oxidized HfC and SiC, and residual Mo-Si species. Unlike the oxidation of HfB_2 from which a continuous glassy layer can be found, such continuous layer was not found in the HfC oxidized layers. It was suggested by the author(s) that the CO formed during the oxidation of HfC reacted with $MoSi_2$ and released the volatile SiO gas. The oxycarbide-like layer mixed with SiO_xC_y was also observed. However, the detailed mechanisms are yet to be understood.

2.3.5 Oxidation Studies of HfC as Protective Coatings

A series of oxidation studies of HfC as a protective coating were reported in the last five years. The C/C was selected as substrate materials in those studies. SiC was another popular material in the oxidation of protective coating studies. Both HfC and SiC can be found as matrix or additive to the other. A study on 2D and 3D structure multilayers coating was also reported.[112] Despite the coating preparation, compositions, thickness, testing methods, testing conditions varied, the main oxidation mechanisms of HfC-SiC coating were basically the same. It was widely reported that the porous hafnium oxide could provide a frame for the glassy SiO_2, this layer would slow down the oxidation process by limiting the oxygen diffusion.

2.4 Oxidation of TaC-HfC Mixed Carbides

The research interests began on the oxidation study of Hf-Ta metallic alloys. The addition of Ta melt during the hafnium oxide and formed a dense, crack-free oxide layer. In the early 1960s, the study on the vaporization of TaC-HfC solid solution has been reported. [113]The results indicated that among all the compositions, 80-mole percent of TaC and 20-mole percent of HfC showed the lowest volatility or a maximum stability at the temperature range of 2500 to 3000 K. In the other report, the melting point of this composition was found to the highest among the known materials. [12] Although this result cannot be reproduced by other researchers, the melting point of TaC and HfC are the highest among the UHTCs ceramics, it is worth investigations. In the second part of Courtright et al. oxidation of HfC work, 25 wt% TaC was added, and same oxidation study

with the temperature up to 2200 ℃ was performed.[108] This work was directed inspired by the Hf-Ta metallic alloys according to the authors. However, the results suggested otherwise. Instead of a dense, crack-free oxide layer, the resultant oxide scale was porous, the surface of the scale was ragged and irregular. The porous structure was due the evolution of the gaseous products. Five thermal cycles were also performed between 2000 ℃ and 500 ℃ on pure HfC and HfC-TaC sample, the post-SEM analysis showed the HfC oxide scale was intact while the mixed carbides oxide scale was spalled and porous, and it was almost double in thickness compared to pure HfC.

Due to the military interest of this sample, and partially due to the Courtright report, literature on TaC-HfC mixed carbide system and their oxidation studies are limited.

In 1996, NASA reported an oxidation study on TaC-HfC film prepared CVD methods. [114]Three compositions were selected, HfC-10, 20, 30 wt% TaC. The oxidation tests were carried out in air, in a tube furnace at 1000 ℃ and 1200 ℃. Higher temperature tests were conducted by an oxyacetylene torch, with no temperature information provided. The results showed that the overall oxide scales were well attached to the substrate after 8 hours oxidation tests, but severe cracking was noticed. In the oxyacetylene oxidation tests, except for the HfC-20 wt% TaC sample, the rest two were intact for 5 min tests. The HfC-20 wt% TaC sample was cracked and flaked away totally. Later in 1999, another report was published. [115]Two carbides were again co-deposited on a graphite substrate by CVD then annealed for 2 hours at 1600 ℃ to obtain the solid solution (Such annealing process was not mentioned in the 1996 report). The oxidation testing was performed by an oxyacetylene torch at a temperature of 1750 ℃. The 1-22 vol % TaC was chosen for the

oxidation testing. The results indicate a trend towards more oxidation and more spalling with increasing TaC content.

So far, the oxidation testing on TaC-HfC mixed carbide system did not show any promising improvement. Since hafnium carbide showed relatively good oxidation resistance and low volatility, it was also selected as the matrix material, and TaC was chosen as an additive. In the Courtright et al. work, HfO_2 and a mixed oxide, $Ta_2Hf_6O_{17}$ was identified by XRD after oxidation. Hafnia was a well-studied oxide, but the properties of $Ta_2Hf_6O_{17}$ are yet to be determined. Since it is a mixture of Ta_2O_5 and HfO_2, its melting point should be between two oxides. $Ta_2Hf_6O_{17}$ can also be considered as Ta_2O_5-$(HfO_2)_6$, so the melting point should be closer to HfO_2 side, as in the HfO_2-ZrO_2 system, melting point of this compound increases with the increasing HfO_2 content due to the higher melting point of hafnia than zirconia. Based on this discussion, more studies on $Ta_2Hf_6O_{17}$ should be carried out.

Wang et al. conducted the similar ablation testing on co-deposited TaC-HfC coating. [116]The ratio of Ta/Hf is 1:3. The coating was identified as the mixture of HfC and $HfTaC_2$. The ablation testing was using an oxyacetylene torch for 1 min. The results indicated the $HfTaC_2$ could promote the formation of a dense oxide layer, $Ta_2Hf_6O_{17}$ was indexed by XRD and showed outstanding ablation performance. Ghaffari et al. pressure-less sintered $Ta_{0.8}Hf_{0.2}C$ solid solution with the addition of $MoSi_2$ as a sintering aid. [10]They also conducted the oxidation tests on this solid solution using an oxyacetylene torch. Double layered oxide scale was found, and both layers were protective against oxidation. The outer layer comprised mainly $Ta_2Hf_6O_{17}$ and the inner layer is a diffusion barrier based on Ta-Hf-Mo oxycarbide. This test results predicted the potential of TaC-

HfC oxidation resistance. However, the content of MoSi$_2$ was relatively high (24 vol.%) that prevented the true mechanisms of TaC-HfC oxidation behavior. TaC-HfC solid solution samples without sintering aids would be the ideal sample to study their oxidation behaviors.

2.5 Summary

From the oxidation behavior of diborides system and the oxidation behavior of HfC and TaC, an oxide scale with a stable frame filled with glassy phase is found to be the ideal structure for the high temperature applications. Tantalum oxide has a low melting point, and hafnium oxide is a stable oxide phase. The TaC-HfC solid solution has great potential for high-performance oxidation materials. Studies on the oxidation behavior under the extreme conditions are needed. Hence, the present work will focus on the oxidation of fully dense TaC-HfC solid solutions under the simulated conditions.

Table 2.1: Literature review summary of the oxidation studies of TaC, HfC, and TaC-HfC

Tantalum carbide

Material	Preparation methods	Oxidation testing conditions	Lab furnace testing(L) or Simulated testing (S)	Main oxide phases	Morphology	Remark	Reference
TaC	HIP	750-850 ºC, Atm, O_2 flow= 5.6×10^{-3} L/s	L	β-Ta_2O_5	Maltese cross, cracks	No oxycarbide found	[14]
TaC, TaC-10 wt.% TaB_2	HIP	TGA in air up to 1500 ºC	L	Ta_2O_5, B_2O_3	Non protective scale	TaB_2 did not improve oxidation resistance significantly	[15]
TaC- 15 vol. % $TaSi_2$, TaC-15 vol.% $MoSi_2$	HIP	In air 1600 ºC for 15 min	L	Ta_2O_5	Maltese cross, cracks	Badly oxidized with cracks. No noticeable difference between $TaSi_2$ and $MoSi_2$	[117]
TaC-coated SiC/C-C substrate	Plasma spray	1800, 1900, 2100 ºC in air for 60 s with an oxyacetylene torch	S	Ta_2O_5, SiO_2	Ablation pit	Coating will be broken through rapidly if the temperature higher than the melting point of Ta_2O_5	[16]

TaC	HIP	3160 ºC in air with a flow velocity of 200 m/s with an oxyacetylene torch	S	β-a$_2$O$_5$, α-Ta$_2$O$_5$	Porous, liquid phase formed with TaC island floated,	A 4-step oxidation process was proposed, including the initial Ta$_2$O$_5$ forming and melting and the formation of oxycarbide phase.	[19]
TaC	HIP	Oxyacetylene with 10, 15, 20 mm standoff distance, corresponding to 2300, 2190, and 1990 ºC	S	β-Ta$_2$O$_5$, α-Ta$_2$O$_5$	Delamination Cracks	Delamination caused by the combination of thermal mismatch and gasses escape. Cracks caused by the fixture due to thermal expansion.	[26]
TaC-GNP	SPS	Plasma spray gun, T=2575 ± 55 ºC	S	Ta$_2$O$_5$, TaO$_3$	Surface burst Oxide scale thickness reduced with GNP additions	The surface burst was due to the gaseous product. The addition of GNP can shield oxygen diffusion so increased the oxidation resistance.	[27]

TaC-MoSi$_2$	HIP	Preliminary oxidation at 1600 ºC Combustion flame of oxygen and hydrocarbon gasses	S+L	Ta$_2$O$_5$ SiO$_2$ (L) + Ta$_2$O$_5$ SiO$_2$ (Ta, Si)O Mo$_5$Si$_3$ (S)	Ta$_2$O$_5$ with Glassy Ta-Si-O, and crack Silica phase exposed during severer conditions	Cracks were due to the gaseous products, and thermal mismatch. MoSi$_2$ did not improve oxidation resistance significantly.	[107]
TaC-MoSi$_2$, TaC-SiC	Plasma sprayed	Plasma flame over 2000 ºC for 60s	S	Ta$_2$O$_5$ SiO$_2$	TaC coating was totally oxidized. The tac-mosi$_2$ oxide layer was partially detached. TaC-SiC showed low mass loss	The MoO$_3$ is responsible for the delamination, Ta$_2$O$_5$-SiO$_2$ is a protective layer and prevent further oxidation.	[76]
TaC-SiC-CNT	SPS	Plasma arc-jet under a heat flux 2.5 MW/M^2	S	Ta$_2$O$_5$ SiO$_2$	Multiple chasms, cracks, and deep pits are seen in TaC, but not in TaC-CNT, TaC-CNT-SiC sample.	The addition of CNT improves the thermal conductivity to dissipate heat better. Grain sealing was also overserved by CNT. SiO$_2$ showed protective properties against oxidation.	[20]

40

HfC	HIP	TGA: 1200-1530 ºC Laser heating: 1800-2200 ºC P_{O2}: 0.02 and 1 at	L	HfO_2	Permeated with small pores and cracks	A gasses counter diffusion model was developed. The volume change due to the phase transformation did not cause cracks	[108]
HfC	HfC powder	Isothermal: 478-602 ºC P_{O2}: 4, 8, and 16 kPa	L	HfO_2 Oxycarbide C	Cracks, powder, broke down into small particles	After initial oxidation and formed oxycarbide, 2 steps oxidation: (1) diffusion controlled, (2) Phase boundary controlled at 50 % of oxidation. Residual carbon was found.	[110]
HfC	CVD film	240 s at 1400, 2060 ºC 390 s at 2060 ºC 7 % O_2, 93 % Ar	L	HfO_2 oxycarbide	3 distinct layers formed after oxidation, including porous HfO_2, dense oxycarbide, and inner carbide	A moving-boundary diffusion model developed and suggested that the oxycarbide is a protective layer with low O_2 diffusion rate	[109]

HfC (100) single crystal	Floating zone technique	Isothermal: 600-900 °C Oxygen pressures: 2 to 8 kPa mixed with Ar for 180 h.	L	HfO_2	Two zones were found. A dense inner zone and pores and cracks were found in zone 2	Zone 1 contained a twice amount of carbon than zone 2, and the thickness of zone 1 remained constant. Zone 2 was HfO_2 layer and its thickness increased linearly with time.	[111]
HfC-MoSi$_2$	Pressureless sintering	Arc-jet testing, Lower enthalpy for 100 s, higher enthalpy for 300 s	S	HfO_2, SiO_2	Surface crack. Discontinued SiO_2 was found. Oxide scale showed layered structure.	No continued SiO_2 observed due to the gasses products. The layered scale consisted: 1. Porous outer layer. 2. A dense interlayer and an oxycarbide layer. 3. Innermost layer HfO_xC_y and SiO_xC_y.	[25]

42

HfC-MoSi$_2$ HfC-TaSi$_2$	HIP	1600 ºC in air	L	HfO$_2$ Hf$_6$Ta$_2$O$_{17}$	Cracks, pores. No continuous silica layer	MoSi$_2$ contained samples performed better than TaSi$_2$ based samples. Mixed oxide Hf$_6$Ta$_2$O$_{17}$ was found due to the solid solution formed during the sintering.	[107]
HfC	LPCVD	Oxyacetylene torch at 3000 ºC for 60, 120, 180, 240 s.	S	HfO$_2$	3 distinct regions were found. Micro-cracks found at the hottest zone. Border region was porous.	Promising protection against oxidation. The molten HfO$_2$ and oxycarbide phase were responsible for such behavior.	[118, 119]
HfC-MoSi$_2$	Pressureless sintering	Reactor called REHPTS. In air, at 1800, 2000, and 2200 K for 20 min	L	HfO$_2$ HfSiO$_4$	Porous and cracked surfaces look similar after oxidation at 1800, 2000, and 2200 K.	Oxidation performance was better in higher temperature test due to the formation of glassy phase	[32]

HfC-SiC	2D and 3D CVD coating	in the air with the arc-image furnace. The highest temperature went up to 2000 ºC	L	HfO_2 $HfSiO_4$	Extensive liquid phases formed where HfO_2 island floated.	The liquid phase was responsible for the high oxidation performance. The 3D structure showed better oxidation resistance than 2D structure.	[112]

TaC-HfC

HfC-25 wt% TaC	HIP	TGA: 1200-1530 ºC Laser heating: 1800-2200 ºC P_{O2}: 0.02 and 1 at	L	HfO_2 $Hf_6Ta_2O_{17}$	Oxide scale was porous. Surface was ragged and irregular	Gaseous products evolution caused the cracking and spalling.	[108]
HfC-10, 20, 30 wt %TaC	CVD film	In the air, in a tube furnace at 1000 and 1200 ºC. Oxyacetylene torch for high temperature	L+S	N/A	Oxide scales were well attached to the substrate. Only HfC-20 wt% TaC cracked and flaked away in high temperature tests.	N/A	[114]
HfC-1-22 vol% TaC	CVD+annealing	Oxyacetylene torch at 1750 ºC	S	N/A	Scale spalled	More spalling with increasing TaC content	[115]

3HfC-1TaC	CVD	oxyacetylene torch	S	HfO_2 $Hf_6Ta_2O_{17}$	3 zones were observed	The formation of $Hf_6Ta_2O_{17}$ was responsible for the outstanding oxidation performance.	[116]
$Ta_{0.8}Hf_{0.2}C$-$MoSi_2$	Pressureless sintering	oxyacetylene torch	S	$Ta_2Hf_6O_{17}$ Ta-Hf-Mo oxycarbide	Double layer structure was observed	The outer layer comprised $Ta_2Hf_6O_{17}$, inner layer was Ta-Hf-Mo oxycarbide. Both layers were protective against oxidation.	[10]

Chapter III Materials and Methods

This chapter details the materials used, the characterization techniques and equipment utilized in the present study.

3.1 Materials

In this study, only two ceramics powders were used for synthesizing the TaC-HfC solid solution samples. No sintering or reinforcing additives were added. In the following subsections, the characteristics and properties of these two powders will be described.

3.1.1 Tantalum Carbide Powder

Tantalum carbide powder in this study is a commercial powder obtained from Inframat Advanced Materials LLC, Connecticut, USA. It has dark brown color. The powder has an average particle size of $0.360 \pm 0.016\,\mu m$ measured by imaging processing method. The purity information is provided by the vendor, and the information is as follow: the purity of the powder is 99.7 wt. %, the impurities include: free carbon (<0.15 wt. %), oxygen (0.15-0.30 wt. %), and niobium (< 0.3 wt. %). The Ta to C ratio is approximately 1:1. The Ta to C ratio is also provided but also verified by the XRD analysis on this powder. The lattice parameter of TaC was measured as 4.4483 Å by XRD analysis.
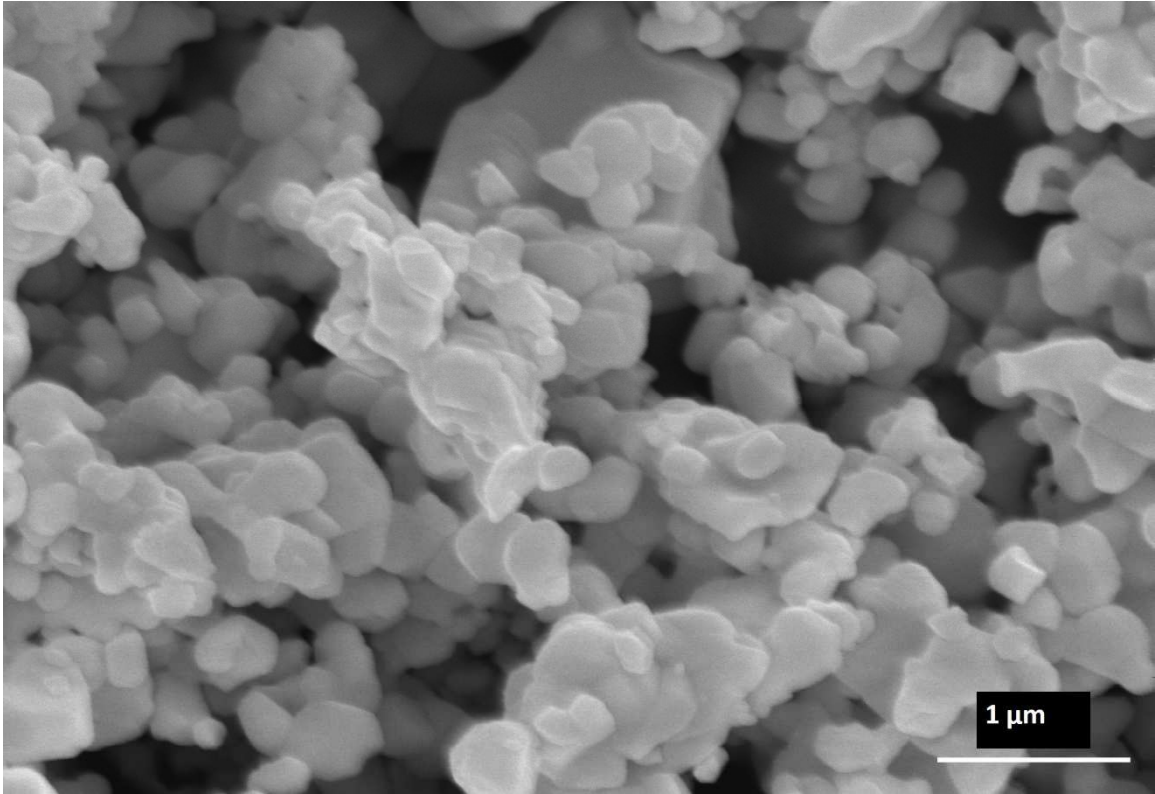
Figure 3.1: SEM image of the as-received TaC powder

3.1.2 Hafnium Carbide Powder

Hafnium carbide powder is a commercial powder obtained from Materion LLC, Cleveland, Ohio, USA. The powder has an average particle size of 0.330 ± 0.075 µm measured by imaging processing method. The purity information is provided by the vendor, and the information is as follow: the purity of the powder is 99.5 wt. %, the impurities include: Cd, Cr, Pb (<0.1 wt. %), Al (0.08 wt. %), and Zr (0.1 wt. %). The Hf to C ratio is approximately 1:1. This is verified by the XRD analysis on this powder. The lattice parameter of HfC was measured as 4.6357 Å by XRD analysis.
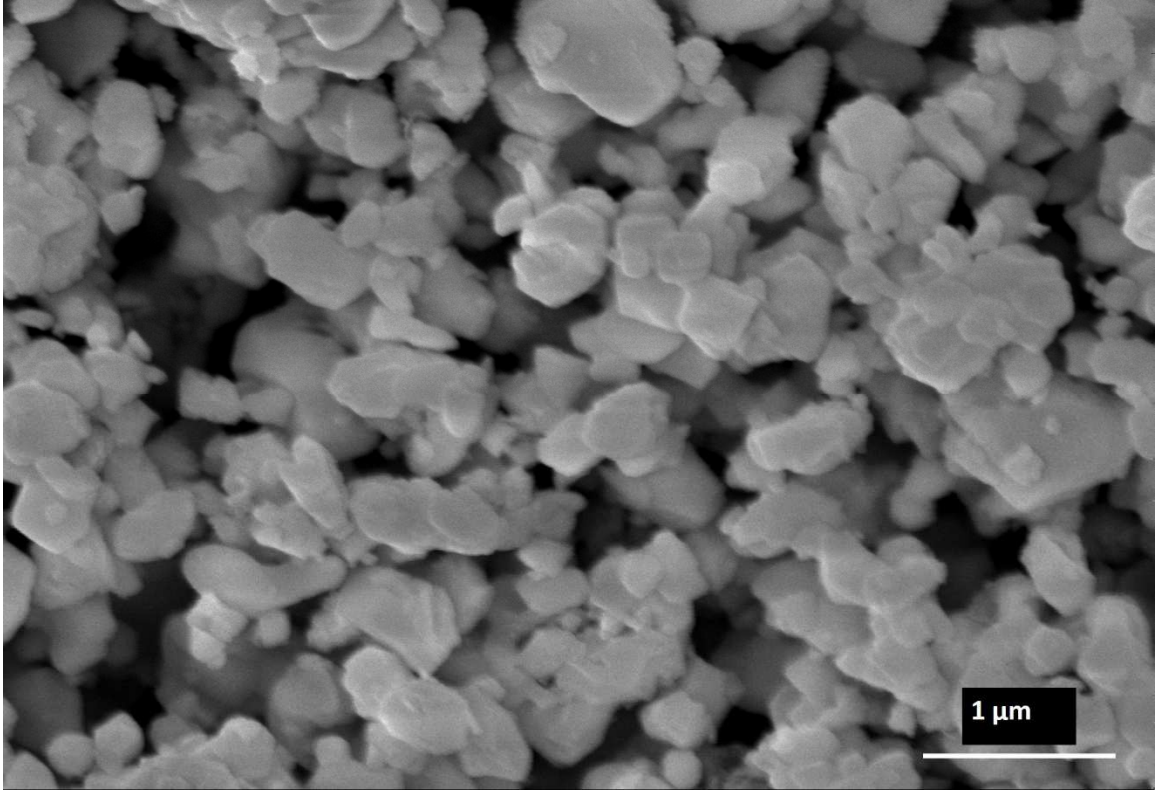
Figure 3.2: SEM image of the as-received HfC powder

3.2 Experimental Procedure

3.2.1 Powder Preparation Methods

Five compositions of TaC-HfC were selected in the present study: pure HfC, 80 vol.% HfC-20 vol.% TaC, 50 vol.% HfC- 50 vol.% TaC, 20 vol.% HfC- 80 vol.% TaC , and pure TaC. Different powder treatment methods have been explored in the present study to (1) achieve uniform particle size in the starting pure TaC and HfC powder, (2) uniformly mix TaC and HfC for the synthesis of TaC-HfC solid solutions. Among different powder treatment methods, tip sonication and ball milling were selected for the present work. Compared to regular bath sonication, tip sonication provides much more intense energy.

TaC and HfC are heavy particles; higher energies are required to achieve the goals in the present study. Similar logic applies to the selection of ball milling technique too; strong mechanical force introduces during the ball milling would be beneficial for breaking down agglomerates and better dispersion. Due to the similar in densities, centrifuge mixing can also be utilized for mixing powders. The detailed description of three techniques will be provided below.

Tip sonication was conducted by a 3/4 ″ high gain probe attached to a Vibra-Cell VCX750 ultrasonic processor (Sonics & Materials, Inc., Newtown, CT). For pure TaC, 15 g of as-received TaC powder was mixed with 400 ml of acetone inside a 500 ml beaker. Acetone was served as mixing media as well as protection against the oxidation and other contamination during the sonication. The beaker was placed into an ice bath to reduce the heat from the sonication process. Each batch of powder mixture was sonication for 45 min at 95% amplitude. Following sonication, the powder mixture was dried inside overnight inside an oven at 80-85 ℃. The mortar and pestle were crushed and further heated for additional 2 hours to ensure fully dried. Previous sintering experience on as-received HfC showed 98% of densification without any powder treatment and sintering additives, so no powder treatment was performed on powder.

Centrifuge mixing was done by a planetary centrifugal mixer (Model: ARM-310, Thinky Mixer, Thinky USA Inc., Laguna Hills, CA. USA) for 30 s with a spinning speed of 2000 rpm. The mixed powders were sent to tip sonication for another 10 min and followed by drying process mentioned above.

Ball milling was utilized in the present study as well. Powders were mixed by a desktop high-energy vibratory ball mill machine (Across International LLC. New Jersey, USA). Pure TaC and HfC initial powders were ball milled for one hour individually, and then the powders mixture was milled for an extra hour. The ball to powder ratio was 3:1, using WC balls 6 mm in diameter. No further powder refinement was intended, which is why the ball to powder ratio was set lower than one would normally do in the ball milling treatment. The mixing results and phase evaluation after ball milling will be discussed in Chapter 4.

3.2.2 Consolidation by Spark Plasma Sintering

Mixed powders were consolidated by spark plasma sintering using a Thermal Technologies model 10-4 spark plasma sintering machine (Thermal Technologies, LLC, Santa Rosa, CA). A 20 mm in diameter graphite die was used due to its high electrical and thermal conductivity. Graphite foils have wrapped the powders between the powders and the inner wall, and the upper and lower punches for easy removal. The temperature was measured by a pyrometer targeting at a pre-drilled hole on the side of the graphite die. Samples were sintered at 1850ºC with a heating rate of 100 ºC/min and a pressure of 60 MPa. The holding time was 10 min and the environment in the vacuum was set at a pressure of 4 Pa. The sintering parameters were decided based on our previous experience on sintering TaC-GNP composites. [18] Near full dense samples was achieve in these studies. The relative ram displacement along with the temperature, pressure, power input, and vacuum was logged during sintering. This information can be used for the calculation of

the instantaneous relative density, which can provide insight information on the densification mechanisms. The instantaneous relative density can be calculated by the following equation:

$$\rho_{inst} = \left(\frac{L_f}{L}\right)\rho_f \qquad \text{Eq. 3.1}$$

In which ρ_{inst} is the instantaneous relative density, L is the specimen thickness at time t throughout the SPS process, which can be calculated by subtracting the ram displacement from the initial compact thickness. L_f and ρ_f are the final specimen thickness and final densification, respectively.

3.3 Microstructural Characterization

The sintered pellets were ground using SiC paper to remove the graphite foil surrounded the pellets surface. The apparent bulk density of the sintered pellets was measured by Archimedes methods. De-ionized water was used as immersion media. Helium gas pycnometer (Accupyc 1340, Micromeretics Instrument Corporation, Norcross, GA) was also employed to measure the densities. Helium pycnometer should give more accurate results, but the results can be affected if the sample contains open pores. The results from both methods were compared to achieve the most accurate data. The relative density was obtained from the ratio between the measured density and theoretical density. Theoretical values were calculated based on the rule of mixing. Phase's information for the each starting powder and the sintered samples were characterized by X-ray diffraction (XRD) (Siemens D-500) using Cu Kα radiation at a scan rate of 2 deg/min. The operating

voltage and current were set at 40 kV and 35 mA, respectively. The sintered pellets were sliced off a 2-3 mm strip by a low-speed diamond saw for fracturing. JEOL 6330F FE-SEM was used to examine the morphology of initial powders, mixed powders and fracture surface of sintered pellets. The fracture surfaces were also used for measuring the grain size by image processing (Image J). At least 30 grains were measured for each sintered samples. A Focused Ion Beam (FIB) (JIB 4500, JEOL USA Inc., Peabody, MA) was used to expose subsurface to investigate the grain sizes and elemental analysis by an integrated X-ray spectroscopy (EDS). TEM was conducted by a Tecnai FEI F30 TEM equipped with field emission gun (FEI). The operating voltage was 300 kV. "Digital Micrograph" software was used for micrograph analysis.

3.4 Mechanical Properties Characterization

Remaining samples were ground using diamond grit paper to the 15 µm level followed by polishing with diamond suspensions to a 1 µm finish. Nanoindentation was carried out by a Hysitron Triboindenter TI-900 to investigate the elastic moduli for each sintered samples. Sixteen indents were performed on each sample at different locations with a constant load of 8000 µN. Vickers hardness was measured by a LECO LM810AT (LECO Corporation, St. Joseph, MI) microindentation hardness tester at a load of 1 kg and a dwell time of 10 s. 7 to 8 indents were performed on each sample, and the average and standard deviations were calculated as well as the crack length was also measured. Indentation toughness was then evaluated by Anstis equation [120].

$$K_{1C} = 0.016 \left(\frac{E}{H} \right)^{\frac{1}{2}} \left(\frac{P}{C^{\frac{3}{2}}} \right)$$
<div align="right">Eq. 3.2</div>

3.5 Oxidation Study

Three 20 mm in diameter pellets of each TaC-HfC solid solutions were prepared by ball milling method and sintered using the same receipt mentioned before. The oxidation tests were conducted by a plasma flow generated from a SG-100 DC plasma gun. The input power was 30 KW and the exposure time was 60s, 180s, and 300s for all the samples. A 75 mm standoff distant was measured from the plasma gun and sample front surface. A significant standoff distance ensured the ample air (oxygen) exposure. Primary argon gas flowed at 56 slpm, and secondary helium gas flowed at 60 slpm. The front side temperature and gas flow velocity were evaluated by an accuraspary in-flight particle diagnostic sensor (Tecnar Automation Ltd., QC, Canada). The sensor head was mounted 75 mm from the plasma gun, and AlO-101 spray dried powder was used as spraying powder for the temperature and velocity measurement. Pellets were placed in front of a steel tube and held by vacuum. A thermocouple was inserted into the steel tube to measure the samples' back side temperature. It was swirled into a coil shape to make sure proper contact during the oxidation tests. A schematic of the oxidation study was displayed in Figure 3.3. Post-oxidation analysis included phase evaluation by XRD, morphology, and elemental analysis by SEM and EDS.
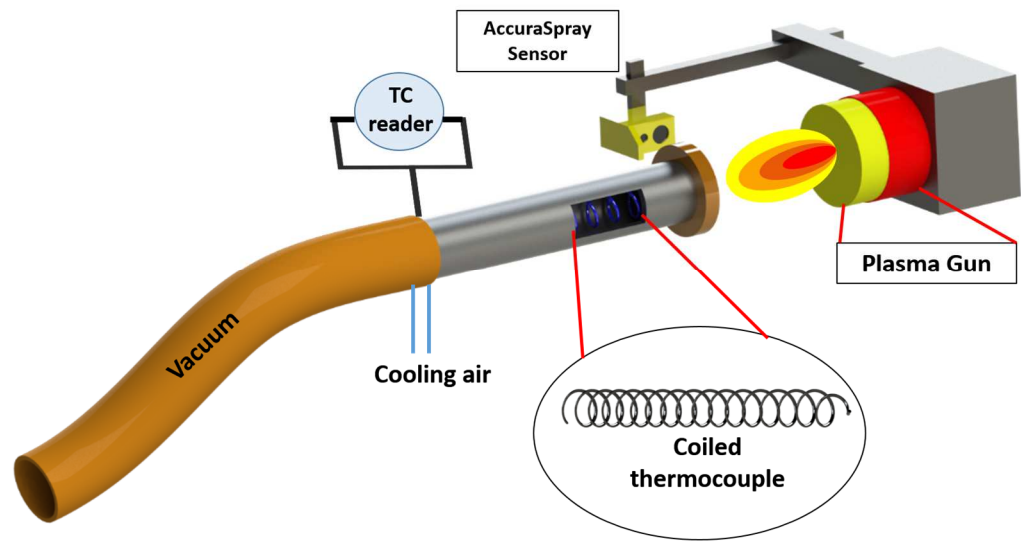
Figure 3.3: Plasma torch oxidation setup

Chapter IV: Results and Discussion

The objectives of the present work are (1) achieving the full dense sintered samples, studying the sintering mechanism of TaC-HfC mixed carbide samples, and investigating the solid solution formation without the help of sintering aids. (2) Evaluation of the oxidation behavior under the simulated environment. In this chapter, detailed discussions on the powder treatment, sintering process, and oxidation behavior will be carried out.

4.1 Powder Treatment

The relationship between the powder treatment and final relative density has been investigated. In both TaC and HfC as-received powders, major agglomerations were found. The size of agglomerates was up to 100 µm. Figure 4.1 shows the lumps in both as-received TaC and HfC powders. The as-received HfC without powder treatment was sintered by SPS using the parameters mentioned in chapter 3; the final densification shows 98%, which was satisfying considered no sintering aids additions and sintered at a relatively low temperature. (The sintering temperature in most of the studies on sintering HfC was exceeded 2000 °C). Previous studies in our group on the sintering of TaC suggested that TaC has really poor sinterability; powder treatment is necessary to achieve highly dense pellet. Tip sonication was applied to as-received TaC powder for 45 min. The treated powder was shown in Figure 4.2. It can be seen that the particles lumps have been broken, but major agglomeration still can be seen. This powder was then sintered by SPS and 85% dense pellet was achieved. Even with 45 min tip sonication, the TaC was still poorly sintered. A close look at the agglomerates in the as-received TaC powder shown in Figure

4.2b. The agglomerates were partially fused already. Ball milling was then applied to the powders for its higher energy during the mixing process. Figure 4.3 shows the as-received TaC and HfC powder after ball milling. Compared to the powder after tip sonication, the particles have been broken down, the size of the powder was uniform. It has been pointed out that small particles with uniform size distribution are a must for achieving high densification in the sintering process. [121] The TaC ball milled powder showed much-improved densification, the final relative density indicated a 97% dense pellet had been made. So the ball milling was used for all the powder treatment in this study.
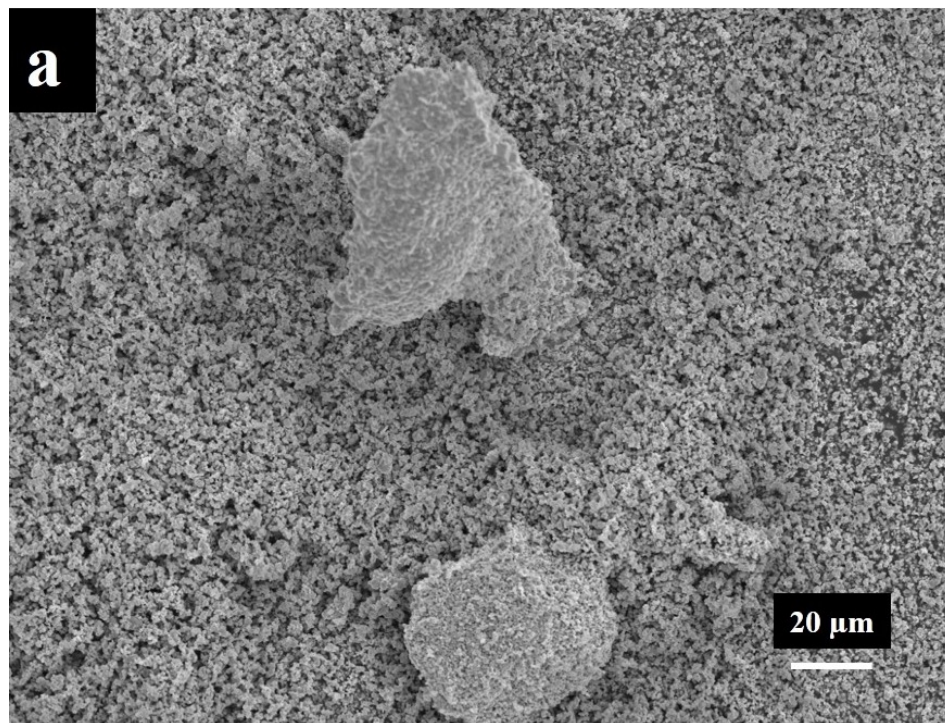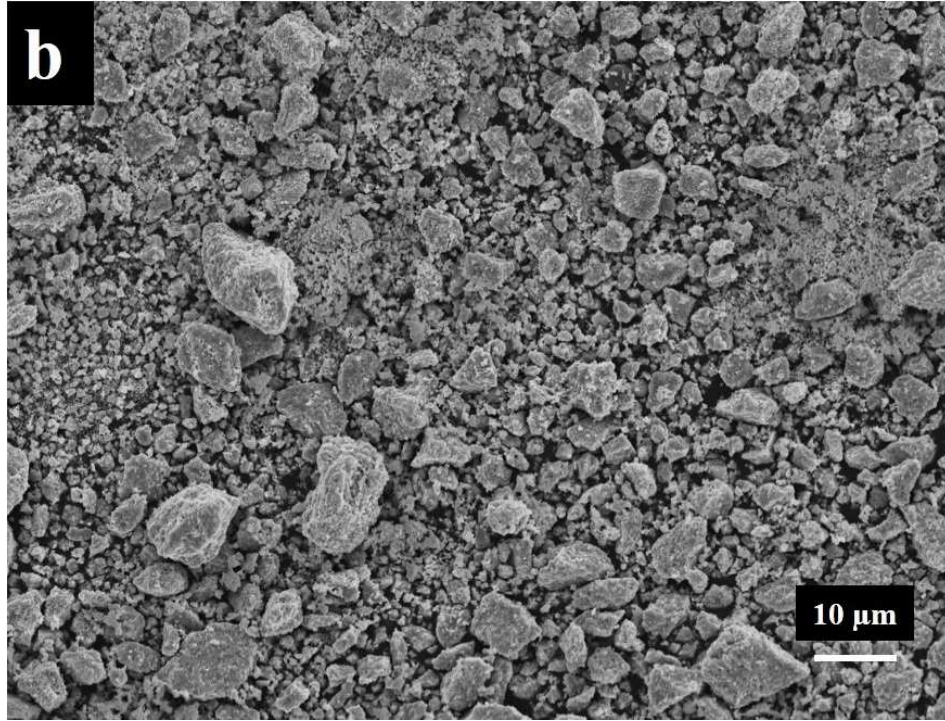
Figure 4.1: Agglomeration in as-received powders: (a) TaC, (b) HfC
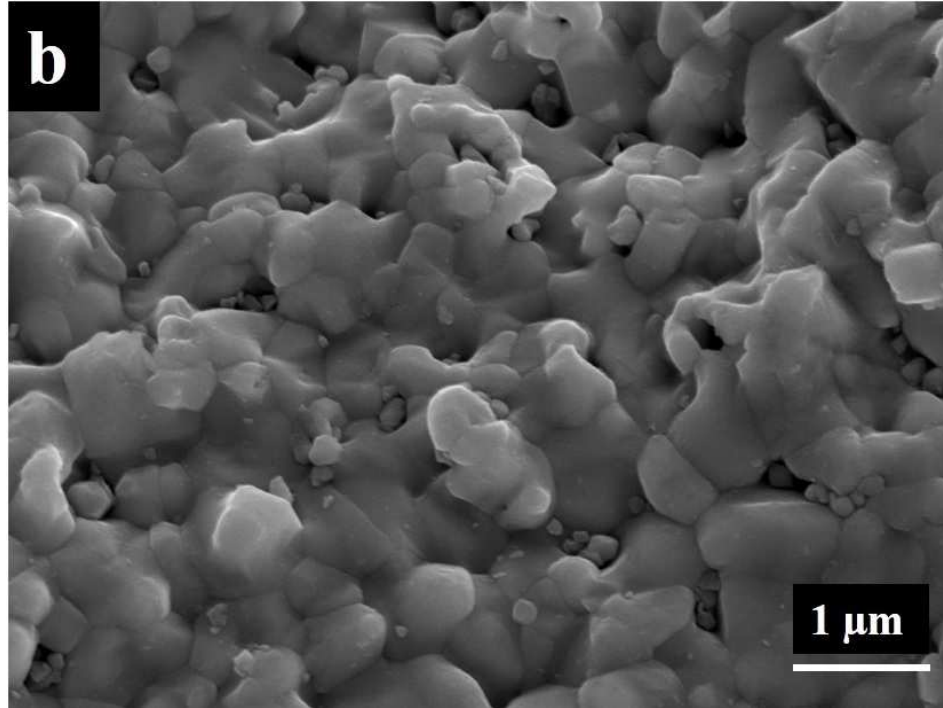
Figure 4.2: TaC powder after tip sonication: (a) Low magnification picture of tip sonicated powder, (b) High magnification picture of partially fused agglomeration
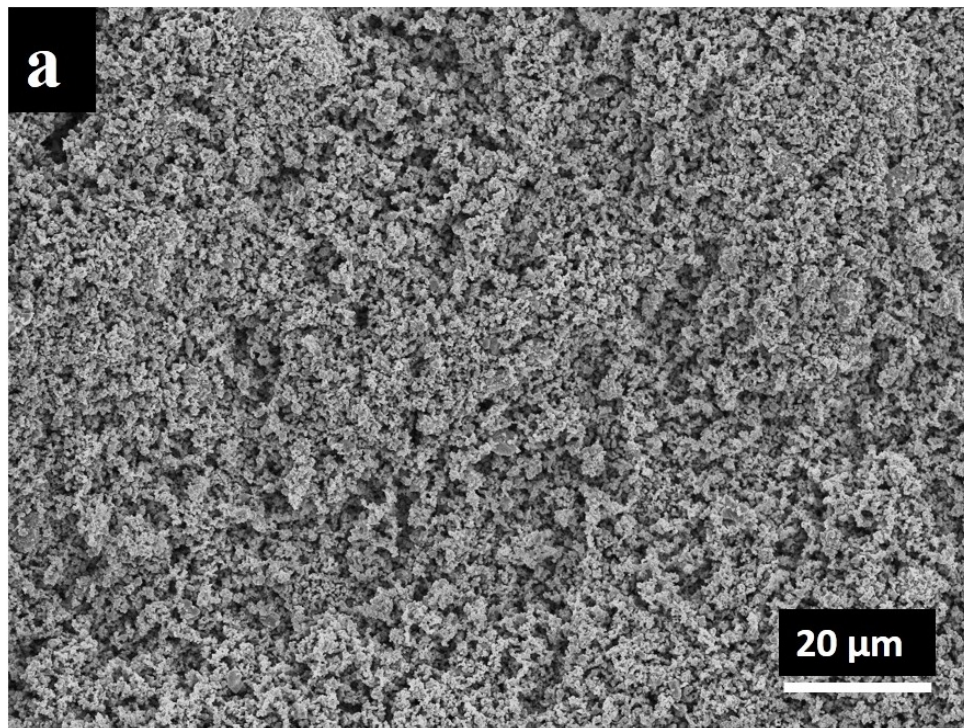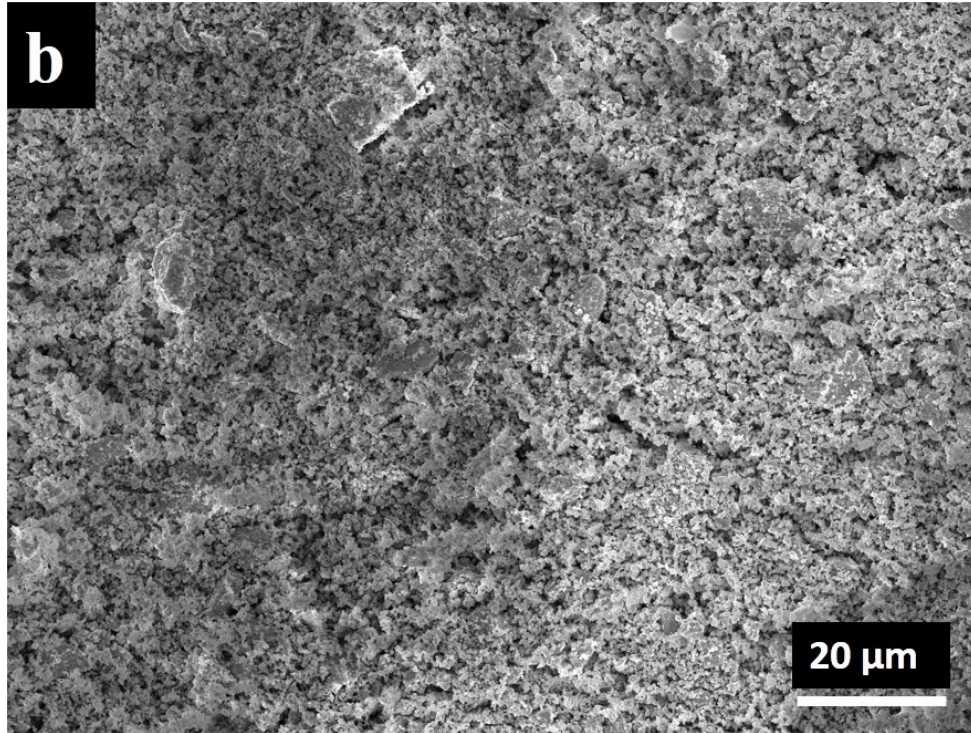
Figure 4.3: Powder morphology after ball milling: (a) TaC, (b) HfC

The ball milling is a high energy mixing processing, and TaC and HfC can form unlimited solid solutions, so XRD analysis has also conducted on the powders before and after ball milling to detect if there was any phase transformation occurred during the ball milling process. The results shown in Figure 4.4. There is no phase transformation has been detected. This result indicated that the ball milling process in this study was solely used to break down the agglomerates, and did not affect the phases of TaC and HfC powders.

Figure 4.4: Powder XRD patterns of five powders after ball milling treatment

4.2 Spark Plasma Sintering of TaC-HfC Solid Solution

4.2.1 Sintering Mechanism

Results of characterization of the density and mechanical properties of sintered samples are tabulated in Table 4.1. For all five compositions of more than 96% densification was achieved. The addition of HfC, including pure HfC itself presented over 98% densification. This indicates that at the present conditions HfC had superior sinterability than that of TaC. Fracture surfaces of sintered composites were examined by SEM and shown in Figure 4.5 and 4.6. All five samples show near fully dense fracture

microstructure, but micropores were also observed in some of the cases, especially in pure TaC. The relative density of pure TaC was measured at 96.7%. There were signs of liquid phase formation during SPS, which were mostly found at the grain boundaries, and on the surfaces of the pores on TaC's exposed grains, as the arrows point out in Figure 4.5b. The phenomenon coincided with Kelly and Graeve's work on pore formation mechanisms for sintering TaC. The liquid phase was identified as melted Ta_2O_5. The Ta_2O_5 comes from the oxygen contamination in the initial TaC powder. [122]

Table 4.1: Density, grain size and mechanical properties of sintered TaC-HfC

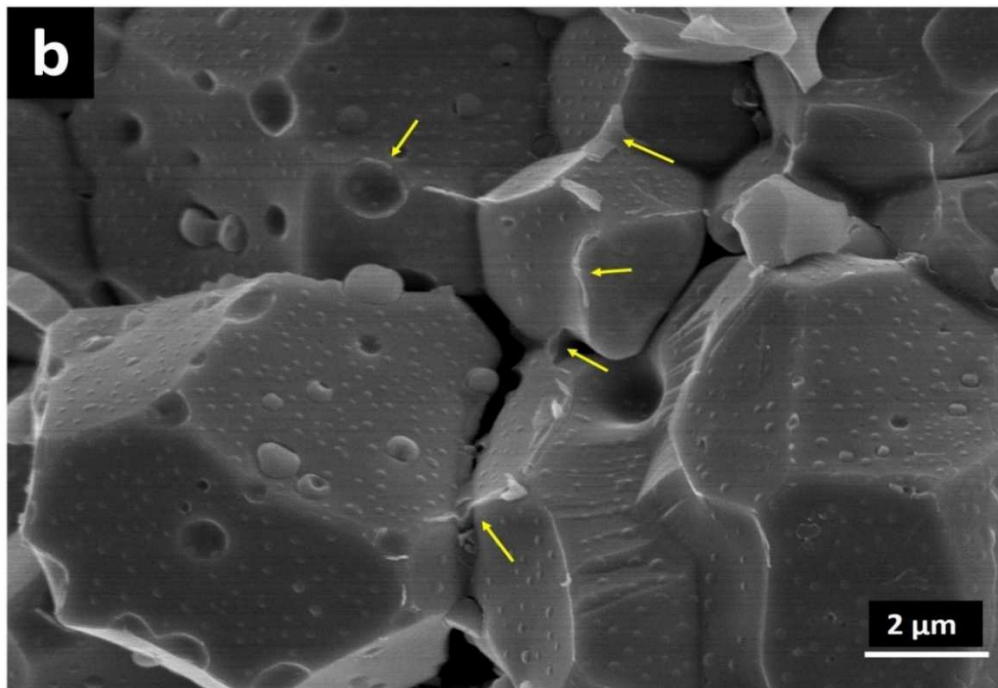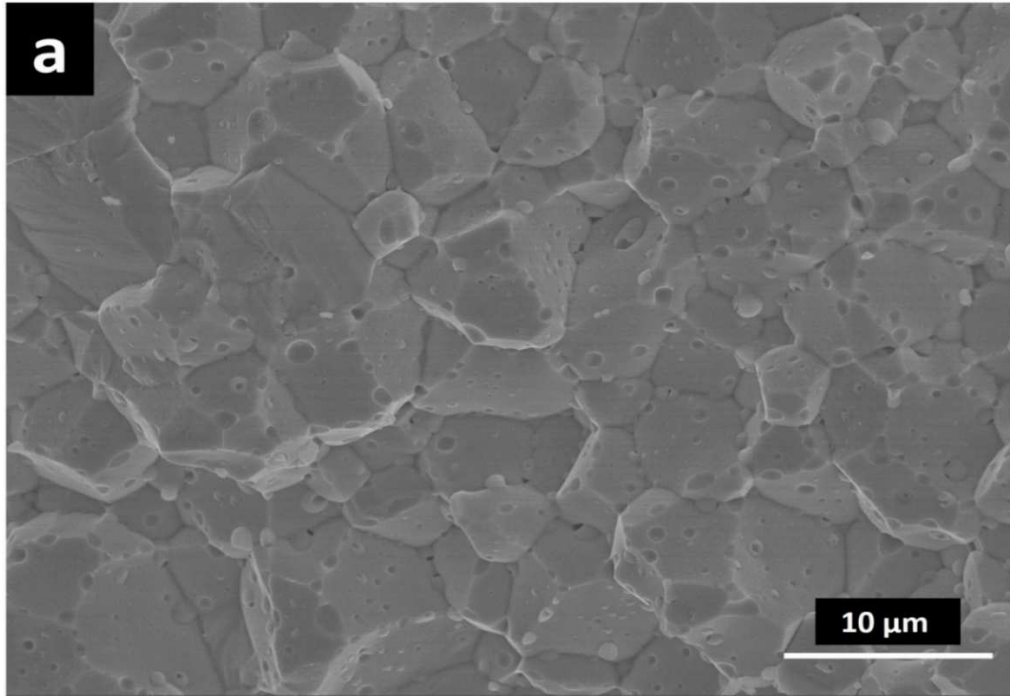| Name	Densification (%)	Avg. Grain Size (μm)	Microhardness (GPa)	Elastic Modulus (GPa)	Indentation toughness (MPa·m$^{1/2}$)
Pure TaC	96.7	6.8±1.4	12.27±0.87	331.67±4.23	4.56±0.52
T80H20	97.8	6.2±2.1	16.39±0.86	443.24±23.65	4.58±1.06
T50H50	98.2	3.8±1.2	17.15±1.1	523.82±7.03	6.03±0.70
T20H80	98.8	3.1±1.1	19.06±0.27	577.30±6.04	5.51±0.56
Pure HfC	98.5	2.3±0.7	18.46±0.22	360.86±29.53	3.39±0.97

Figure 4.5: Fracture surface of Pure TaC. (a): low magnification, (b): High magnification, arrows pointed at liquid phase. (Tiny lumps on TaC grain were over-coated gold)

The average grain size increased from 0.36 µm, which is the initial particles size,

to 6.8 µm. Some significant gaps were noticed in pure TaC samples, which is due to the

fast grain coarsening without proper densification. In fact, numerous small particles were found sitting on larger grains as shown in Figure 4.5b. The average size of these little particles was close to the initial particle size, and it appears as if they were being absorbed by the larger grains. This behavior can be explained by Ostwald Ripening mechanism. This also suggested that some of the pores of TaC's exposed grain surfaces could be the residual dents left by the small particles when the sample was fractured.

With the addition of HfC, the morphology of the fracture surfaces changed dramatically. Figure 4.6 a, b, c are the fracture surfaces of T80H20, T50H50, and T20H80 respectively. At first glance, the overall densification has been improved. The exposed grain surfaces were clean and free from pores as those in the exposed TaC grains. Fracture behavior also shifted from intergranular to transgranular which implied stronger grain bonding as a result of better densification. Overall densification for these three samples was 97.8%, 98.2%, and 98.8% respectively, with some marginal improvement when HfC content is increased. However, the average grain sizes of these samples dropped significantly: 6.2 µm for T80H20, 3.8 µm for T50H50 and 3.1 µm for T20H80. It was evident that the addition of HfC suppresses grain growth during SPS. What was also of interest is that the pores seen in the pure TaC sample, which was caused by oxygen contamination, have almost disappeared. This occurred in the T80H20 sample where only 20% of HfC was added. This implicated that the oxygen contamination was transferred. There was a new feature in fracture surfaces of samples that contain HfC, which was highlighted in the circled area of Figure 4.6a.
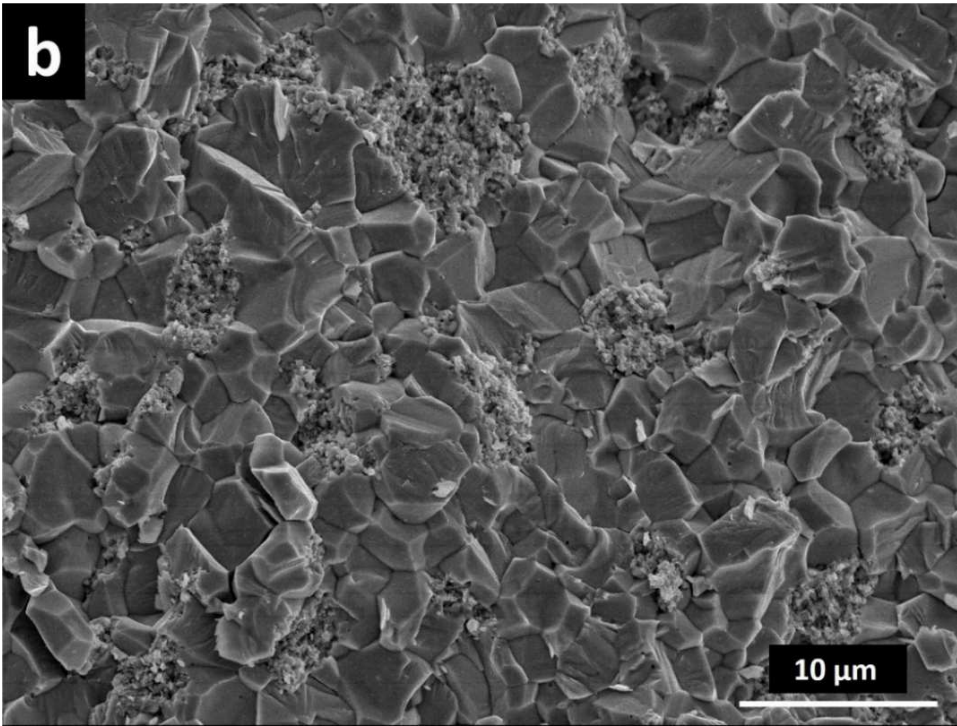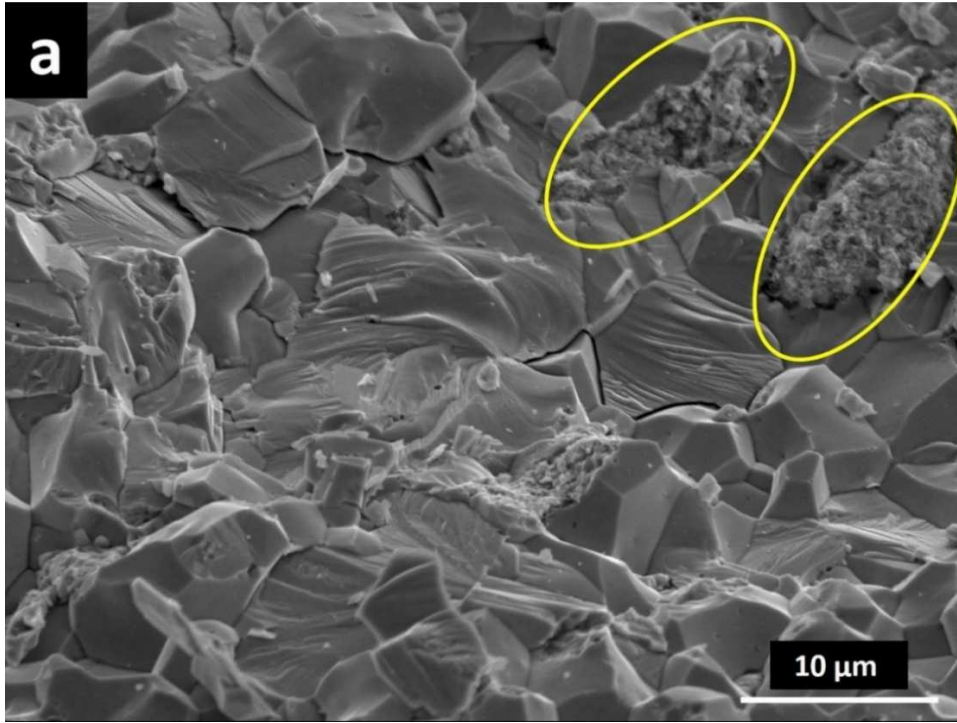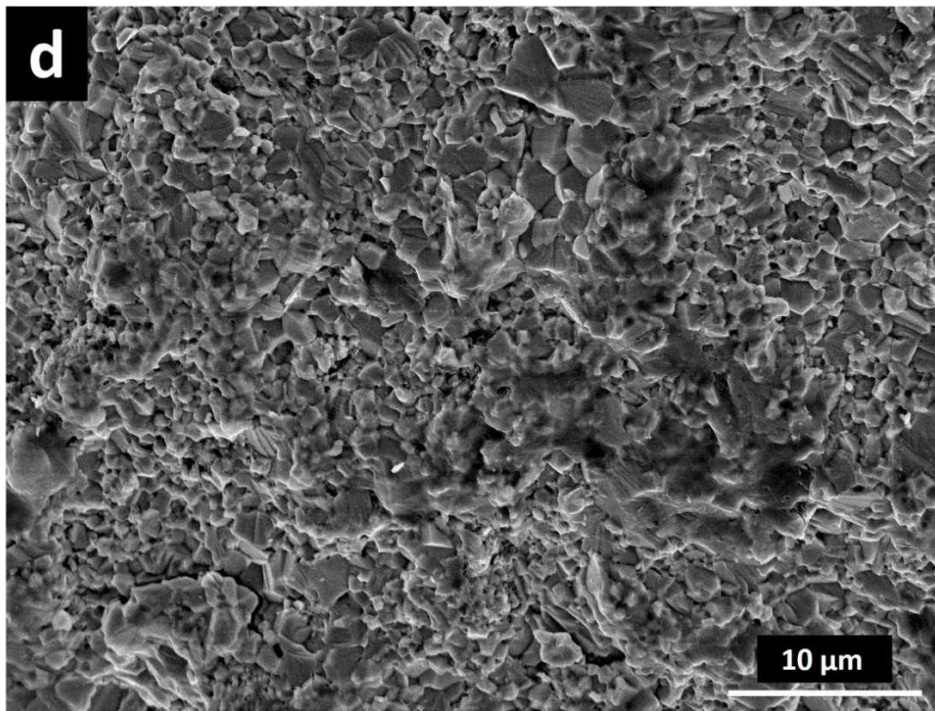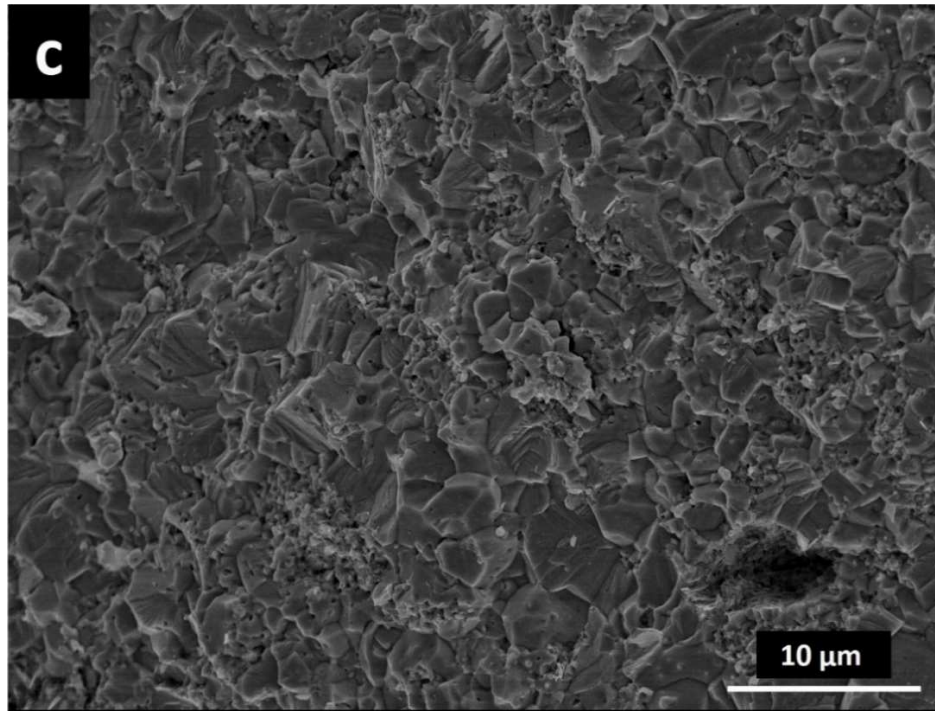
Figure 4.6: Fracture surfaces of HfC contained samples. (a): T80H20, circled areas were amorphous due to oxygen contamination, (b): T50H50, (c): T20H80, (d): pure HfC

This has not been observed in pure TaC. The circled area in Figure 4.6 a showed smeared, ultrafine grains that were noticeably smaller than the average initial particle size of HfC or TaC. EDS on the FIB milled section identified oxygen, carbon, and hafnium as the main elements in the ultrafine region (*The EDS mapping and point analysis were shown in the Appendices, section 1*). Oxygen was not detected in the rest of milled surface. The oxygen content in these areas was around 16 at.%, significantly richer than the one in initial HfC particles (<2 at.%), suggesting the oxygen was transported from elsewhere. Based on thermodynamics calculation completed using FACTSAGE software (*results shown in the Appendices, section 2*), HfC can react with Ta_2O_5 and form TaC, HfO_2, and CO in the temperature range (1850 ^oC) of this study. The fine grained region in HfC-contained samples can be recognized as a mixture of HfC, HfO_2, and Hafnium oxycarbide phase. Pure HfC sample in Figure 4.6d shows high densification with the mildest grain growth. Since the activation energy needed for diffusion to occur in HfC was much greater than that of TaC [28], very limited grain growth took place in pure HfC sample. The amorphous particles can still be found in pure HfC sample but at many small concentrations than in the 3 TaC-contained samples. One possible reason is the lower oxygen contamination in pure HfC sample, up to 0.3 % was reported for the TaC powder from the manufacturer vs. trace amounts in the HfC sample. It was evident that the porosity in TaC-HfC samples was mainly due to the oxygen contamination, and it affected TaC and HfC in different ways. The pore formation in TaC was caused by liquefied Ta_2O_5 (melting point of Ta_2O_5 is1850 ^oC). HfO_2 would not melt since it has a much higher melting point i.e. 2800 ^oC. The trace amount of oxygen contamination on HfC powder surface retarded the diffusion between HfC, hence, resulted in minor porosity in the final HfC-contained pellets.

To better understand the sintering behaviors of these five samples, overall densification versus heating period time curves are plotted and displayed in Figure 4.7. Full densification was reached prior to the end of the holding time for all samples. So, the holding time can be reduced in the future work to restrain the grain growth during the holding. Each sample presents three distinct stages based on this plot, the starting and end time for each stage has been summarized in Table 4.2. The 0 s was defined when the temperature reached to 600 °C due to the sensitivity of the pyrometer. In the first stage, the maximum pressure was achieved around 100 s. External loads were responsible for the initial densification through rearrangement and compaction of the initial powders. Furthermore, a minor degree of diffusion started. The second stage started from 400 s to the time the samples reached full densification. In this second stage, the slopes of each curve reflect the densification rate. The densification rates for five samples was calculated, and results were tabulated in Table 4.2. It was apparent that the pure TaC had the quickest diffusion rate, and the rest of the samples had similar densification rates. The onset densification time increased with the increase of the HfC addition. The delay in densification for HfC contained samples can be explained from the energy point of view. During the SPS the densification process, though with the different driving forces, is mainly a diffusion process. The energy provided by SPS is responsible for heating the samples and accommodating the diffusion. The activation energies of diffusion for pure TaC and HfC are 39.49 kJ and 60.42 kJ respectively [28]. A 21 kJ energy difference between the pure TaC and pure HfC resulted in a 2 min early densification as shown in Table 4.2. For the three solid solution samples, the formation of the solid solution has been observed in the present study (Detailed analysis shown in the next section) and also has

67

been confirmed by other researchers [7-11]. The enthalpy of mixing for three solid solution samples have been calculated *(the procedure shown in the Appendices, section 3)* and can be found in Table 4.2. Since the enthalpy of mixing is greater than zero for all three solid solution samples, extra energies are needed in order to form a solid solution. Additionally, due to the higher activation energy for diffusion of HfC, the onset densification time gradually increased from T80H20 to T20H80 samples. The total time needed to reach the highest densification (stage 2) for three solid solution samples and pure HfC sample were comparable, and the slope of stage 2 were the same. However, the pure TaC sample showed extreme high densification rate compared to the rest 4 samples. This advocated the existence of a faster densification mechanism beside diffusion and well collaborated with aforementioned liquid phase formation in TaC sample due to the melt of Ta_2O_5 during SPS. No liquid phase formation was observed in the rest 4 samples; the dominated densification mechanism was the only diffusion in the HfC contained samples. The addition of HfC also introduced the lattice mismatch, so the diffusions in HfC contained samples were slower.

Table 4.2: Densification stages and enthalpy of mixing of TaC-HfC samples of five compositions

	1st stage	2nd stage	3rd stage	Densification rate (%/min)	ΔH_{mix} (kJ)
Pure TaC	0s ~ 304s	304s ~ 479s	479s ~ 750s	16.2	N.A.
T80H20	0s ~ 358s	358s ~ 685s	685s ~ 750s	7.8	139.01
T50H50	0s ~ 413s	413s ~ 722s	722s ~ 750s	7.8	139.05
T20H80	0s ~ 420s	420s ~ 758s	758s ~ 750s	7.2	139.10

Pure HfC	0s ~ 460s	460s ~ 753s	753s ~ 750s	7.8	N.A.
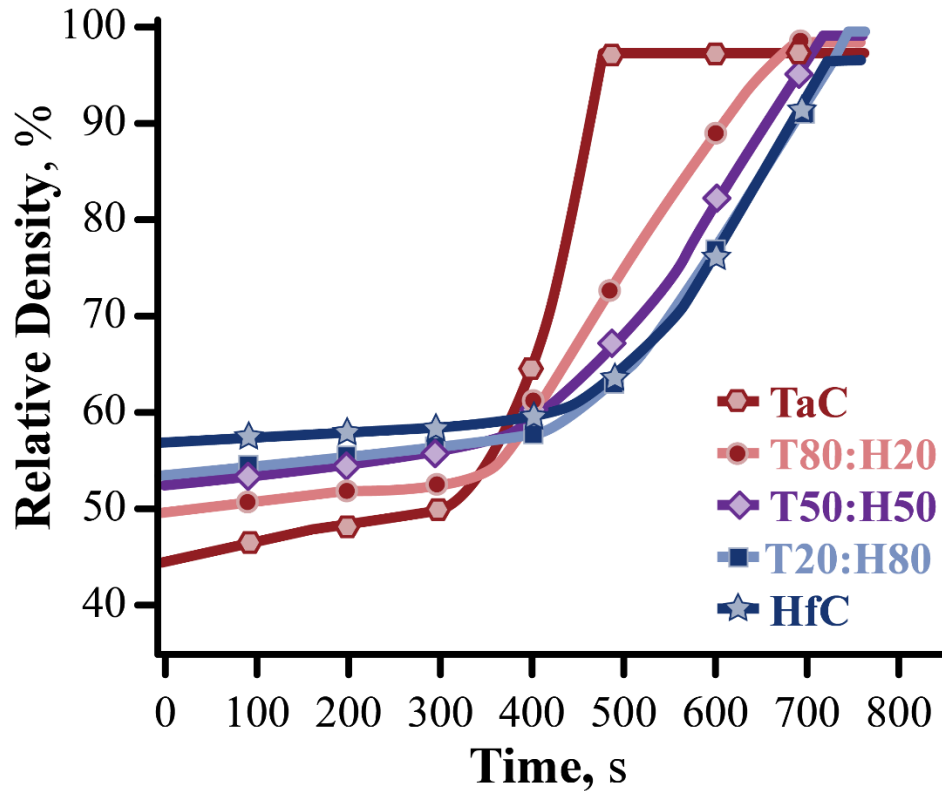
Figure 4.7: Relative densities verse time plot during spark plasma sintering

4. 2. 2 Phase Evaluation of Sintered Pellets

Figure 4.8 shows the XRD patterns of five sintered samples. Figure 4.8a shows the XRD patterns of starting powders and sintered pellets. For the pure HfC and TaC, peak location, width and relative intensity remain consistent, as expected. In the mixed carbide samples, displays in Figure 4.8b, the peaks of each composition shifted between the pure TaC and HfC peaks. These results strongly demonstrate the formation of solid solutions. These results contrast the findings of Ghaffari et al. in which $TaC_{0.8}HfC_{0.2}$ was consolidated

with SPS and disilicide sintering aids [10], in that study, two individual peaks form with the HfC remaining. This may be a result of the processing parameters (1650 ºC, 30 MPa pressure, and a holding time of 5 min) as it can be concluded that higher temperature, pressure, and longer holding time were needed to have thorough solid solution formation. In addition, the use of sintering aids could also have been responsible for the two individual phases remaining, as they may induce additional diffusion paths.
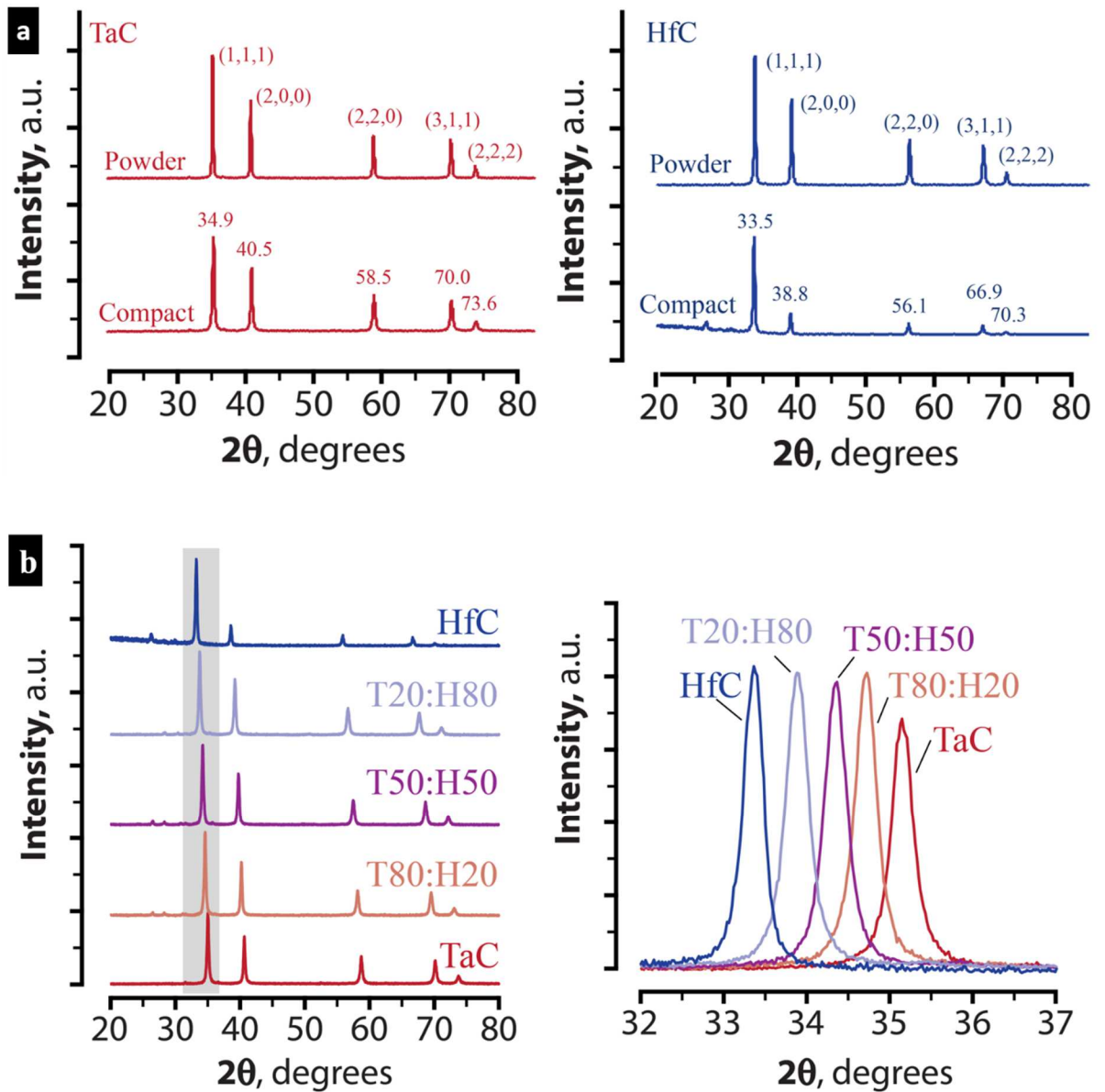
Figure 4.8: XRD results of sintered TaC-HfC composites. (a): pure TaC powder vs. pellet and pure HfC powder vs. pellet, (b) XRD of 5 sintered pellets, caption showed peaks from 33° to 37°

The lattice parameters of TaC-HfC solid solution obeyed Vegard's law. The TaC and HfC values were taken as 4.441 Å and 4.645 Å respectively. [5] The theoretical values of $Ta_{0.8}Hf_{0.2}C$, $Ta_{0.5}Hf_{0.5}C$ and $Ta_{0.2}Hf_{0.8}C$ were calculated. The calculated lattice parameters from XRD patterns of three solid solution samples were summarized in Figure 4.9. The calculated lattice parameters from XRD matched the theoretical values. For additional confirmation, HR-TEM was also employed to measure the lattice constants of three solid solution samples to confirm solid solution formation further. In the Figure 4.10, three areas with three different lattice parameters were identified and labeled as "a," "b", and "c" respectively. The lattice parameters were measured as 4.572 Å, 4.467 Å and 4.486 Å for the area "a", "b", and "c". The values deviated from the original lattice parameters of TaC and HfC suggesting the formation of solid solutions. However, compared to the theoretical value calculated from Vegard's Law, only the area "c" can be considered as T80H20 solid solution. TaC and HfC can form a solid solution at any compositions, and the formation of solid solution is a diffusion process. Even there was only one single phase shown in the XRD pattern; the samples should be considered as mixtures of TaC-HfC solid solution with different compositions.
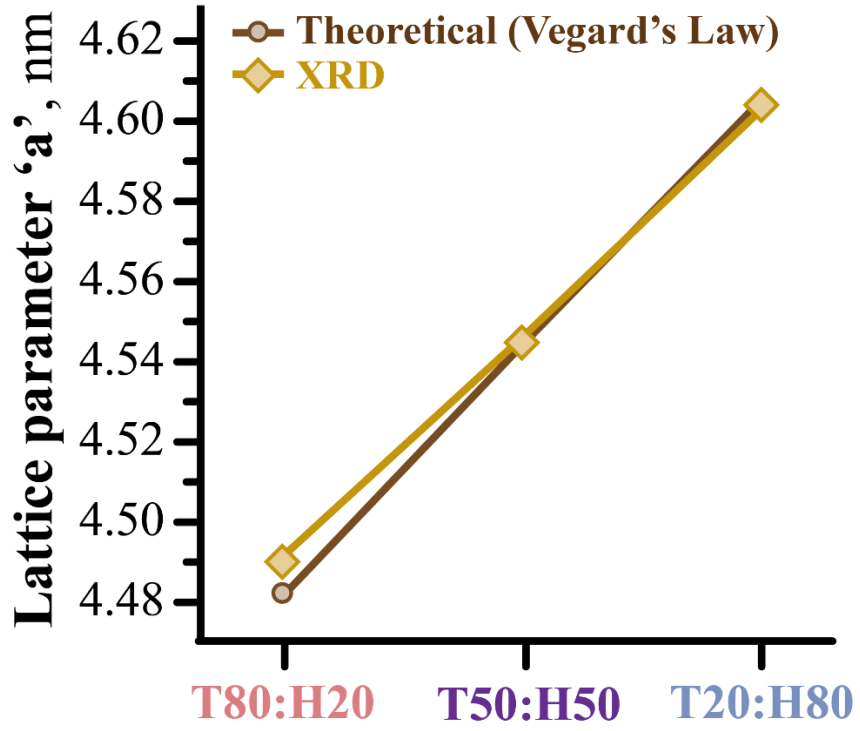
Figure 4.9: Lattice parameter comparison between theoretical value and calculated values from XRD
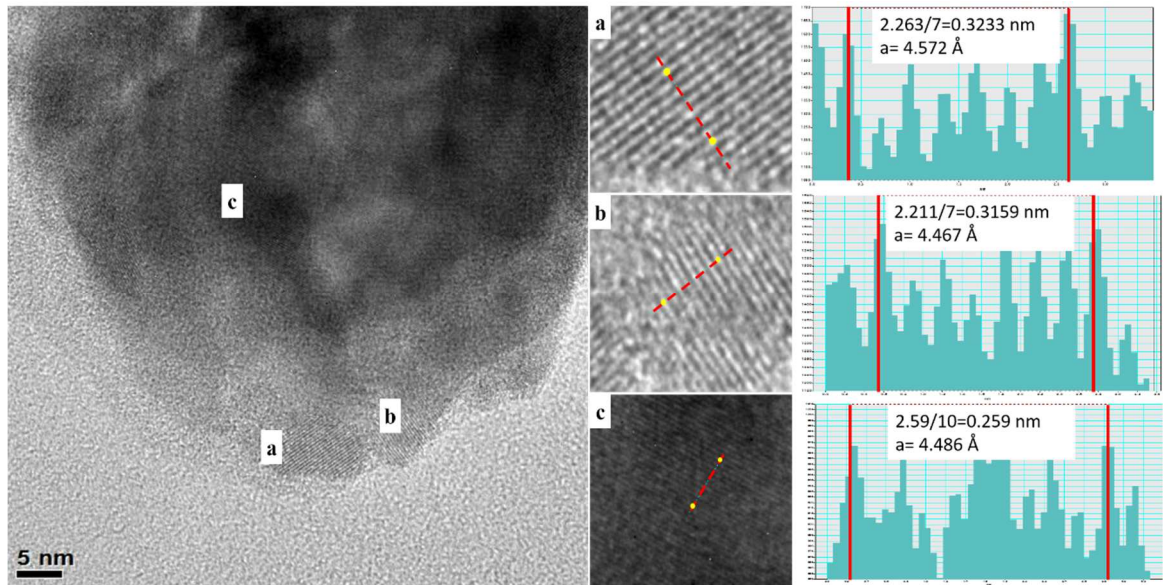
Figure 4.10: HR-TEM image of T80H20. The "a" area had the lattice parameter close to the one of the HfC, the one in the "b" area closed to the one of the TaC, and "c" area was completed "T80H20."

4.2.3 Mechanical Properties of Sintered Pellets

The micro-hardness, elastic moduli, and indentation toughness values for all five samples are summarized in Table 4.1. The pure TaC sample shows the lowest values in both hardness and elastic modulus. The relatively high porosity and large grain size were responsible for these relatively low values. In addition, the pure HfC sample had higher densification and much smaller grain size; it displayed higher values of hardness and elastic modulus than those for the pure TaC sample. The solid solution formation between TaC and HfC is a substitutional reaction. The Ta/Hf atoms are replaced by Hf/Ta atoms in the lattices. As a result, some degree of lattice distortions is introduced into the lattices. Analogous to solid solution strengthening mechanism in metal alloys, these distortions create a local stress field which results in increased hardness. Figure 4.9 shows position

deviation in the lattice parameter of T80H20 sample and negative deviation in T20H80 sample which could be due to incomplete solid solution formation. Since Hf is a larger atom than Ta; the deviation could also be the results of lattice distortion created by the introduction of larger/smaller atoms inside the lattices. This phenomenon explained the increased hardness values in solid solution samples. Similar strengthening mechanisms can be found in CrO_2 strengthening Al_2O_3, Y_2O_3 stabilize ZrO_2.[123, 124] In addition, the overall densification for solid solution samples increased with the increased HfC content, while the grain size decreased. So the increase in hardness values in solid solution samples was anticipated and it was in full accordance with the classic relationship between hardness and grain sizes. Elastic moduli (E), followed the same trend as hardness in all samples. Higher E values were observed for solid solution samples than in monolithic carbides. E value increased with an increasing HfC content for solid solution samples. Although elastic modulus is a material's intrinsic property, the explanation in hardness values can also be applied in elastic moduli data since the evaluation of elastic modulus involved indentation method.

The indention toughness followed the same trend as the hardness and elastic moduli data as well. Despite the toughness value for T50H50 was higher than the one for T20H80, the difference was not statistically significant. The increase in overall densification also strengthened the bonding between the grains. This was concluded from the change in fracture mode shifted from inter-granular (pure TaC) to trans-granular (three solid solutions). Moreover, the solid solution samples had unique ultrafine grain regions that was not found in the pure carbides samples, the ultrafine grain can serve as energy-

dissipation zone resulting in higher indentation toughness in solid solution samples than in pure carbides samples.

4.3 Evaluation of Oxidation Performance

4.3.1 Determination of Oxidation Conditions

The high-temperature simulated oxidation tests have been performed on each sintered samples for 1, 3, and 5 min. The SG-100 plasma gun was utilized in this study since it is originally used for plasma spray, the temperature and velocity generated in the present tests were determined by in-flight particle diagnosis. An accuraspray sensor head was utilized, and ALO-101 spray dried powder was used for analyzing. The sensor was targeted at a distance of 75 mm from the spray gun to measure the temperature of the samples surface. Figure 4.11 shows the results from the accuraspray sensor. The temperature at the surface was measured above 2700 ^{0}C with a velocity of 330 m/s. With these simulated testing conditions, samples would experience both oxidation and ablation similar to the ones that space vehicles would face upon reentry.

Figure 4.11: Accuraspray screenshot the temperature measurement

4.3.2 Morphologies of Post-Oxidation Samples

The morphologies of the post-oxidation samples were studied by SEM and the images for each sample are shown in Figure 4.13-22. Most of the samples remained intact, and did not show any spallation or delamination except for pure TaC samples. The oxide layers of TaC post-oxidation samples were very fragile, and spallation was observed during the tests. So both oxide layer thickness measurement and weight changes data might not be accurate. The data displayed in the Table 4.3 is just for comparison, not for any quantitative analysis.

Table 4.3: Oxide layer thickness

Unit: μm	PT	T8H2	T5H5	T2H8	PH
1 min	35.99±2.33	19.74±1.00	9.00±0.44	20.30±2.29	57.28±3.44
3 min	73.36±6.64	29.18±1.43	15.73±1.09	50.54±3.43	151.05±2.86
5 min	305.20±11.47	39.64±1.91	28.46±1.41	101.04±2.36	189.78±2.72

For the sake of better visualization, the oxide layer thickness data was also plotted in bar chart shown in Figure 4. 12.
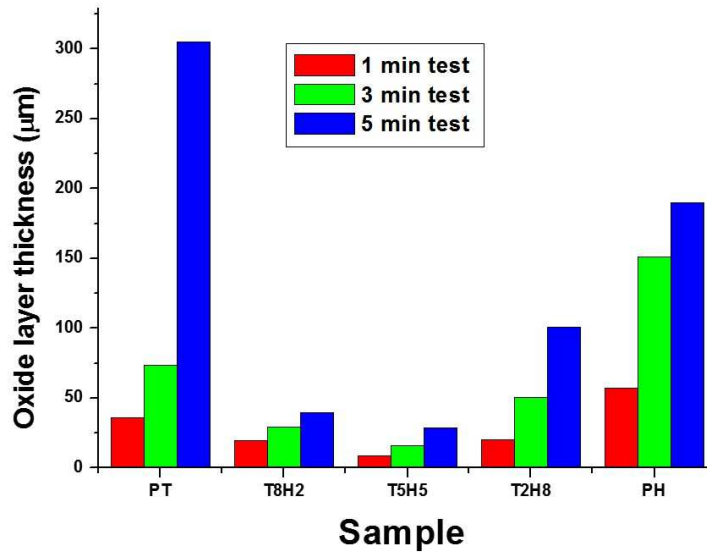

Figure 4.12: Oxide layer thickness bar chart plot

From Figure 4.12, it can be concluded that solid solution samples display better oxidation resistance compared to both monolithic carbides. Among the three solid solution

samples, T50H50 had the thinnest oxide layers for all the three time durations. SEM examination on the top surfaces and cross-sections of each samples are discussed below.

4.3.2.1 The Morphologies of Pure HfC Top Surface and Cross-Section.

For pure HfC, there was no significant difference between the samples for different time duration oxidation tests. In the low magnification pictures, there is no significant difference between 1 min test and 3 min test, and the top surfaces for both the time duration are dense with scattered cracks. The top surface for 5 min is less dense, and beside the cracks that be seen in the 1 min and 3 min tests, spallation could also be observed. The underneath materials were fully exposed to the high-temperature plasma flame and oxidized. The high magnification pictures for each test time duration are also shown. All three tests showed the sign of melting and the degree of melting increased with the grown in testing time. In the 1 min test, grains can still be observed, and the size of grains was still comparable to the initial HfC grains. However, in the 3 min and 5 min tests, the grains disappeared. The high magnification pictures suggest that the grains have melted and fused together. The melting point of HfO_2 is around 2800 ^{o}C, the sign of melting could also verify our temperature measurement for the present study.

The cross-section of HfC oxidized samples were porous, and only a single layer oxide was observed. Samples from different time duration did not show obvious difference except for the thickness. The thickness of the oxide layers for the three samples were uniform. Most outer layers exhibited the sign of melting, in accordance with the observation from the top surface. Oxidized grains could be clearly seen in the cross-section,

78

suggesting that the oxidation initiated at the grain boundaries. The cracks were inter-connected, which provided a pathway for the gaseous products without disrupting the oxide layers. One of the important reasons for HfC has superior oxidation resistance is the formation of a dense, crack-free oxycarbide layer, which is considered as a protective layer. However, in the present study, such oxycarbide layer is barely visible; only few micron thick dense layer can be seen, as shown in Figure 4.14b.HfC can dissolve oxygen without turning into HfO_2, so the oxidation process of HfC always begins with the adsorption and diffusion of oxygen into the lattice. However, in the present study, high temperature and high velocity accelerate the diffusion process. Hence, the oxycarbide phase became unstable and transformed into HfO_2.
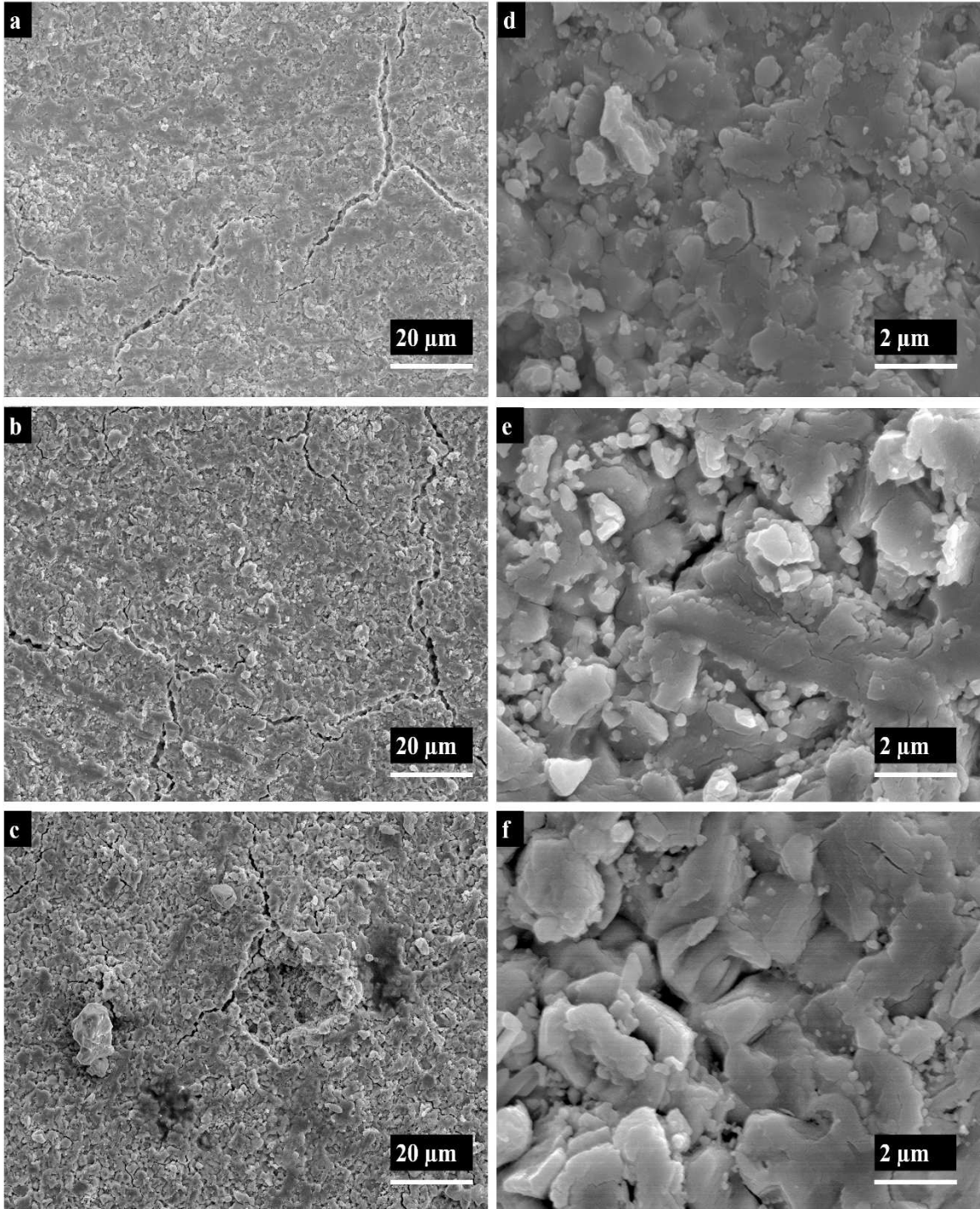
Figure 4.13: Top surface of the pure HfC after oxidation tests. Low magnification (a) 1 min, (b) 3 min, and (c) 5 min. High magnification (d) 1 min, (e) 3 min, and (f) 5 min
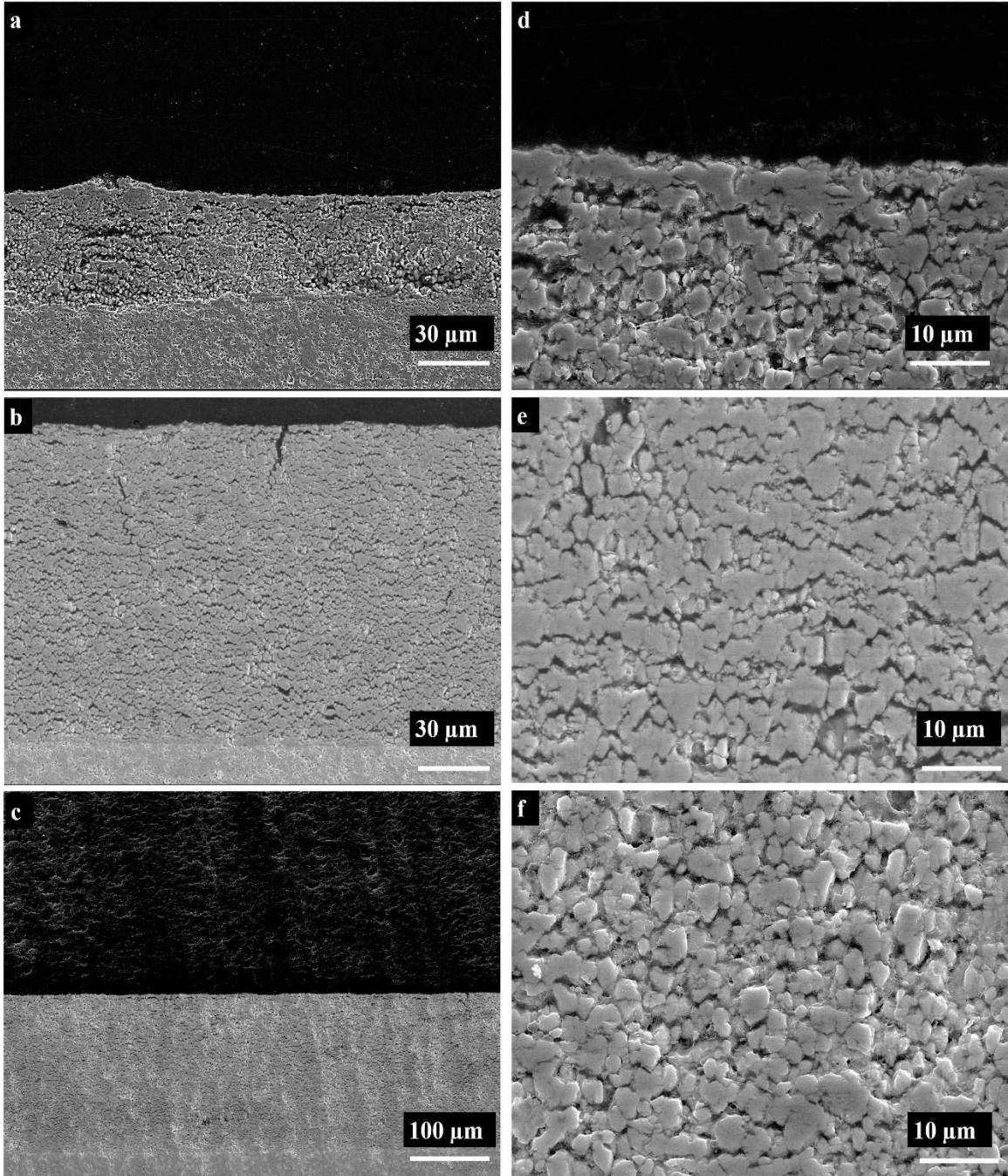
Figure 4.14: Cross-section of the pure HfC after oxidation tests. Low magnification (a) 1 min, (b) 3 min, and (c) 5 min. High magnification (d) 1 min, (e) 3 min, and (f) 5 min

81

4.3.2.2 The Morphologies of T20H80 Top Surface and Cross-Section

The top surfaces of T20H80 samples were dense but covered with much more cracks compared to pure HfC samples. The crack density increased with increased oxidation time duration. The high magnification pictures also showed the signs of melting. This is expected since the melting point of Ta_2O_5 from the TaC addition is only around 1800 ^{o}C, way below our testing temperature.

The cross-section images of T20H80 samples showed a single layer of oxides and the thickness was uniform. Although the oxide scales were covered by cracks, they were much denser than those for pure HfC. The added TaC would rapidly oxidize and melt under current testing conditions. The liquid phase of Ta_2O_5 with solid frame HfO_2 structure improved the oxidation resistance. The thickness of the oxide scales in T20H80 samples reduced by more than 50% as compared to pure HfC oxidation. From the cross-section images, the grain shapes could still be seen, so the grain boundaries were the preferential diffusion pathway as well for T20H80 samples. Since the testing temperature was high enough, the resultant HfO_2 could be sintered, and the liquid Ta_2O_5 serve as a sintering aid. As a result, the oxide scales in T20H80 samples were denser than those in pure HfC samples.

Figure 4.15: Top surface of the T20H80 after oxidation tests. Low magnification (a) 1 min, (b) 3 min, and (c) 5 min. High magnification (d) 1 min, (e) 3 min, and (f) 5 min

Figure 4.16: Cross-section of the T20H80 after oxidation tests. Low magnification (a) 1 min, (b) 3 min, and (c) 5 min. High magnification (d) 1 min, (e) 3 min, and (f) 5 min

4.3.2.3 The Morphologies of T50H50 Top Surface and Cross-Section

The top surfaces for T50H50 were dense and crack-free. Long straight lines left by the grinding process could be spotted in all the samples' surface, suggesting the oxidation was not severe for all the three time durations. Low magnification images showed the sign of melting and some micro-cracks as the results of gaseous products.

The cross-section pictures of the T50H50 post-oxidation samples showed a very dense oxide scale. The oxide scales and residual carbides had distinct interfaces, and no other layers could be found in the scales. Some cracks still can be spotted inside the oxide scales of the three time durations. But crack-healing can also be observed as the oxidation proceeded. Such thin oxide scales indicating a protective oxidation mechanism was dominant during the T50H50 oxidation. The XRD analysis revealed a hafnium carbide oxide formed during the oxidation testing, which was responsible for this promising oxidation resistance. A detailed description will be provided in the next section.
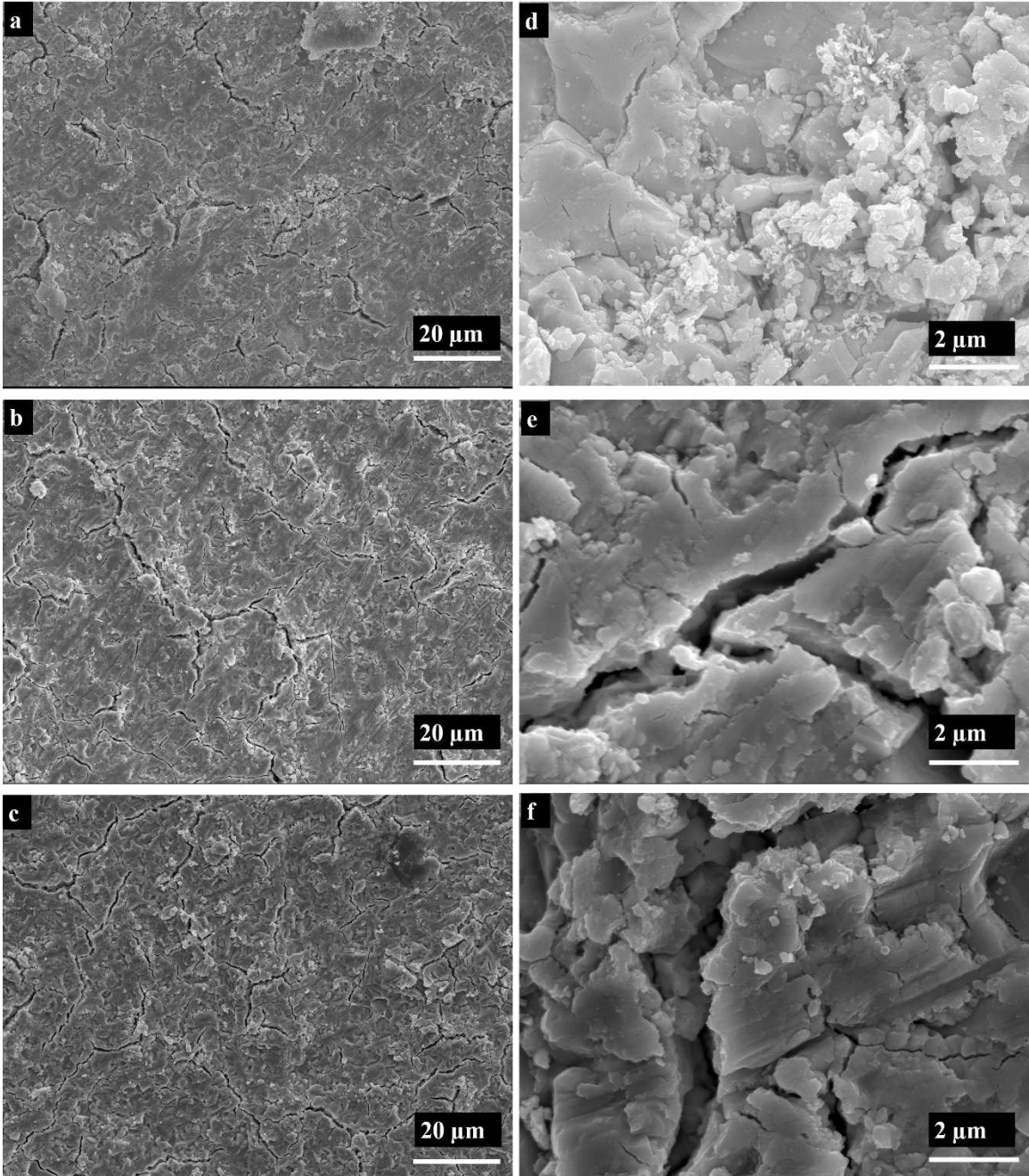
Figure 4.17: Top surface of the T50H50 after oxidation tests. Low magnification (a) 1 min, (b) 3 min, and (c) 5 min. High magnification (d) 1 min, (e) 3 min, and (f) 5 min
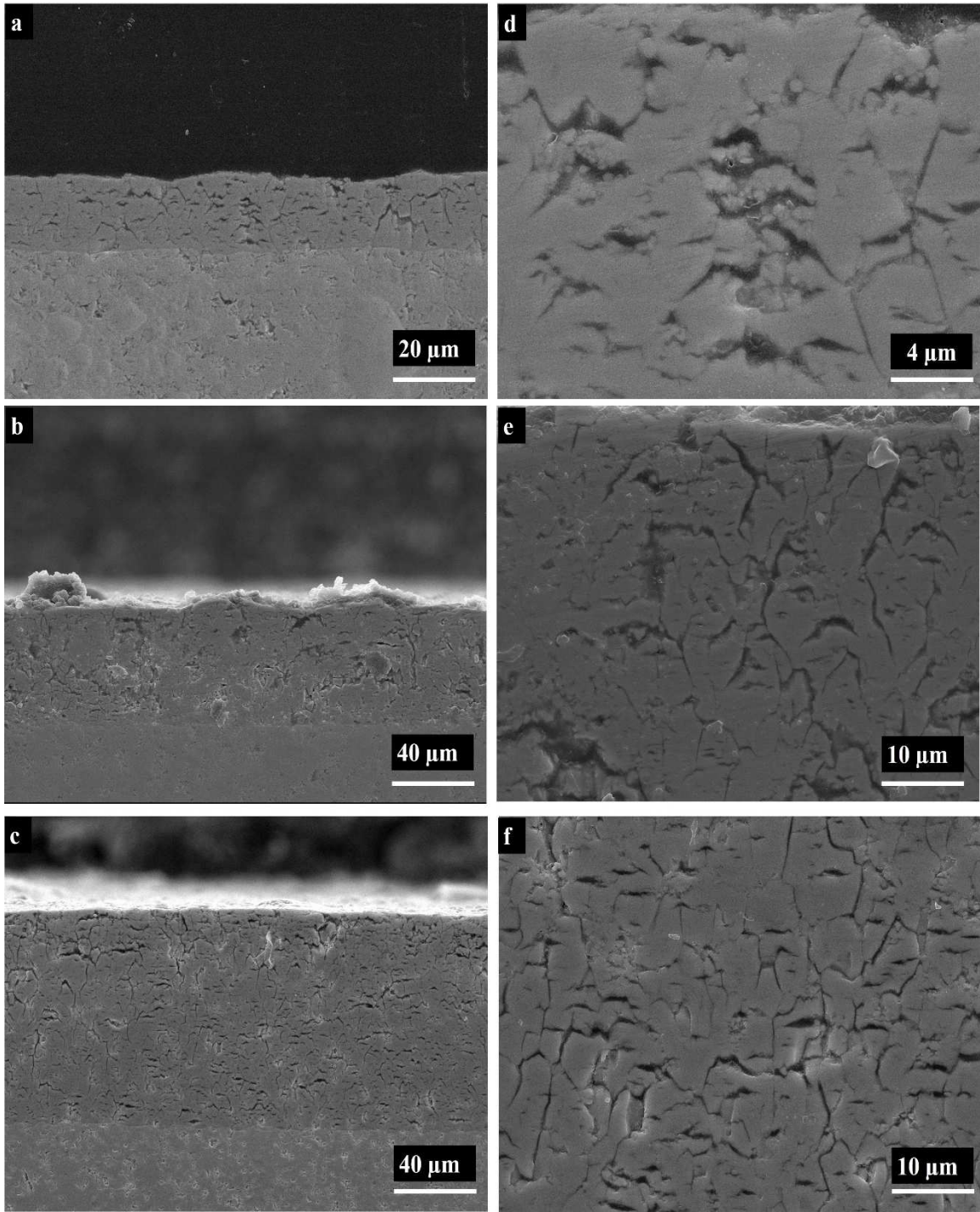
Figure 4.18: Cross-section of the T50H50 after oxidation tests. Low magnification (a) 1 min, (b) 3 min, and (c) 5 min. High magnification (d) 1 min, (e) 3 min, and (f) 5 min

4.3.2.4 The Morphologies of T80H20 Top Surface and Cross-Section

The top surfaces of T80H20 were similar to the surfaces of T20H80 samples. The surfaces were flat and covered by cracks. Besides the cracks, spallation was also noticed in the surfaces and intensified with the increase of testing time duration. The spallation caused much larger opening than just the cracks did, and the opening created a pathway for oxygen diffusing deeper in the samples.

Although the cross-section of T80H20 samples suggested the oxide scales were full of cracks, but no sign of delamination was observed, the scales remained intact in all the three cases. The high magnification images showed few deep cracks crossed the scale thickness, which was identified as a gaseous pathway and cracking caused by thermal mismatch upon cooling. In the 5 min testing sample, signs of liquid attacking were spotted indicating massive liquid phase generated during the oxidation testing. Such signs of liquid attacking could also be found in T50H50 samples, but T80H20 showed much severe attacking, especially in 5 min testing. This might be due to the low melting point of Ta_2O_5 from the increased amount of TaC. Another interesting characteristic of T80H20 cross-section images was the significant crack-healing. In the 5 min testing sample, the oxide scale was dense and without any obvious cracks or pores. This phenomenon could also be explained by the liquid phase formation, which will be elaborated in the following text.
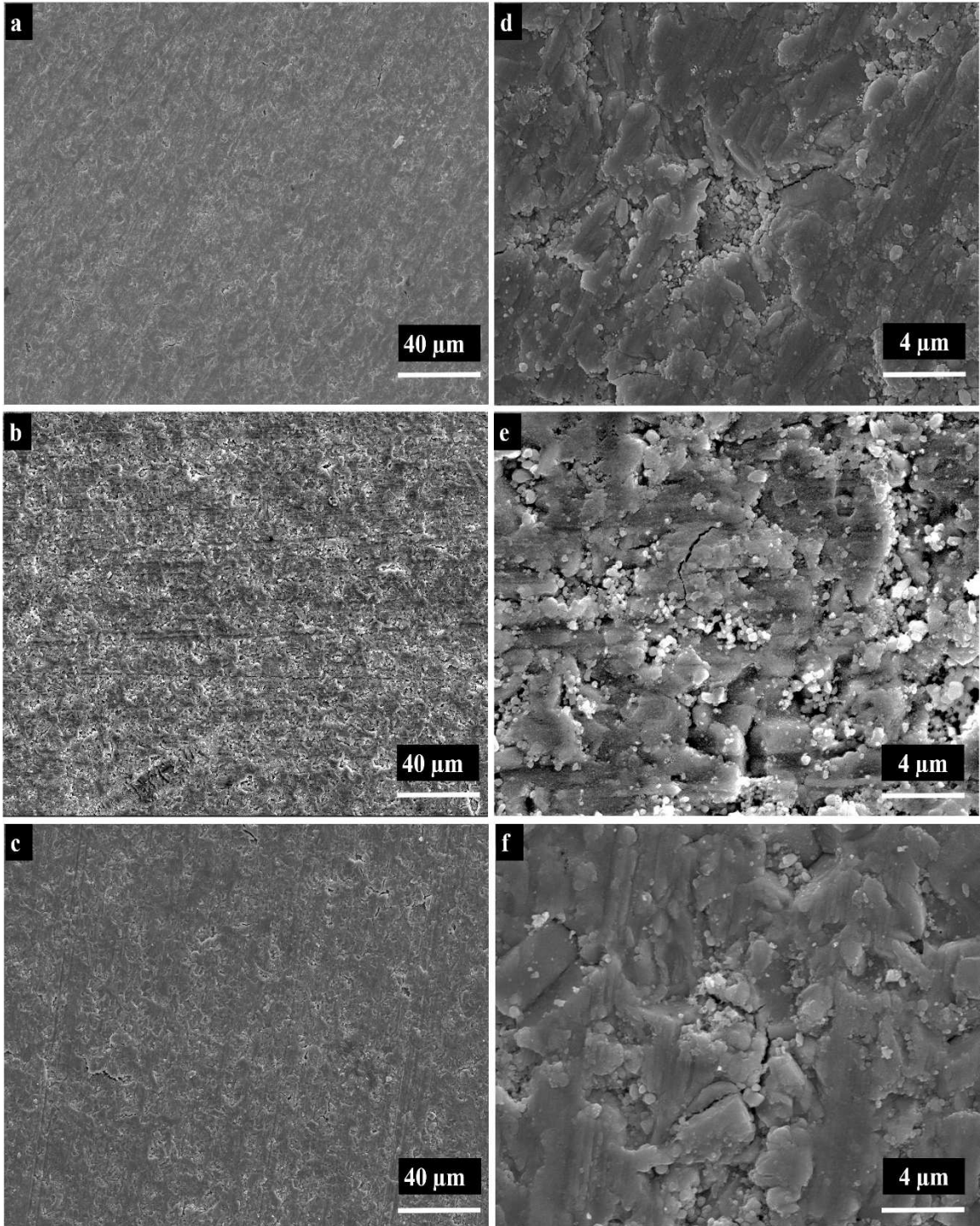
Figure 4.19: Top surface of the T80H20 after oxidation tests. Low magnification (a) 1 min, (b) 3 min, and (c) 5 min. High magnification (d) 1 min, (e) 3 min, and (f) 5 min
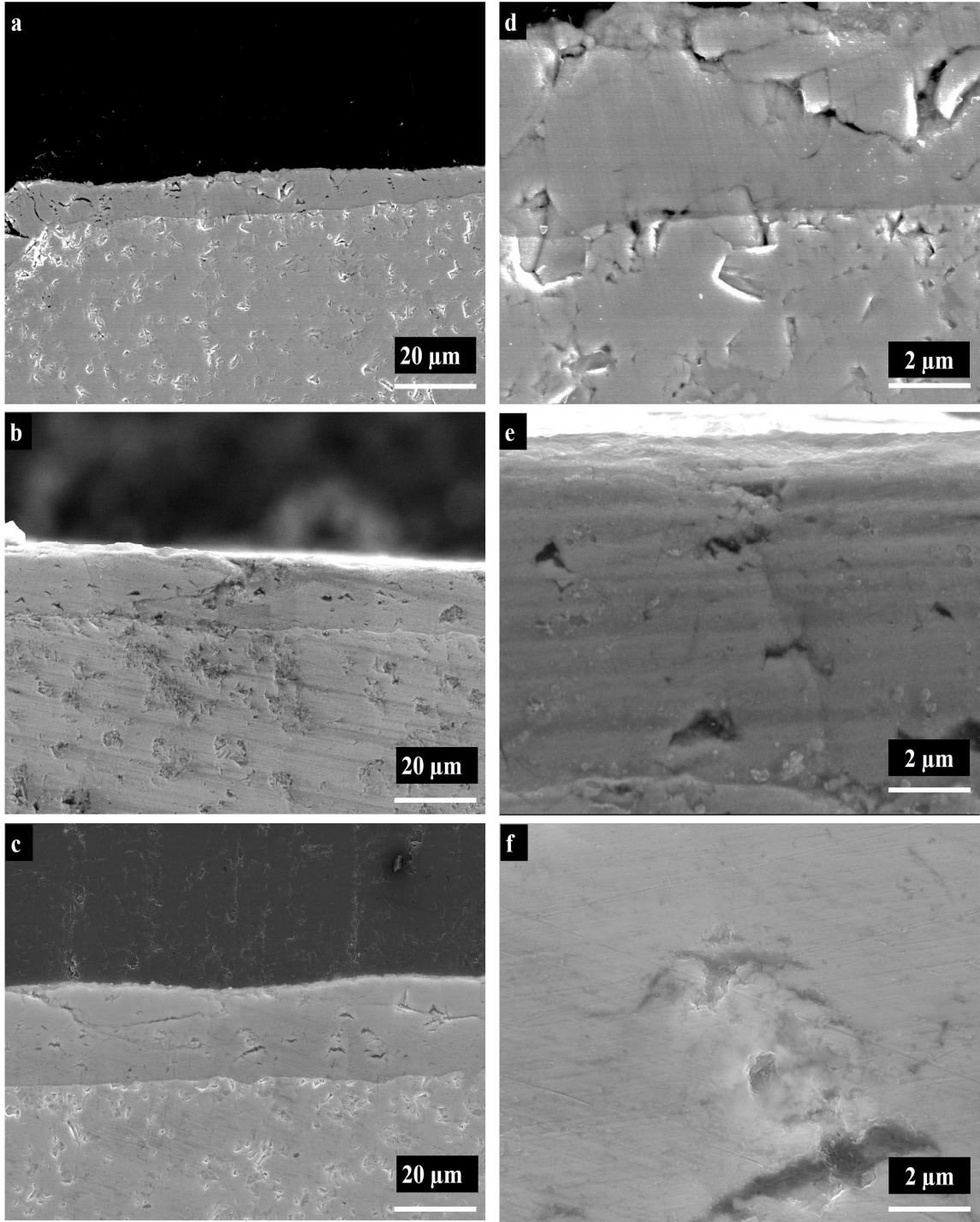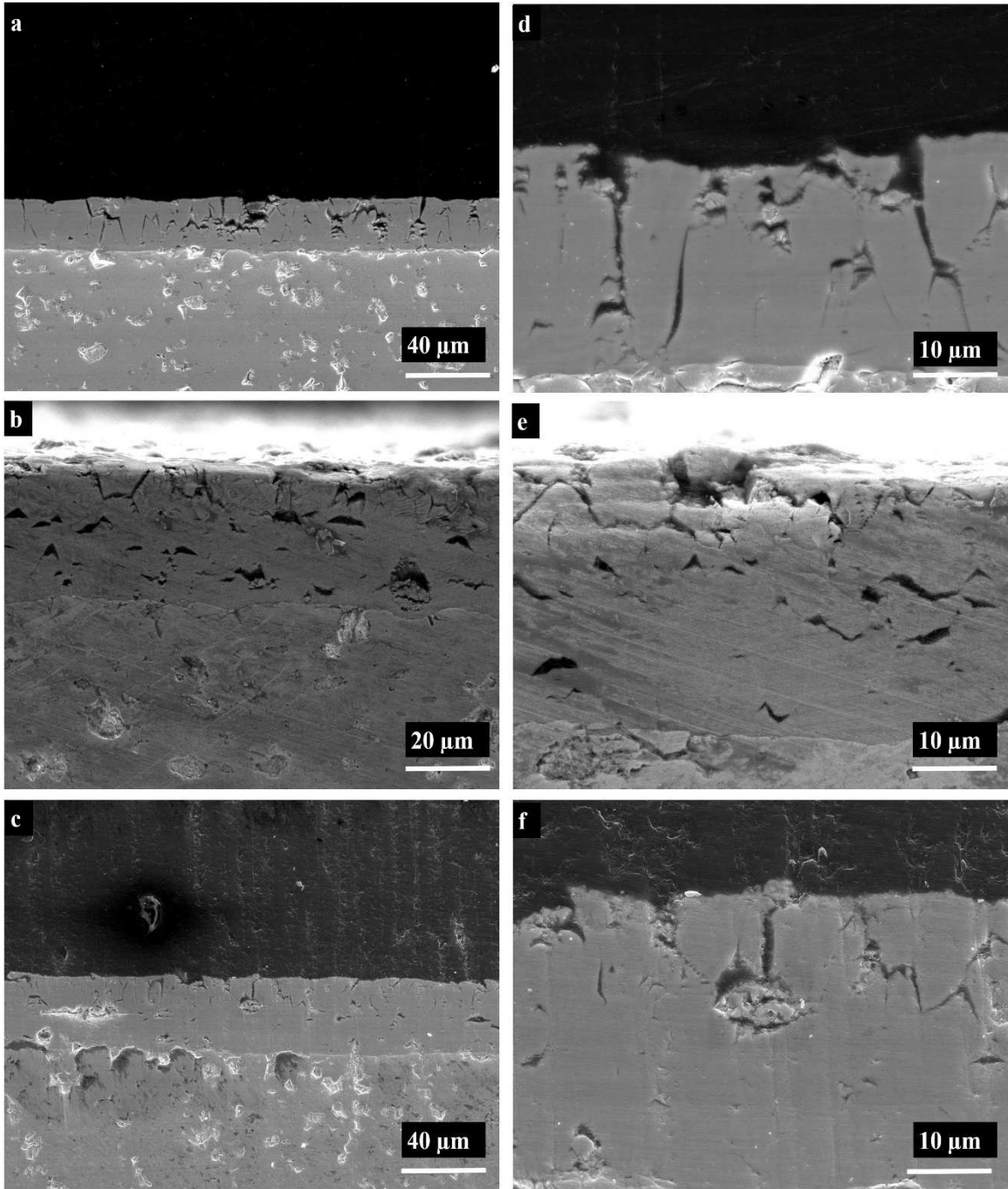
Figure 4.20: Cross-section of the T80H20 after oxidation tests. Low magnification (a) 1 min, (b) 3 min, and (c) 5 min. High magnification (d) 1 min, (e) 3 min, and (f) 5 min

4.3.2.5 The Morphologies of Pure TaC Top Surface and Cross-Section

The quality of the top surfaces of TaC samples was the worst among all the five samples. They not only were full of cracks and pores but also showed delamination. The 1 min testing top surface was loose but still intact. Delamination started occurring in 3 and 5 min testing. The surface became irregular and uneven. The excessive gaseous products lifted the surfaces and disrupted the integrity of the oxide scale. The high magnification images showed some sub-micron grains. The sub-micron grains came from the re-crystallization of Ta_2O_5 or other tantalum oxides upon cooling. The defects in the oxide layers provided the nucleation sites and resulted in sub-micron grains.

The cross-section morphology of pure TaC is similar to the top surfaces. Numerous cracks and pores were observed as a result of gaseous products. No crack-healing has been observed. Instead, the oxide scale was totally lifted and destroyed. The Ta_2O_5 did not provide any protection to the underlying carbide against oxidation. Tantalum carbide would definitely not be suitable for use in the extreme conditions.
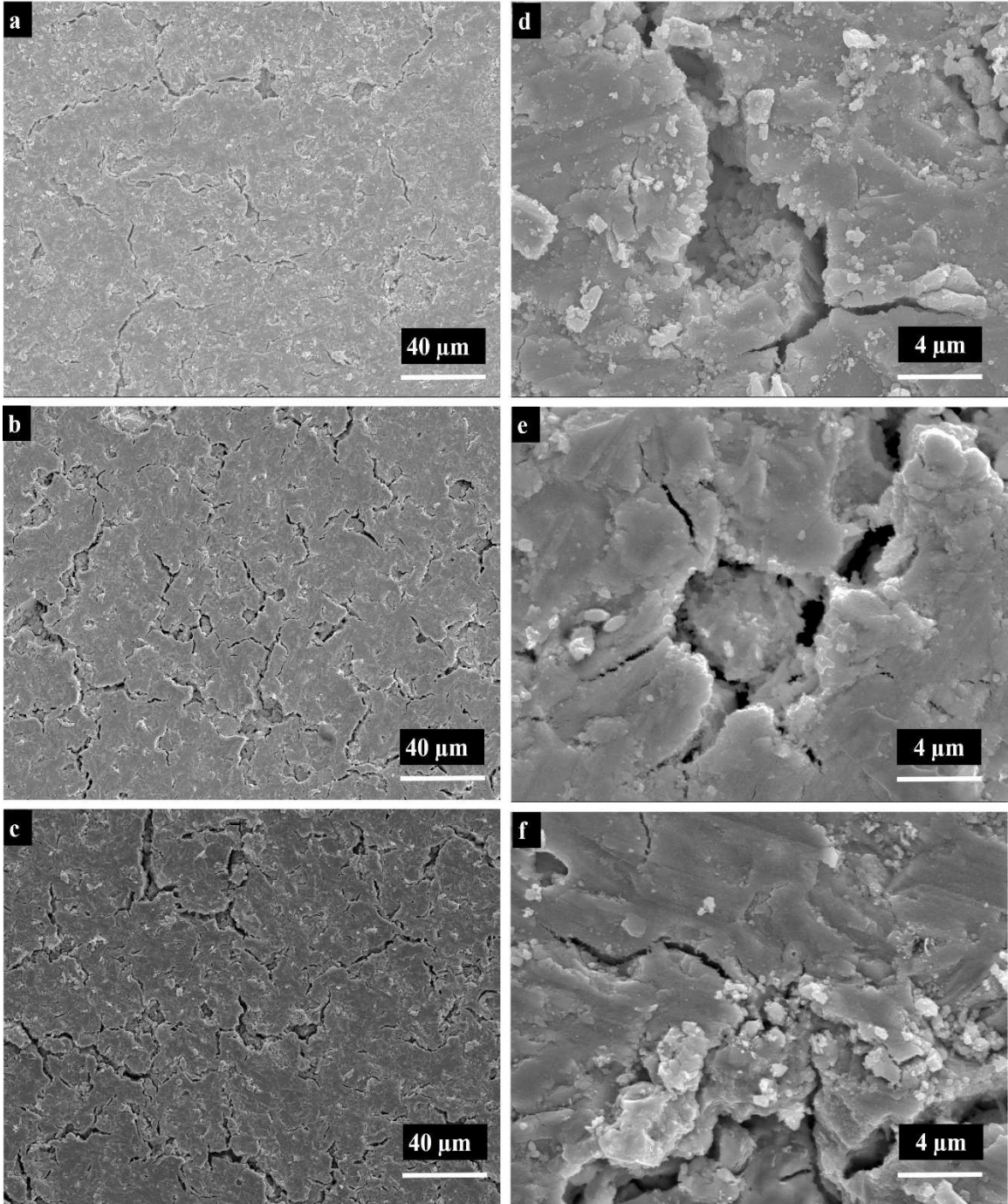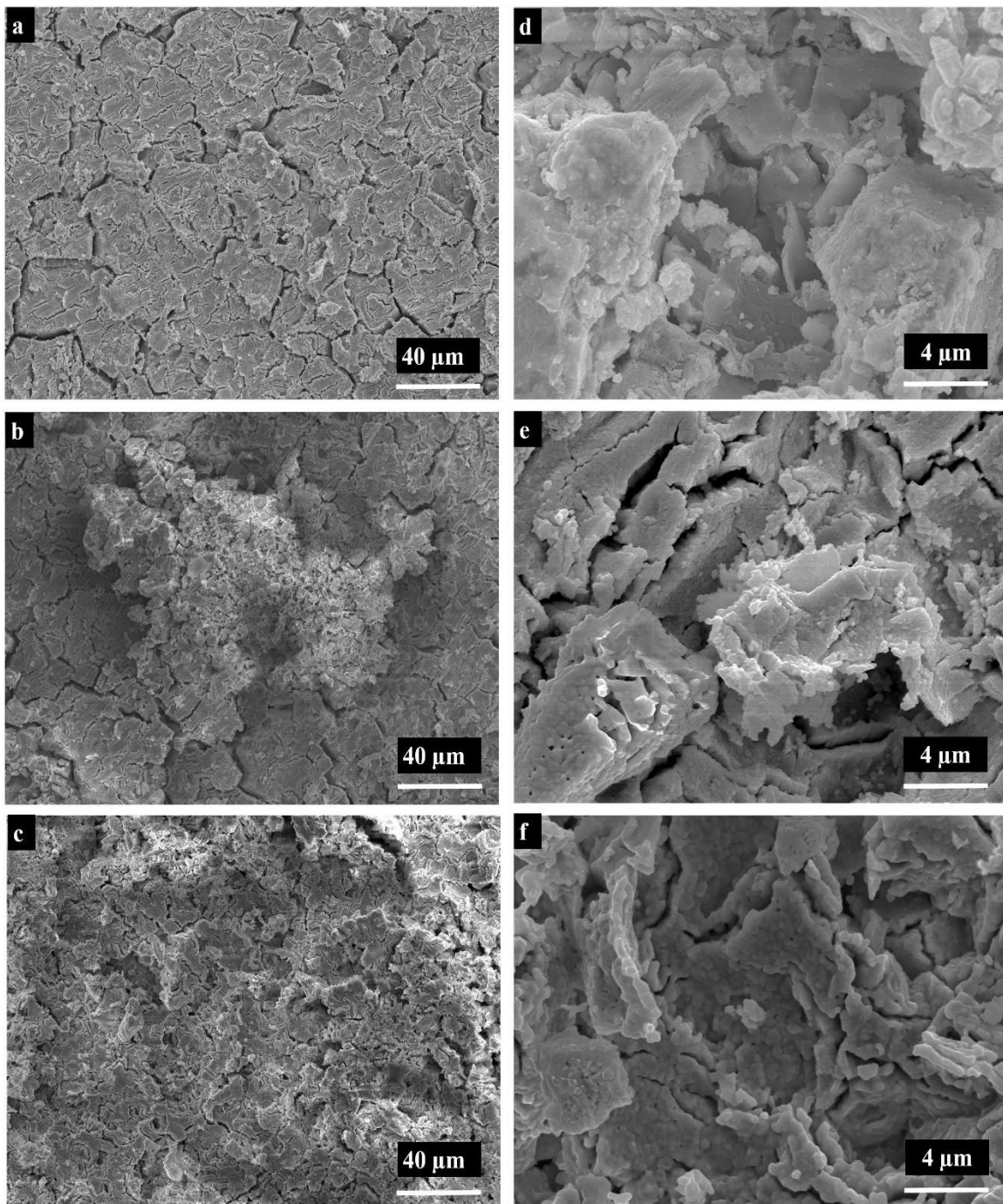
Figure 4.21: Top surface of the pure TaC after oxidation tests. Low magnification (a) 1 min, (b) 3 min, and (c) 5 min. High magnification (d) 1 min, (e) 3 min, and (f) 5 min
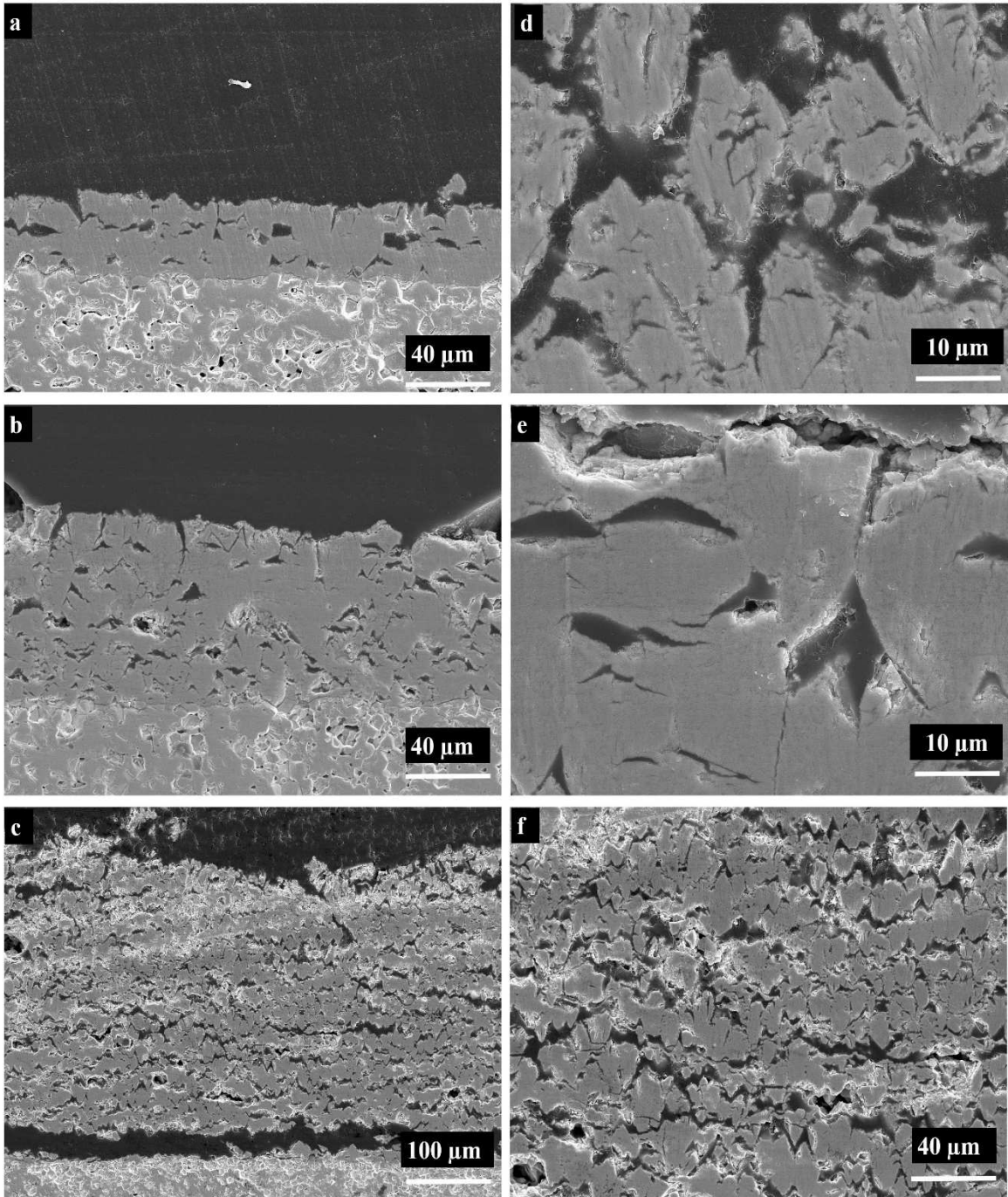
Figure 4.22: Cross-section of the pure TaC after oxidation tests. Low magnification (a) 1 min, (b) 3 min, and (c) 5 min. High magnification (d) 1 min, (e) 3 min, and (f) 5 min

93

4.3.3 Oxidation Scale Phase Evaluation

Three samples for each composition have been evaluated by XRD analysis to identify the oxide phases. The results are shown below:

4.3.3.1 Phase evaluation on the pure HfC post-oxidation samples

The XRD results of three HfC oxidation samples are shown in Figure 4.23. The XRD patterns for the three samples are identical and indexed as monoclinic hafnium oxide (00-034-0104). This HfO_2 is recognized as the low temperature form of hafnium oxide. The phase transformation from high temperature form to low temperature form is always accompanied by volume changes. In an earlier report, [108] the morphologies of the HfO_2 from HfC oxidation which experienced phase transformation and the one without phase transformation did not show any difference. So the author concluded that the phase transformation did not lead to the crack formation, and the plasticity of HfO_2 at high temperature accommodated the volume changes.

Figure 4.23: XRD patterns of HfC oxidized samples

4.3.3.2 Phase Evaluation on the T20H80 Post-Oxidation Samples

The XRD patterns for T20H80 samples after oxidation are shown in Figure 4.24. With 20 vol. % of TaC addition, the post-oxidation phases showed a mixture of HfO_2 and $Hf_6Ta_2O_{17}$. The phase's information matched the early oxidation work on the oxidation of HfC-TaC solid solutions. There is no substantial difference between the samples for the three time durations.

Figure 4.24: XRD patterns of T20H80 oxidized samples

4.3.3.3 Phase Evaluation on the T50H50 Post-Oxidation Samples

The XRD patterns for T50H50 samples were the same for the three time durations and displayed in Fig. 4. 25. The overall patterns were similar to the ones for T20H80 samples. The major difference was at 22-23° where Ta_2O_5 peak started to appear. This could be due to the increased amount of TaC addition compared to the T20H80 samples. The formation of $Hf_6Ta_2O_{17}$ is the result of the reaction between Ta_2O_5 and HfO_2. At the

extreme testing conditions, individual Ta_2O_5 and HfO_2 can still be detected, suggesting the reaction was blocked by separating the Ta_2O_5 and HfO_2.
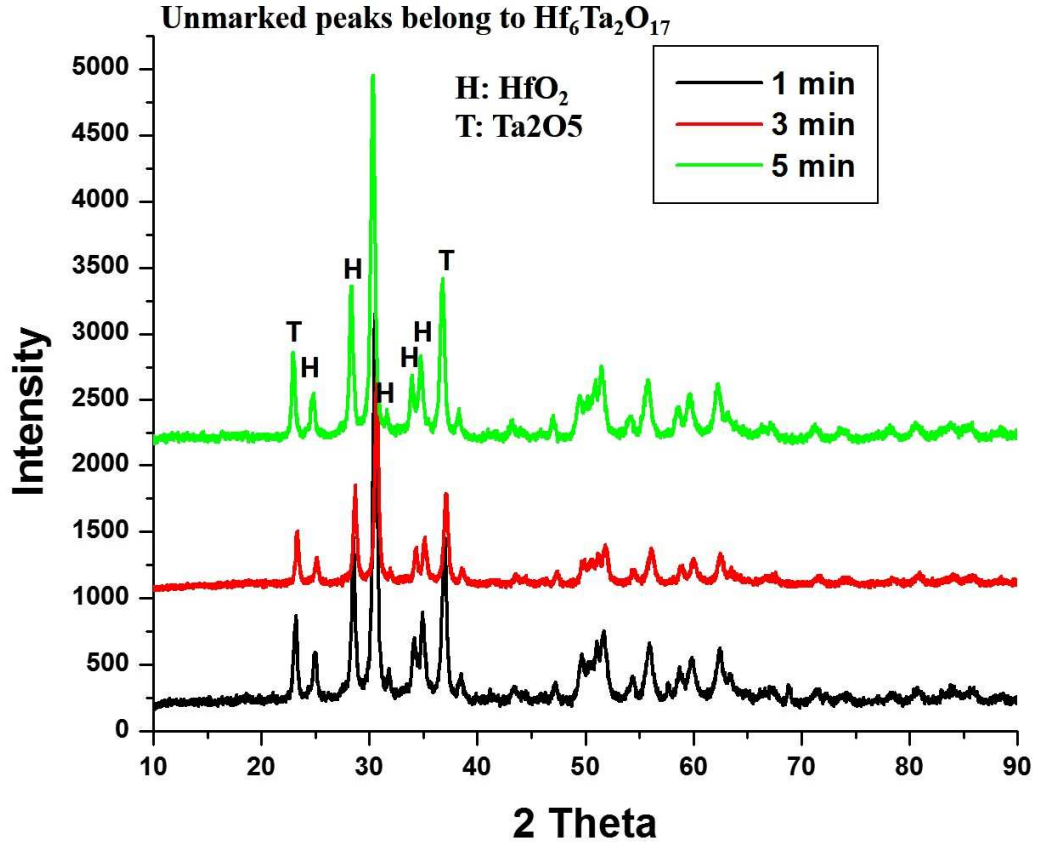
Figure 4.25: XRD patterns of T50H50 oxidized samples

4.3.3.4 Phase Evaluation on the T80H20 Post-Oxidation Samples

The XRD patterns for T80H20 samples after oxidation are shown in Figure 4. 26. At first glance, the XRD peaks for the three time durations were identical. All the peaks were indexed as orthorhombic Ta_2O_5, the low temperature forms of tantalum pentoxide. No presence of HfO_2 was detected. The excessive amount of molten Ta_2O_5 covered the

97

formed HfO_2, which made the latter undetectable to the XRD analysis. This observation also collaborated with the theory of solid scaffold and liquid phase structure. A closer look at 3 min and 5 min tests XRD pattern, as marked by arrows, tiny peaks started to appear and are indexed as $Hf_6Ta_2O_{17}$. The formation of $Hf_6Ta_2O_{17}$ requires more HfO_2 than Ta_2O_5 according to its reaction equation. In the 1 min test, there was not enough HfO_2 formation, so no $Hf_6Ta_2O_{17}$ was detected. Only after 3 min exposure when enough HfO_2 had formed, $Hf_6Ta_2O_{17}$ started appearing on the XRD patterns.
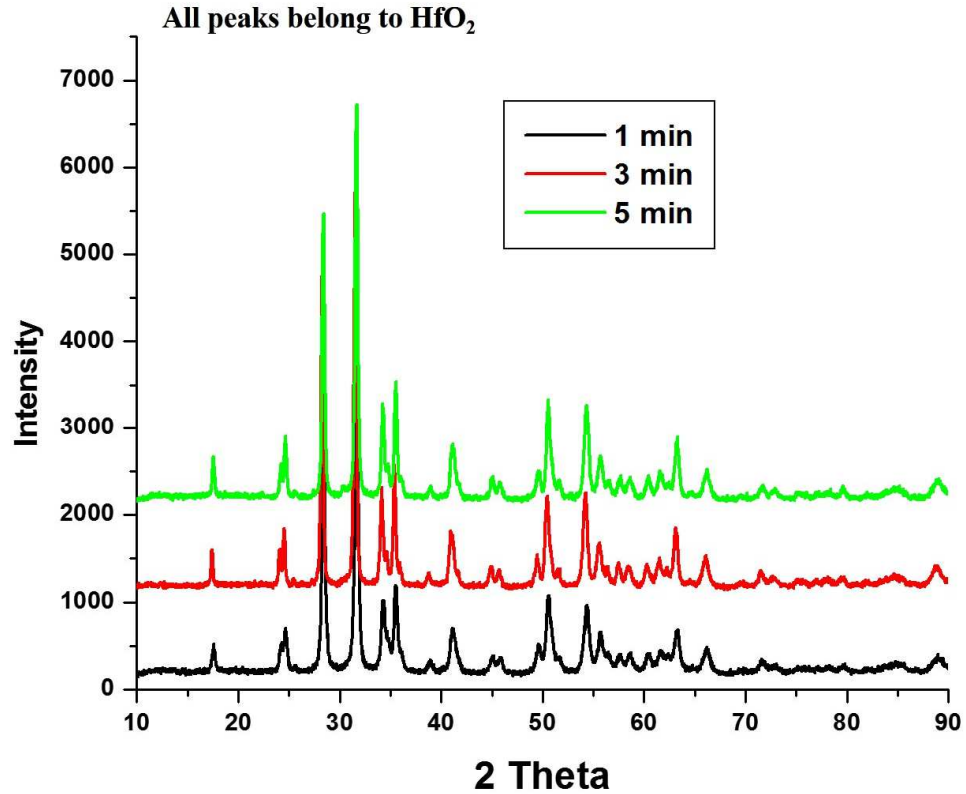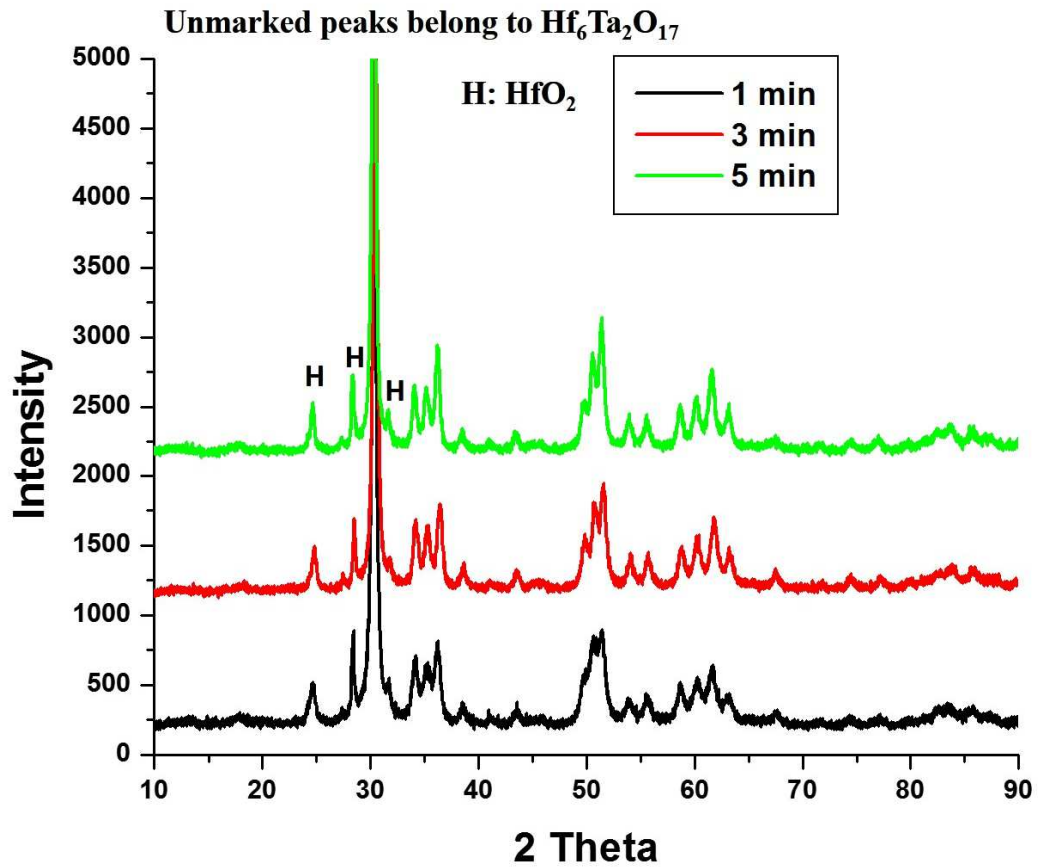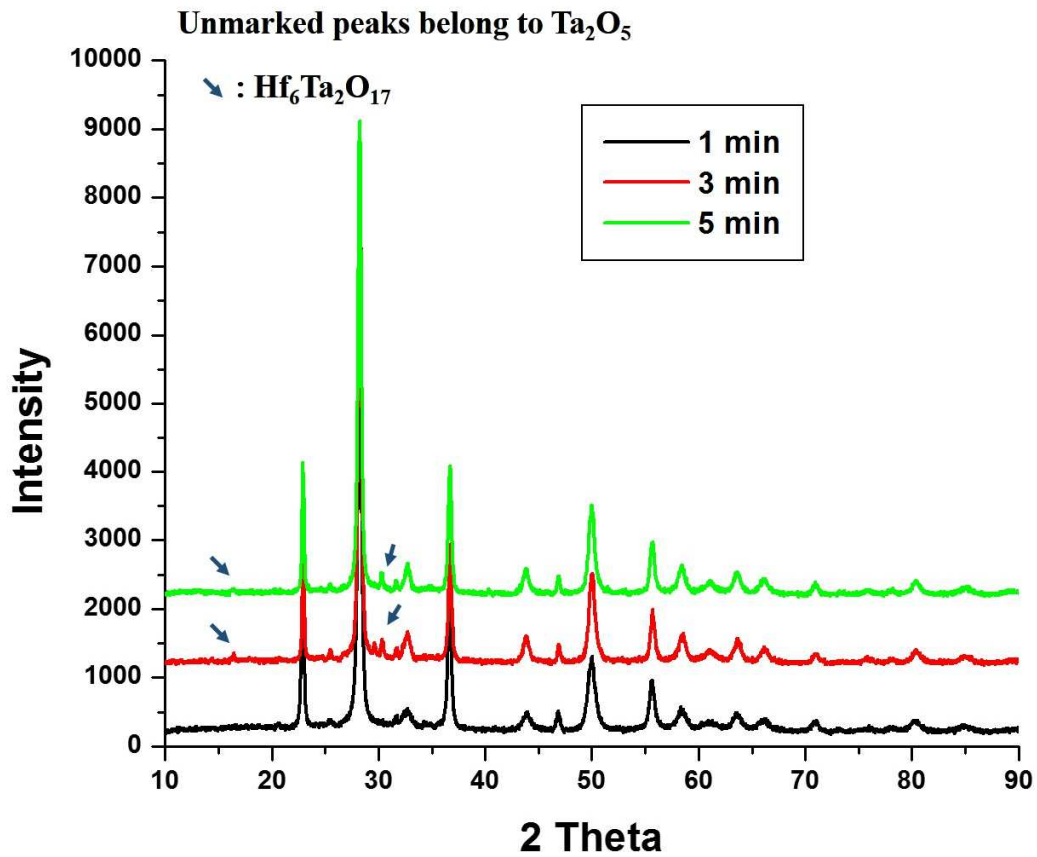

Figure 4.26: XRD patterns of T80H20 oxidized samples

4.3.3.5 Phase Evaluation on the Pure TaC Post-Oxidation Samples

The XRD patterns for pure TaC samples after oxidation are shown in Figure 4. 27. The 1 min and 3 min tests samples are identical and indexed as orthorhombic Ta_2O_5. However, in 5 min test samples, in addition to the orthorhombic Ta_2O_5 phase, triclinic Ta_2O_5 was also detected. The triclinic Ta_2O_5 is reportedly a high temperature form of tantalum pentoxide. The transformation of tantalum oxide from high temperature form to low temperature form was sluggish, so the high temperature form of the oxide can be retained when samples were quenched. Delamination and spallation were severe in 5 min oxidized sample, which provided more pathway to cool air and resulted in high cooling rate.
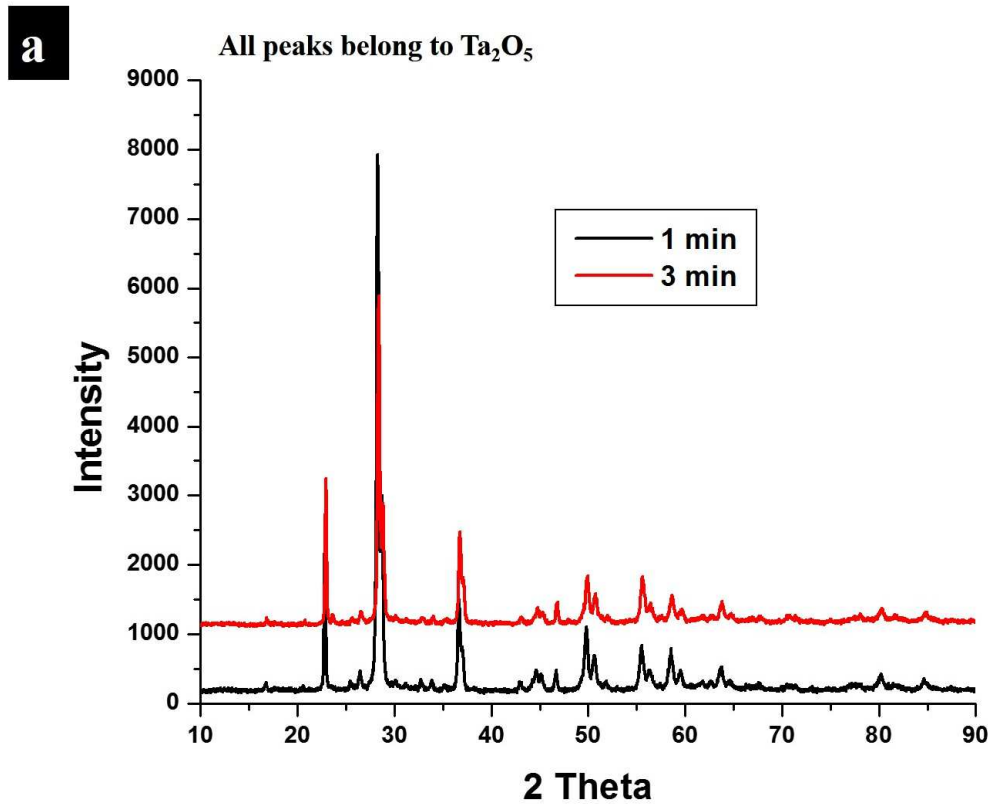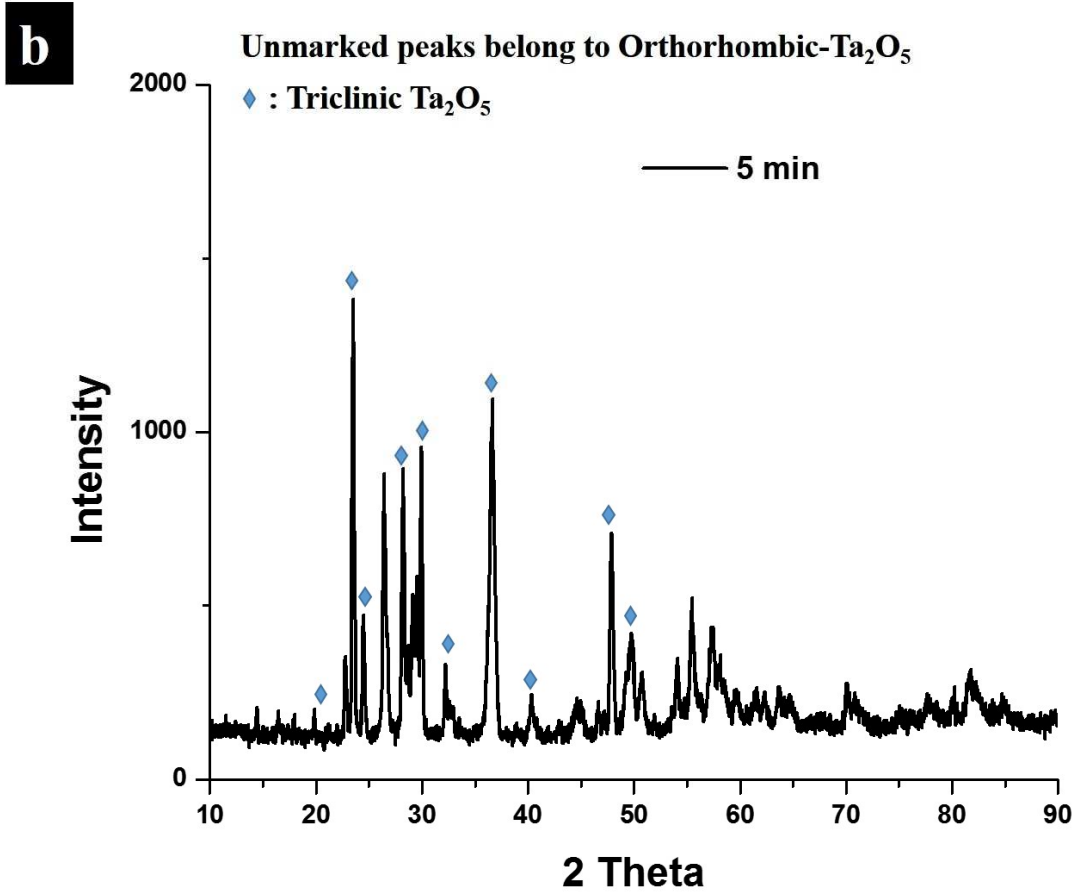
Figure 4.27: XRD patterns of pure TaC oxidized samples. (a) 1 and 3 min samples, and (b) 5 min sample

4.3.4 Back-Side Temperature Measurement During the Oxidation

The back side temperature plots for the oxidation tests are shown in Figure 4.28. The temperature was normalized to their thickness. The thermal conductivities of TaC-HfC were measured and reported by Cedillos-Barraza et al. The results showed the TaC has better thermal conductivity than HfC. The thermal conductivity of TaC-HfC solid solutions decreases with the increasing HfC amount. The higher thermal conductivity

should result in higher measured back-side temperature. The 1 min temperature plot for each sample followed their carbides trend. The pure TaC and T80H20 had the highest measured temperature. Although TaC had better thermal conductivity, the cross-section of TaC oxidized samples revealed its highly porous oxide scale. Combined with the lower densification of pure TaC, the porosity reduced the thermal conductivity of pure TaC oxidized sample, so the measured temperature was similar to T80H20 sample. In 3 min and 5 min tests, the thermal gradient of the pure TaC dropped after 60s oxidation exposure in both time durations. Based on the analysis of TaC oxidation behavior, the decline in the measured temperature could be the result of the delamination or spallation of the tantalum oxide. It also suggests the oxide scale of pure TaC could only remain intact for 1 min under the present testing conditions. The cooling curve of pure TaC for 5 min oxidation showed a steep drop, which coincided with the formation of the triclinic Ta_2O_5 caused by quench cooling. In 3 min and 5 min tests, the measured temperature was lower than pure HfC, but T20H80 had better thermal conductivity than HfC according to the literature. This can be related to the lower thermal conductivity of $Hf_6Ta_2O_{17}$ as compared to HfO_2. Also, in 3 min and 5 min tests, T80H20 showed slight dips in both thermal gradient curves around 150 s. This could be attributed to the formation of $Hf_6Ta_2O_{17}$ which has lower thermal conductivity than HfO_2. Although the melting point of $Hf_6Ta_2O_{17}$ is unclear at this point, its melting point should be in between Ta_2O_5 and HfO_2 deduced from the ZrO_2-HfO_2 mixed oxides [125]. The reactant Ta_2O_5 in the formation of $Hf_6Ta_2O_{17}$ was in the liquid state; it is very likely that after the formation of $Hf_6Ta_2O_{17}$, the liquid phase is consumed and forms solid state $Hf_6Ta_2O_{17}$. The $Hf_6Ta_2O_{17}$ later melts due to the high temperature, and consequently the thermal gradient recovers to the original level. The reaction occurred at

around 150s, so $Hf_6Ta_2O_{17}$ phase was not enough to be detected by XRD in 1 min and 3 min tests. The $Hf_6Ta_2O_{17}$ formation was rapid and occurred at the early stage of the oxidation process; the dips were not observed in the other solid solution samples.
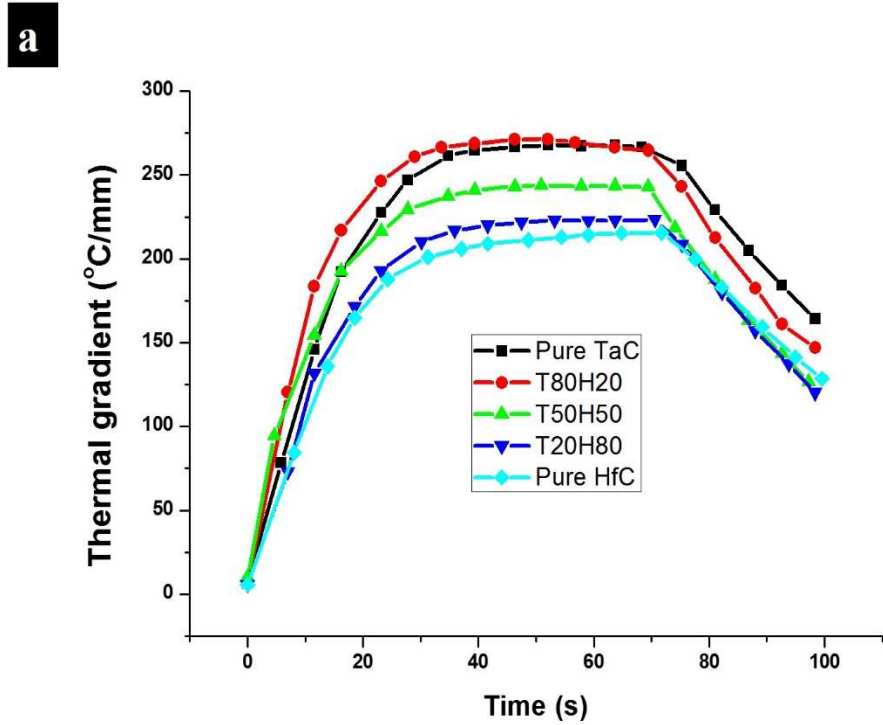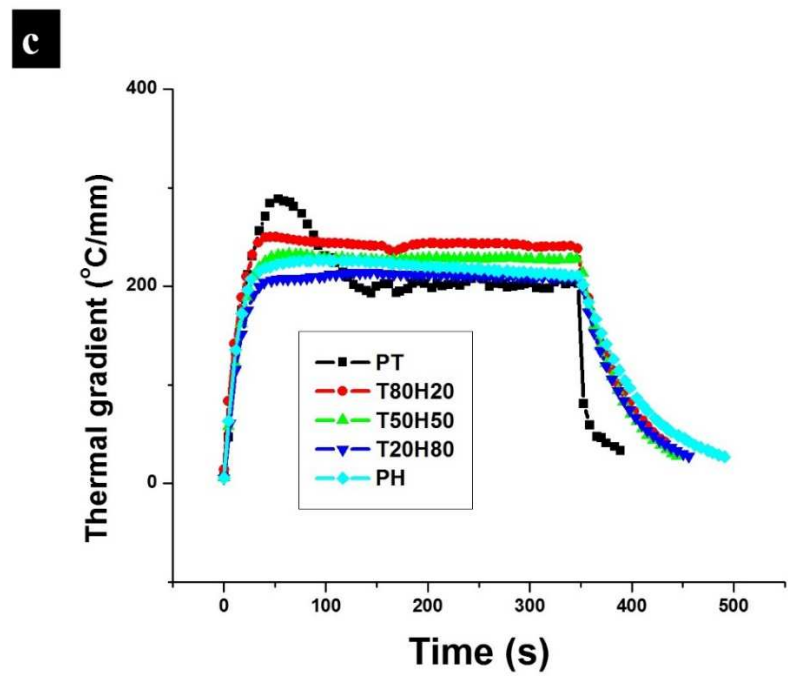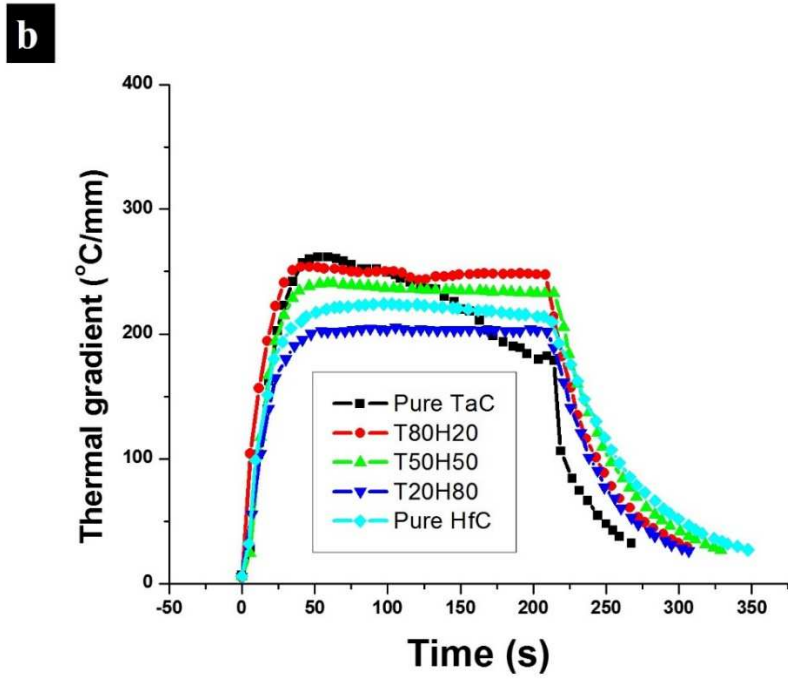
Figure 4.28: Back side temperature plots: (a) 1 min, (b) 3 min, and (c) 5 min

103

4.3.5 Oxidation Mechanisms and Models

The oxidation of pure HfC and pure TaC have been investigated by different researchers. Due to the different testing conditions, the proposed mechanisms and models cannot be directly applied to the current study. In the oxidation of pure HfC samples, it was believed that the oxidation process begins with the absorption of oxygen, followed by the diffusion of oxygen through the grain boundaries and formed HfO_2 and grain surfaces. With the help of thermal mismatch and gaseous products, cracks occur and create new pathways for oxygen diffusing deeper into un-oxidized carbides and start a new cycle of oxidation. A similar mechanism can be adopted for the present study. The HfC samples were sintered pellets from powders. Compared to other synthesis methods, sintering would generate more grain boundaries regardless of the densification. The grain boundaries are the preferred diffusion pathway due to their high defects concentration. When the HfC pellets are exposed to the high temperature oxygen flow, the initial oxygen absorption and oxidation are accelerated due to the high temperature. First layer HfC was rapidly oxidized and formed HfO_2. The grain boundaries became vulnerable due to the thermal mismatch between oxide and carbide, and the high vapor pressure from the gaseous products. Such vulnerability led to the formation of cracks and provided pathways for oxygen. With the near sonic speed, the oxygen was pushed through those formed cracks instead of diffuse through the grains to oxidize the underlying carbide, which also explained the reason why there was no oxycarbide layer observed in the present study. As shown in Figure 4.14, the oxide scale in pure HfC samples are granular; each grain is isolated by intermediate gaps. Only a very thin dense layer was seen which matched the description of oxycarbide phase suggesting the high oxygen potential throughout the oxide scale. The grain size of the oxide

scale was found to vary due to the localized sintering. The sintering temperature for material is considered the two third of its melting point. The melting point of HfO_2 is around 2800 °C, and the present oxidation testing temperature was close to its melting point, which could provide enough driving force for the sintering of HfO_2. The sintering of HfO_2 densified the oxide scales, and the low Pilling-Bedworth ratio of HfO_2 allows good adherence to the carbide. As a result, HfO_2 scales remained intact, and no obvious spallation was noticed under the extreme conditions.

Tantalum carbide exhibited poor oxidation resistance in the present study. Not only it had the thickest oxide layer, but its oxide scales were also peeled off from the carbide surfaces. Similar to the oxidation of hafnium carbide, the oxidation process in tantalum carbide began at the grain boundaries. The oxygen diffusion/penetration process was akin to the process in the HfC; cracks and gaps were formed at the grain boundaries and allowed oxidation into the deeper carbide. The difference was the oxygen diffusion pathway into the grains. In case of HfC, after the initial oxidation on the surfaces of the grains, the oxidation of each grain was completed by the oxygen lattice diffusion. However, in the case of TaC, the formed Ta_2O_5 on the grain surface rapidly melted under the high temperature environment and covered the TaC grains. The liquid phase formation hindered the oxygen lattice diffusion, but the liquid layer was far from being protective. It was pointed out that [19] Ta_2O_5 would react with TaC and further oxidize the underneath carbides. The formed Ta_2O_5 cannot withstand the high temperature environment and liquefies during the oxidation process. The gaseous products generated can easily disturb and lift the liquid phase oxide scales, causing massive spallation and cracking. Although liquid phase is considered beneficial to the oxidation resistance, the liquid phase itself

should not react with the parent material. Ta_2O_5 has a low melting point so the liquid phase could form at the early stage of the oxidation, however, the reaction with TaC makes it an unfavorable phase during oxidation. Also without the solid phase structure, the liquid phase would be prone to ablation under the high gas blow. These were the main reason that TaC had worst oxidation resistance in the present study.

TaC-HfC solid solutions had much better oxidation resistance than their monolithic carbides. In the case of T50H50, the oxide scales were not only thin but also highly dense. The thickness of T50H50 oxide scale was 1/10 of the thickness of pure TaC 5 min oxidation, 1/6 of the thickness of pure HfC 5 min oxidation. The oxidation mechanisms for TaC-HfC solid solutions could be deduced from the oxidation mechanisms for oxidation of monoclinic TaC and HfC. In the T20H80 sample, the 20 volume percent TaC was added. During the oxidation, HfO_2 and Ta_2O_5 were formed at the surfaces of the top layer grains. Due to the extreme testing conditions, especially the high temperature, the formed Ta_2O_5 melted and covered on HfO_2 surface. However, like in the pure TaC oxidation case, the formed liquid Ta_2O_5 was not a protective layer against oxidation. It could react with both TaC and HfC and form tantalum sub-oxide and HfO_2. In the XRD analysis on the T20H80 post-oxidation samples, only HfO_2 and $Hf_6Ta_2O_{17}$ were detected without the presence of Ta_2O_5, which implies that the Ta_2O_5 has been consumed by the reaction. The formation of one mole of $Hf_6Ta_2O_{17}$ requires one mole of Ta_2O_5 and six moles of HfO_2, so no Ta_2O_5 would remain with the presence of HfO_2. Additionally, multiple reports suggest that the formation of $Hf_6Ta_2O_{17}$ requires at least 10 hours and the temperature exceeding 1200 °C. Although the current testing conditions accelerated the reaction, $Hf_6Ta_2O_{17}$ can only be formed after the formation of Ta_2O_5 and HfO_2. The $Hf_6Ta_2O_{17}$ formed was a protective

layer against oxidation [116], so the thickness of the oxide scale had reduced up to 65%.

However, the amount of liquid phase formed was not enough to form a continuous liquid

layer and protect the T20H80 samples from oxidation. The cross-section images showed

that though the oxide scales were not as granular as the ones in pure HfC samples, the large

cracks and big gaps still could be seen. Some minor cracks along the grain boundaries

indicate that the same oxidation mechanism is prominent in both pure HfC and T20H80

samples. Additionally, oxide scale sintering occurred, especially in the presence of liquid

phase, explained some large grains found in T20H80 oxide scales.

When 50 volume percent of the TaC was added to T50H50 samples, more liquid

phase was generated during the oxidation. The beginning of the oxidation was the same as

the pure HfC and the T20H80 samples. The XRD patterns showed the mixture of Ta_2O_5,

HfO_2, and $Hf_6Ta_2O_{17}$. As discussed in the eariler, the Ta_2O_5 and HfO_2 could not co-exist,

the Ta_2O_5 should be consumed into the formation of $Hf_6Ta_2O_{17}$ at such high temperature.

However, the XRD resulted suggest otherwise. The only explanation was the formed Ta_2O_5

and HfO_2 were separated. In the T50H50 samples, the Ta_2O_5 formed on the HfO_2 melted

and formed $Hf_6Ta_2O_{17}$. The formed $Hf_6Ta_2O_{17}$ did not react with underlying materials and

also separate the Ta_2O_5 and HfO_2. The stress at the grain boundaries was quickly eased by

the abundant liquid phase, so the oxide scale was much denser compared to the other

samples. Moreover, enough liquid formed during the oxidation which formed a continuous

liquid layer. Two different liquid phases exist in the T50H50 samples resulted in high

viscosity fluid, which could withstand the high gas flow. The formed HfO_2 also provided a

scaffold structure that further stabilized the oxide scales. The gaseous products introduced

some pores, but the damage from the high vapor pressure which caused big cracks in the

other samples was prevented due to the liquid in the scale. Furthermore, the pores inside the oxide scales were sealed over the time as the liquid flowed into such porous areas, which later was observed as crack-healing in the 5 min oxidation sample.

The morphology of T80H20 1 min test sample was similar to the one of pure TaC, but the thickness of the oxide scale of T80H20 was only 45% of the thickness of pure TaC oxide scale. The main difference was the 20 volume percent of HfC in the system. The excessive Ta_2O_5 melted and totally wrapped the HfO_2 grain inside, so the HfO_2 was not detected by XRD. The HfO_2 secured the oxide scale from ablation, and the oxide scale remained intact. Fig 4.29 shows that a single grain was attacked and lifted by the liquid phase indicating the liquid phase prevented the oxygen diffusion, and the oxidation of T80H20 was from the liquid attack to the carbides. In the 3 and 5 min test samples, crack-healing was again noticed, which also verified the existence of HfO_2 that hosted and stabilized the liquid phase. Such "scaffold" structure was not noticed in pure TaC samples, so no crack-healing was noticed. In the 5 min test, the $Hf_6Ta_2O_{17}$ peaks started to appear due to the HfO_2 formation of large amount of HfO_2 generated during the oxidation tests. The liquid layer became more protective against the oxidation, and further crack-healing occurred as seen in the cross-section images.

A model is developed and the schematic is shown in Figure 4.30. The carbides and their solid solutions had a flat surfaces with grains. Oxidation in all cases began with the oxygen attacking the first layer grain through grain boundaries (Step 1, Figure 4.30). Due to the relatively small grain sizes in all samples, and harsh oxidizing conditions, the oxidation of individual grain was not the rate determining process. The oxidation in the present study is dependent on the availability of oxygen. In the case of pure HfC samples,

oxygen penetrated the oxide scales through the cracks created by the thermal mismatch and gaseous products (Step 2, Figure 4.30a). Some liquid phase appeared in the T20H80 samples, the liquid phase was not enough to cover the oxidized surface. Oxygen could still reach to the underlying carbides through the cracks, but much limited compared to the pure HfC samples. The protective layer $Hf_6Ta_2O_{17}$ was also formed, which further protected the carbides from oxidation (Step 2, Figure 4.30b). Sintering of the oxide scales was spotted in the pure HfC and T20H80 samples due to the extreme high temperature. Sintering in the oxide scales were beneficial to the structural integrity. In the T50H50 samples, enough liquid was generated, so the oxygen penetrating pathway was blocked. The oxidation process was driven by the chemical reactions between the liquid phase (Ta_2O_5) and residual carbides (Step 3, Figure 4.30b). Furthermore, decent considerable amount of $Hf_6Ta_2O_{17}$ formed during the oxidation. It not only serves as a protective layer, but also blocks the contact between Ta_2O_5 and the residual carbides. However, $Hf_6Ta_2O_{17}$ also retarded its own formation from the reaction between Ta_2O_5 and HfO_2. Due to the large amount of liquid phase formed in T80H20, the morphology of the oxide scales was similar to the pure TaC. The HfO_2 covered by Ta_2O_5 provided frame for the liquid, so that the liquid would not be pushed away by the high velocity gas flow. After 5 min exposure, the $Hf_6Ta_2O_{17}$ appeared and provided extra protection against oxidation. Crack-healing (Step 5, Figure 4.30b) was observed in T50H50 and T80H20 samples due to the large amount of liquid and HfO_2 scaffold. The oxide scales in the pure TaC samples were similar to the "Boiling water". Excessive amount the liquid and gaseous products generated during the oxidation resulted in the worst oxidation resistance of TaC. Spallation and delamination occurred

especially in 5 min samples causing the sample to experience quench cooling. The high

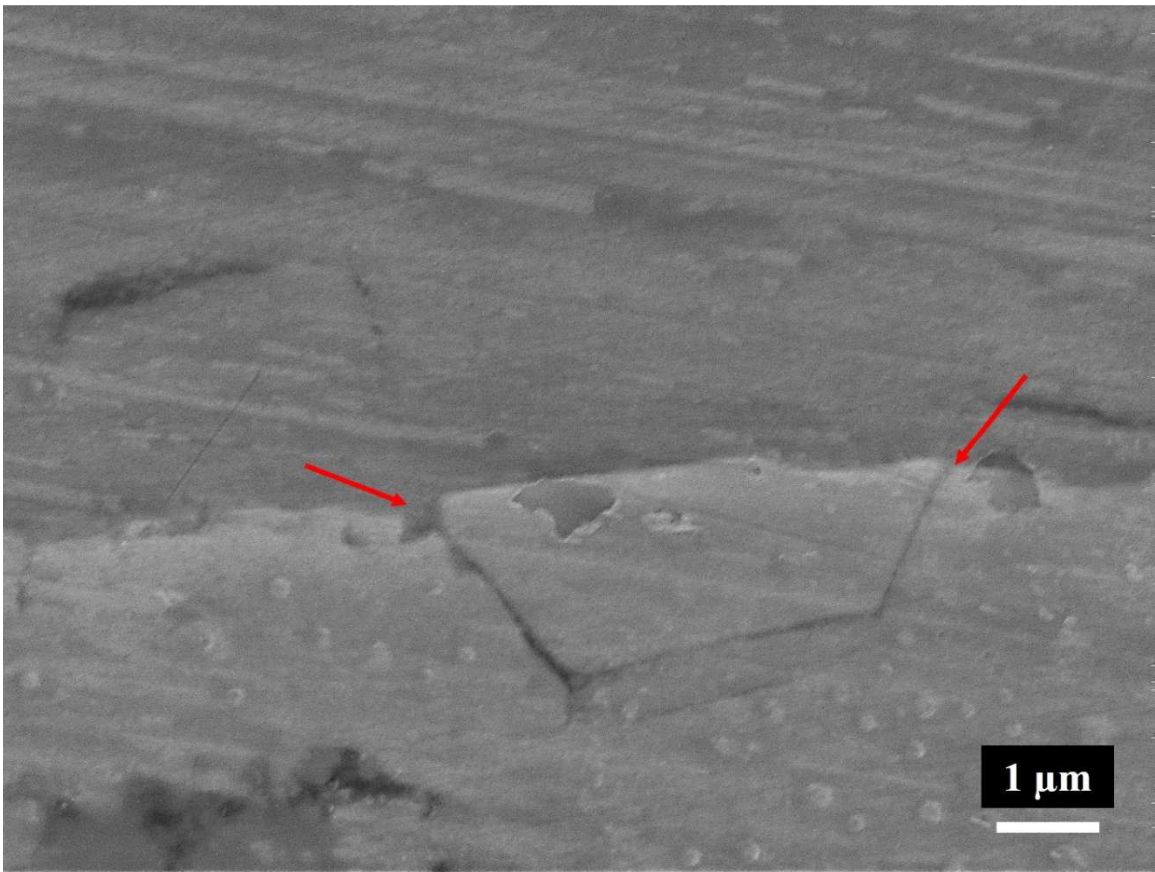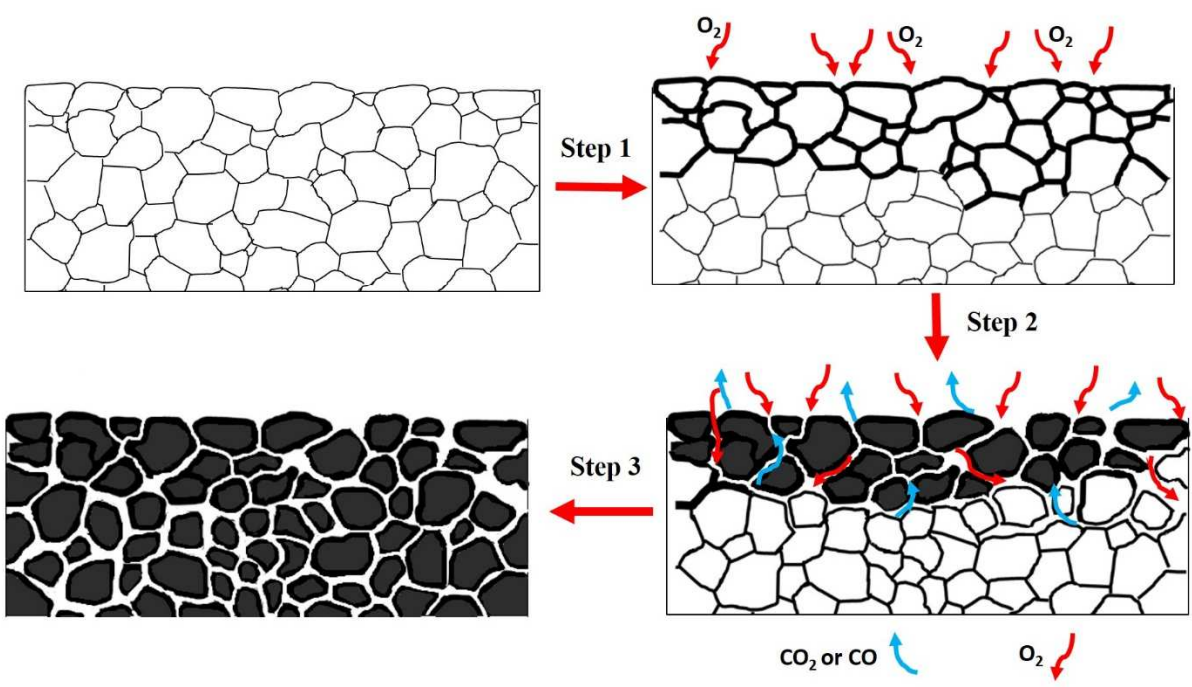temperature form of Ta_2O_5 was retained and detected by XRD analysis.

Figure 4.29: Liquid phase attacking on the underlying carbides
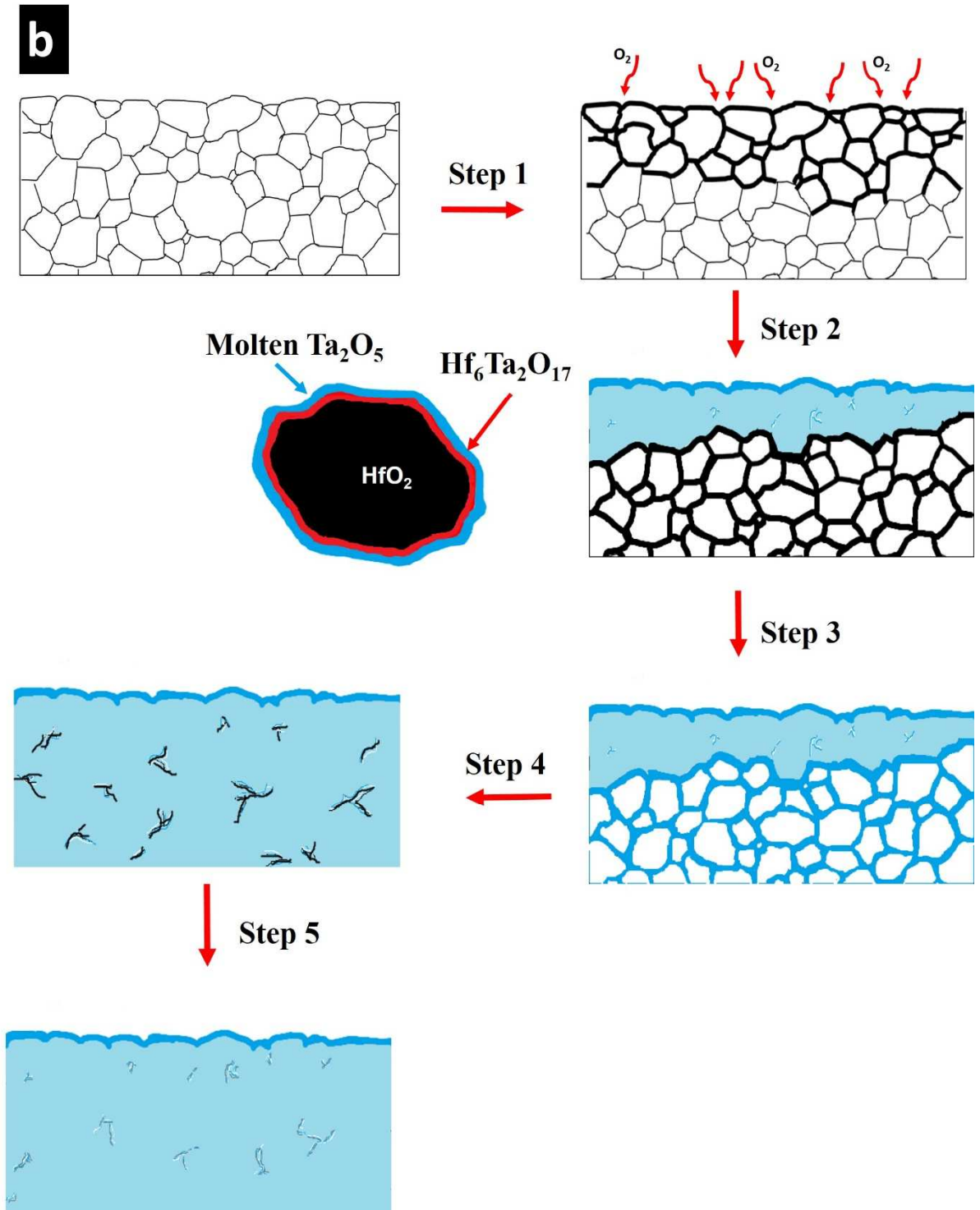
Figure 4.30: Oxidation schematic for (a) Pure HfC, and (b) solid solution samples

4.3.6 Effect of the Formation of the Solid Solution on the Oxidation Behavior

In the present study, the oxidation behaviors of TaC-HfC solid solutions were investigated. The advantages of solid solutions compared to the composites became clear after the detailed analysis. The oxidation resistance increased in the TaC-HfC solid solution samples due to the liquid phase formation, especially the $Hf_6Ta_2O_{17}$ which was considered the main reason for the advanced oxidation performance. In the solid solution samples, the oxide products: Ta_2O_5 and HfO_2 were generated and remained in contact. Closed contacted two oxides promoted the formation of $Hf_6Ta_2O_{17}$. In the composites, on the other hand, the Ta_2O_5 and HfO_2 formed and separated, making the formation of $Hf_6Ta_2O_{17}$ and a continuous liquid layer more difficult. The study on the absorption of oxygen on TaC and HfC suggest that the oxygen tends to sit on the Hf- C bridge, and further formed HfO_2 and CO. In the case of TaC, the preferential oxygen site was on the Ta-Ta bridge. When forming a solid solution, the oxidation of Hf element was not affected. However, the Ta atoms were partially replaced by Hf atoms, so the availability of Ta-Ta was disturbed. As a result, the formation of Ta_2O_5 was delayed, and the formation of HfO_2 was unaffected. In the oxidation of solid solutions, the formation of HfO_2 was guaranteed. Otherwise, the excessive molten Ta_2O_5 would hinder the oxidation of HfC. The HfO_2 is crucial to the stability of the oxide scales as it provides the scaffold to the oxide scale. So the solid solutions should have superior oxidation resistance than the TaC-HfC composites.

4.3.7 The Evaluation on the Reusability of the Post-Oxidation Samples

The evaluation on the reusability of the post-oxidation samples will be carried out in different ways, including both high and low load indentation, and oxidation testing on the oxidized samples. In the present work, nano-indentation (NI) testing was conducted on the top surface of the oxidized samples from the 3 min testing. The purpose of these tests was to assess the integrity of the oxide scales on the post-oxidation samples. Instead of getting elastic modulus and hardness values from NI tests, the present work investigated the shape of the loading curves based on our previous work [126]. The curves obtained from NI tests are shown in the Figure 4.31 and the average indentation depth is tabulated in the Table 4. 3. Pure carbides had the largest average indentation depth, which can be deduced from their cross-section images: pure HfC had an oxide scale with granular structure with inter-connected pores, and pure TaC had a porous oxide scale with serve delamination. Both structures would not be able to withstand the external loads, which resulted in a discontinued curves in the loading segments of pure TaC and pure HfC samples. The discontinuity occurred when the tip indented at a porous area, which caused a large displacement and minor increased load. Large standard deviations also indicated that the oxide scales are extremely un-uniformed. The oxide scales of the solid solution samples, on the other hand, showed much more improved integrity, by exhibiting the smoother loading curves and reduced the total displacement. The results advocate the formation of the liquid phases during the oxidation tests which filled the pores in the oxide scales, resulted in a dense and continuous structure. Such structure will not only withstand the impact that hypersonic vehicles may face after entering the Earth orbit, but also have large potential to be reused.

114

c

T50H50

Load (μN) vs Displacement (nm)

d

T80H20

Load (μN) vs Displacement (nm)

116
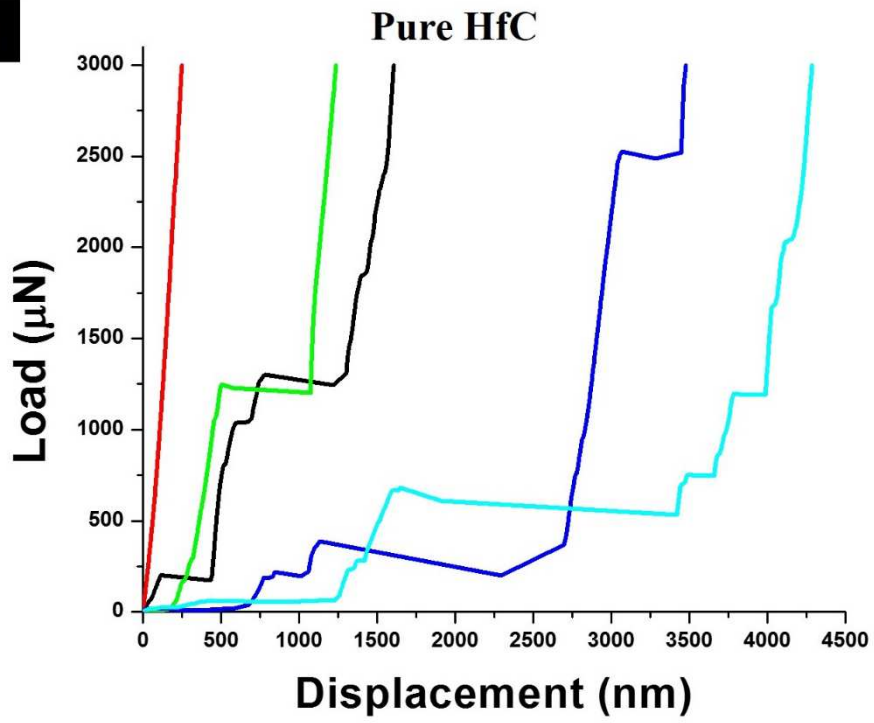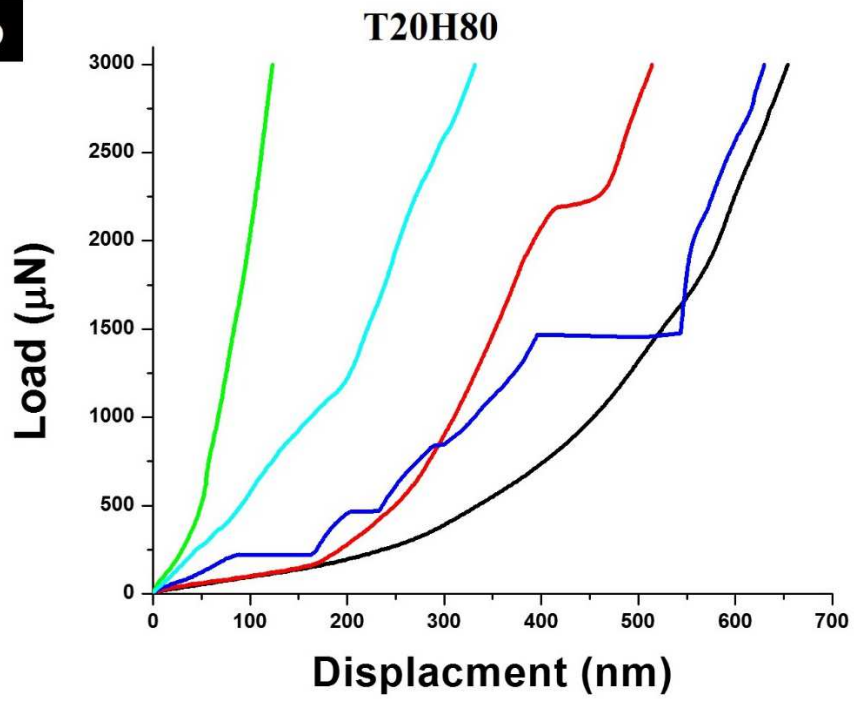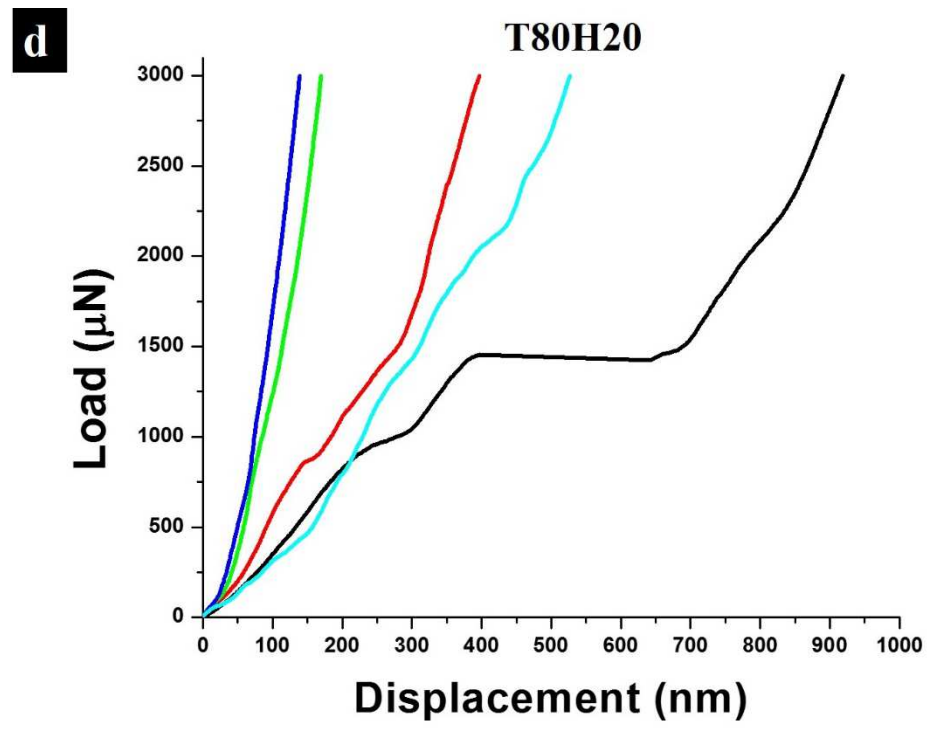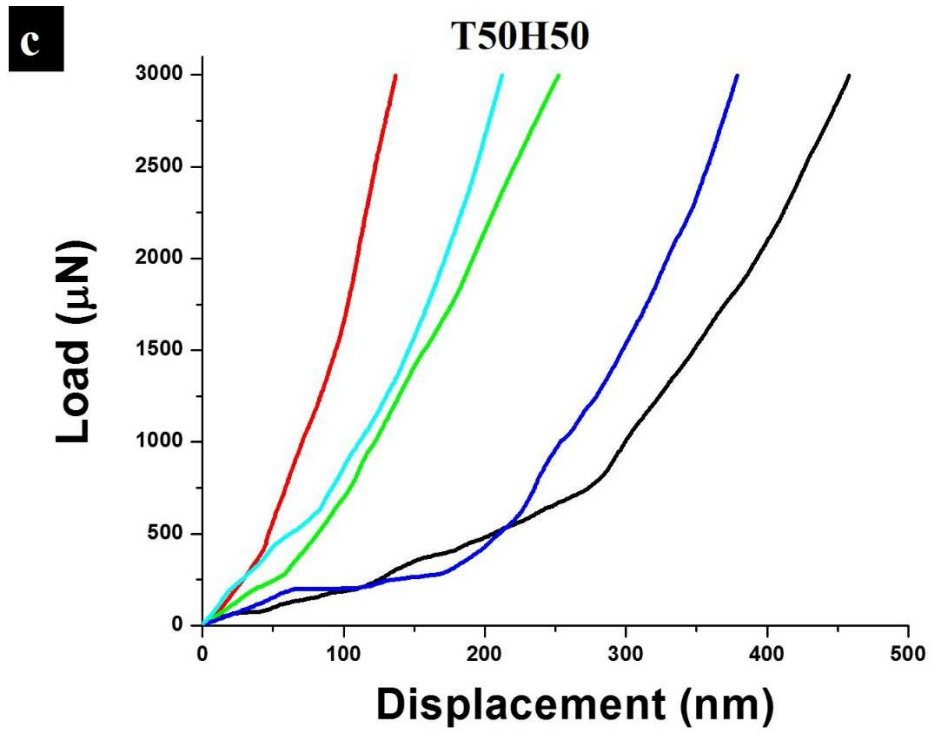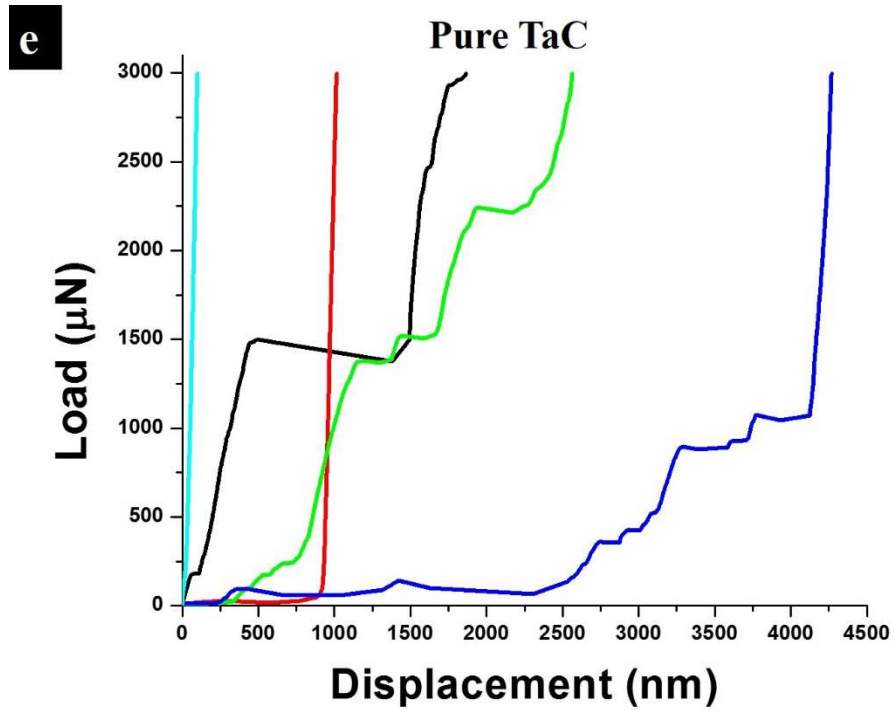
Figure 4.31: Representative loading segments of post-oxidation samples: (a) pure HfC, (b) T20H80, (c) T50H50, (d) T20H80, and (e) pure TaC

Table 4.4: Average nano-indentation displacement on the top surface of the oxide layer

Sample	Pure HfC	T20H80	T50H50	T80H20	Pure TaC
Depth (nm)	1526.3±1203.0	316.0±167.5	294.5±105.4	354.7±308.7	1176.5±1032.8

Chapter V Summary

The present study investigated the synthesis of TaC-HfC solid solutions by spark plasma sintering method. Five compositions were chosen: pure HfC, 80 vol.% HfC-20 vol.% TaC, 50 vol.% HfC- 50 vol.% TaC, 20 vol.% HfC- 80 vol.% TaC, and pure TaC. Major conclusions are listed below:

- The solid solutions were formed in all composition after sintering. The lattice parameters for the solid solution samples were calculated by the XRD analysis, and the results provided an excellent match with theoretical values according to the Vegard's Law.

- No phase transformation occurred after ball milling of the powders. The ball milling in the present study was solely used for breaking agglomeration of the powders.

- Nearly fully dense samples were achieved by spark plasma sintering with the peak temperature of 1850 $^{\circ}$C, 60 MPa pressure, and 10 min holding time without any sintering aids.

- The porosity in pure TaC samples was caused by the oxygen contamination (Ta_2O_5) on the starting powder surface. Due to low melting point (1872 $^{\circ}$C) of Ta_2O_5, liquid phase formation was observed in the pure TaC samples.

- In HfC-TaC samples, the oxygen contamination from the TaC surface was transferred to the HfC surface by the reaction between HfC and Ta_2O_5 and formed ultrafine HfO_2 particles. No sign of liquid phase was spotted in the HfC samples due to the much higher melting point of HfO_2.

- Significant grain growth was observed in the pure TaC and TaC-rich solid solution samples. The final grain sizes were measured at 6.8 and 6.2 µm, respectively. With the increase of HfC concentration, grain growth was hindered, and the grain size was reduced by 50% from T80H20 to T20H80 sample.

- The elastic moduli, hardness and fracture toughness of the solid solution samples outperformed the pure carbides samples partially due to the increased densification and smaller grain size.

- The solid solution samples showed improved oxidation resistance as compared to the pure carbides samples. The thickness of the oxide scales in T50H50 samples was 90% and 85% lower compared to the one in pure TaC and pure HfC, respectively.

- The oxidation process under the extreme conditions was governed by the availability of the oxygen, not diffusion.

- Liquid phase and solid scaffold structures were formed in all solid solution post oxidation samples. The liquid phase protected the underlying carbides from exposing to the oxygen, while the solid scaffold anchored the liquid phase and guaranteed the integrity of the oxide scales.

- The molten Ta_2O_5 attacked the un-oxidized carbides and promoted the oxidation process.

- A new phase, $Hf_6Ta_2O_{17}$, was formed from the reaction between HfO_2 and Ta_2O_5, and it was responsible for the exceptional oxidation resistance in the solid solution samples.

The present work has proven the feasibility of achieving fully dense solid solutions of carbides without sintering aids by spark plasma sintering. The oxidation studies conducted using high speed and high temperature plasma jet exhibited better oxidation resistance in solid solution samples than their constituent carbides. It also suggests that the key to the superior oxidation resistance is to form a liquid + solid scaffold structure in the oxide scales. The $Hf_6Ta_2O_{17}$ and HfO_2 combination in this case showed the promising oxidation performance. This work provides a guideline for screening the candidate materials for use on the hypersonic vehicles that require to survive under the extreme conditions.

Chapter VI Future Work and Recommendation

The present work shows the great potential of TaC-HfC solid solutions being used on the next generation space vehicles. Especially the T50H50 solid solution displayed the exceptional oxidation resistance. Spark plasma sintering is also proven as an effective method for synthesizing the solid solution samples. Based on the current work, the author believes some further studies are needed in the following aspects.

6.1 Powder Treatment and Sintering Parameters

The current sintering conditions resulted in near full densification samples without the sintering aids additions. The porosity came from the oxygen contamination on the starting powders. Better powder treatment is needed to remove such oxygen contamination in order to achieve denser samples. The TEM analysis on the sintered samples suggested the solid solution formation was not completed, so some adjustment on the sintering parameters is required. Higher sintering temperature and longer hold time will be the starting point.

6.2 Study on the Different Solid Solution Compositions and Possible Additives.

The T50H50 samples were the best performing solid solution in the current study, more comprehensive study is required to predict the optimum composition. Based on the present results, the composition range should be focused from T80H20 to T20H80. In the present work, no sintering aids were added. This is because the addition of sintering aids

would introduce the secondary phases and increase the complexity of the system, which prohibits the truly understanding of the oxidation behaviors of the solid solution samples. However, after thorough studies, additives is again an effective way to improve the oxidation resistance of the solid solutions. Due to the high melting point of Ta_2O_5, no liquid phase would generate when the temperature under 1850 °C. The additives such as B_4C and SiC are expected to form liquid phase in the lower temperature range, so that the solid solution samples would have better oxidation resistance.

6.3 Lower Temperature Oxidation Study

The promising oxidation performances of the solid solution samples were mainly due to the liquid phase formation, included Ta_2O_5 and $Hf_6Ta_2O_{17}$. The presence of such liquid phase would not be possible if the testing temperature is lower than the melting point of Ta_2O_5, which is around 1850 °C. In the lower temperature oxidation studies, the solid solution samples are expected to behave differently than in the present study. So it is crucial to understand the oxidation behaviors of the solid solutions under the lower temperature conditions.

6.4 Mechanical and Reusability Evaluation after Oxidation

After entering the Earth orbit, the reentry vehicles would still travel at high speed. So the materials for the reentry vehicles should be able to remain intact in order to withstand the strong shear force and possible impact from the loose particles. Also, in the cost perspective, reusable materials are highly welcomed. The present work has assessed

the reusability of the post-oxidation samples using nano-indentation technique. The results indicated the oxide scales in T50H50 samples owned superior integrity.

To further understand the deformation behaviors of the oxide scales, higher load indentation technique is needed. In our previous studies, we developed an in-situ high load indentation technique that can be used to evaluate the reusability. The testing setup is shown in Figure 6.1. The indentation is carried out inside a SEM. A linear, screw driven micro-load frame attached a 1 µm; 120° conospherical tip was employed for the indentation testing. The test will be monitored by SEM, and a real-time video is recorded. The reusability will be assessed by analyzing the size of the total impact area, and the deformation behavior.

Besides from the evaluation on the mechanical properties of the post-oxidation samples, repeated oxidation testing is also desired on T50H50 oxidized samples to estimate the lifespan of this solid solution sample. Combining the results from both mechanical and repeated oxidation testing, we will be able to get the full picture of the reusability of the solid solution samples.
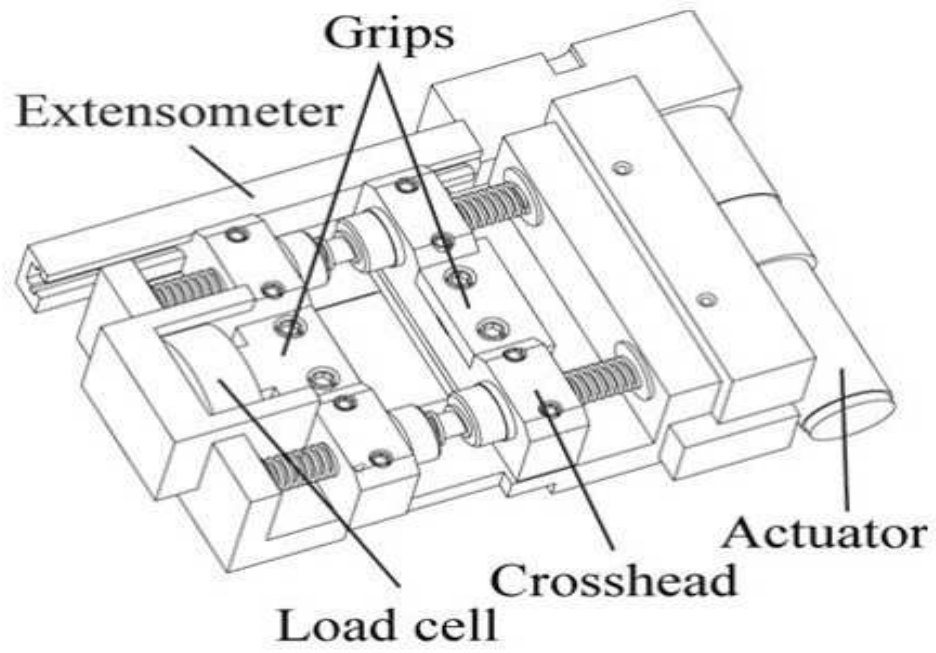
Figure 6.1: High load in-situ indention setup

REFERENCE

[1] E.J.W. W. G. Fahrenholtz, W. E. Lee, Y. Zhou, John Wiley & Sons, Inc., Hoboken, New Jeresey, 2014.

[2] L.E. Louis, Transition Metal Carbides and Nitrides, Academic Press, New York, 1971.

[3] J.Y. K. Upadhya, W. P. Hoffman. , Am. Ceram. Soc. Bull., 76 (1997) 51-56.

[4] M.M. Opeka, I.G. Talmy, J.A. Zaykoski, Journal of Materials Science, 39 (2004) 5887-5904.

[5] H.O. Pierson, Handbook of refractory carbides and nitrides, William Andrew Publishing, Westwood, NJ, 1996.

[6] L. Silvestroni, D. Sciti, Adv Mater Sci Eng, (2010).

[7] S.A. Ghaffari, M.A. Faghihi-Sani, F. Golestani-Fard, M. Nojabayy, International Journal of Refractory Metals & Hard Materials, 41 (2013) 180-184.

[8] O. Gaballa, B.A. Cook, A.M. Russell, International Journal of Refractory Metals & Hard Materials, 41 (2013) 293-299.

[9] O. Cedillos-Barraza, S. Grasso, N. Al Nasiri, D.D. Jayaseelan, M.J. Reece, W.E. Lee, Journal of the European Ceramic Society, 36 (2016) 1539-1548.

[10] S.A. Ghaffari, M.A. Faghihi-Sani, F. Golestani-Fard, S. Ebrahimi, Ceramics International, 39 (2013) 1985-1989.

[11] S.A. Ghaffari, M.A. Faghihi-Sani, F. Golestani-Fard, H. Mandal, Journal of the European Ceramic Society, 33 (2013) 1479-1484.

[12] H.A.Z.t.P. C. Agte, 11 (1930).

[13] A.A. Lavrentyev, B.V. Gabrelian, V.B. Vorzhev, I.Y. Nikiforov, O.Y. Khyzhun, J.J. Rehr, Journal of Alloys and Compounds, 462 (2008) 4-10.

[14] M. DesmaisonBrut, N. Alexandre, J. Desmaison, Journal of the European Ceramic Society, 17 (1997) 1325-1334.

[15] X. Zhang, G.E. Hilmas, W.G. Fahrenholtz, Journal of the American Ceramic Society, 91 (2008) 4129-4132.

[16] Y.J. Wang, H.J. Li, Q.G. Fu, H. Wu, L. Liu, C. Sun, Ceramics International, 39 (2013) 359-365.

[17] A. Paul, J.G.P. Binner, B. Vaidhyanathan, A.C.J. Heaton, P.M. Brown, J Microsc-Oxford, 250 (2013) 122-129.

[18] A. Nieto, D. Lahiri, A. Agarwal, Materials Science and Engineering a-Structural Materials Properties Microstructure and Processing, 582 (2013) 338-346.

[19] A. Lashtabeg, M. Smart, D. Riley, A. Gillen, J. Drennan, Journal of Materials Science, 48 (2013) 258-264.

[20] A. Nisar, S. Ariharan, T. Venkateswaran, N. Sreenivas, K. Balani, Corrosion Science, 109 (2016) 50-61.

[21] N.B.E. A. Metcalfe, in: U.S.P.A. Publication (Ed.), USA, 2006.

[22] G.R. Holcomb, G.R. Stpierre, Oxid Met, 40 (1993) 109-118.

[23] A. Sayir, Journal of Materials Science, 39 (2004) 5995-6003.

[24] K. Marnoch, J. Met. , (1965) 1225.

[25] R. Savino, M.D.S. Fumo, L. Silvestroni, D. Sciti, Journal of the European Ceramic Society, 28 (2008) 1899-1907.

[26] A. Paul, J.G. Binner, B. Vaidhyanathan, A.C. Heaton, P.M. Brown, J Microsc, 250 (2013) 122-129.

[27] A. Nieto, A. Kumar, D. Lahiri, C. Zhang, S. Seal, A. Agarwal, Carbon, 67 (2014) 398-408.

[28] I.M.V. G. V. Samsonov, Handbook of Refractory Compounds, IFI/Plenum Data Company, 1980.

[29] X. Zhang, G.E. Hilmas, W.G. Fahrenholtz, Journal of the American Ceramic Society, 91 (2008) 4129-4132.

[30] L.M. Liu, F. Ye, Z.G. Zhang, Y. Zhou, Materials Science and Engineering a-Structural Materials Properties Microstructure and Processing, 529 (2011) 479-484.

[31] S.R. Bakshi, V. Musaramthota, D.A. Virzi, A.K. Keshri, D. Lahiri, V. Singh, S. Seal, A. Agarwal, Materials Science and Engineering a-Structural Materials Properties Microstructure and Processing, 528 (2011) 2538-2547.

[32] L. Charpentier, M. Balat-Pichelin, D. Sciti, L. Silvestroni, Journal of the European Ceramic Society, 33 (2013) 2867-2878.

[33] D. Lahiri, V. Singh, G.R. Rodrigues, T.M.H. Costa, M.R. Gallas, S.R. Bakshi, S. Seal, A. Agarwal, Acta Materialia, 61 (2013) 4001-4009.

[34] J.A. Costello, I.S.T. Tsong, R.E. Tressler, American Ceramic Society Bulletin, 59 (1980) 356-356.

[35] J.A. Costello, I.S.T. Tsong, R.E. Tressler, American Ceramic Society Bulletin, 59 (1980) 828-828.

[36] Y. Laukhe, Y.M. Tairov, V.F. Tsvetkov, F. Shchepanski, Inorganic Materials, 17 (1981) 177-179.

[37] J.A. Costello, R.E. Tressler, Journal of the American Ceramic Society, 64 (1981) 327-331.

[38] A. Suzuki, H. Ashida, N. Furui, K. Mameno, H. Matsunami, Japanese Journal of Applied Physics Part 1-Regular Papers Short Notes & Review Papers, 21 (1982) 579-585.

[39] P.A. Ivanov, V.E. Chelnokov, Semiconductor Science and Technology, 7 (1992) 863-880.

[40] R.W. Newman, J Hopkins Apl Tech D, 14 (1993) 24-28.

[41] B. Hornetz, H.J. Michel, J. Halbritter, Journal of Materials Research, 9 (1994) 3088-3094.

[42] E.J. Opila, Journal of the American Ceramic Society, 77 (1994) 730-736.

[43] R. Riedel, H.J. Kleebe, H. Schonfelder, F. Aldinger, Nature, 374 (1995) 526-528.

[44] L. Ogbuji, E.J. Opila, Journal of the Electrochemical Society, 142 (1995) 925-930.

[45] E.J. Opila, R.E. Hann, Journal of the American Ceramic Society, 80 (1997) 197-205.

[46] D.R. Clarke, F.F. Lange, Journal of the American Ceramic Society, 63 (1980) 586-593.

[47] T. Hirai, K. Niihara, T. Goto, Journal of the American Ceramic Society, 63 (1980) 419-424.

[48] H.H. Du, R.E. Tressler, K.E. Spear, Journal of the Electrochemical Society, 136 (1989) 3210-3215.

[49] T. Narushima, T. Goto, T. Hirai, Y. Iguchi, Materials Transactions Jim, 38 (1997) 821-835.

[50] A. Rendtel, H. Hubner, M. Herrmann, C. Schubert, Journal of the American Ceramic Society, 81 (1998) 1109-1120.

[51] H. Park, H.W. Kim, H.E. Kim, Journal of the American Ceramic Society, 81 (1998) 2130-2134.

[52] F.S.S. Chien, J.W. Chang, S.W. Lin, Y.C. Chou, T.T. Chen, S. Gwo, T.S. Chao, W.F. Hsieh, Applied Physics Letters, 76 (2000) 360-362.

[53] R. Raj, L.N. An, S. Shah, R. Riedel, C. Fasel, H.J. Kleebe, Journal of the American Ceramic Society, 84 (2001) 1803-1810.

[54] K. Houjou, K. Ando, S.P. Liu, S. Sato, Journal of the European Ceramic Society, 24 (2004) 2329-2338.

[55] X.M. Li, X.W. Yin, L.T. Zhang, L.F. Cheng, Y.C. Qi, Materials Science and Engineering a-Structural Materials Properties Microstructure and Processing, 500 (2009) 63-69.

[56] M.M. Opeka, I.G. Talmy, E.J. Wuchina, J.A. Zaykoski, S.J. Causey, Journal of the European Ceramic Society, 19 (1999) 2405-2414.

[57] E.J. Wuchina, M.M. Opeka, Elec Soc S, 99 (2000) 477-488.

[58] R. Savino, M. De Stefano Fumo, L. Silvestroni, D. Sciti, Journal of the European Ceramic Society, 28 (2008) 1899-1907.

[59] D. Sciti, L. Silvestroni, S. Guicciardi, D.D. Fabbriche, A. Bellosi, Journal of Materials Research, 24 (2009) 2056-2065.

[60] W.G. Fahrenholtz, G.E. Hilmas, I.G. Talmy, J.A. Zaykoski, Journal of the American Ceramic Society, 90 (2007) 1347-1364.

[61] T.A. Parthasarathy, R.A. Rapp, M. Opeka, R.J. KeranS, Acta Materialia, 55 (2007) 5999-6010.

[62] W.G. Fahrenholtz, G.E. Hilmas, International Materials Reviews, 57 (2012) 61-72.

[63] R. Licheri, C. Musa, R. Orru, G. Cao, D. Sciti, L. Silvestroni, Journal of Alloys and Compounds, 663 (2016) 351-359.

[64] V.Z. Poilov, E.N. Pryamilova, Russian Journal of Inorganic Chemistry, 61 (2016) 55-58.

[65] E.P. Simonenko, D.V. Sevast'yanov, N.P. Simonenko, V.G. Sevast'yanov, N.T. Kuznetsov, Russian Journal of Inorganic Chemistry, 58 (2013) 1669-1693.

[66] W.G. Fahrenholtz, Journal of the American Ceramic Society, 90 (2007) 143-148.

[67] I.G. Talmy, J.A. Zaykoski, M.M. Opeka, Journal of the American Ceramic Society, 91 (2008) 2250-2257.

[68] D.J. Chen, W.J. Li, X.H. Zhang, P. Hu, J.C. Han, C.Q. Hong, W.B. Han, Materials Chemistry and Physics, 116 (2009) 348-352.

[69] D.J. Chen, L. Xu, X.H. Zhang, B.X. Ma, P. Hu, International Journal of Refractory Metals & Hard Materials, 27 (2009) 792-795.

[70] T.A. Parthasarathy, R.A. Rapp, M. Opeka, M.K. Cinibulk, Journal of the American Ceramic Society, 95 (2012) 338-349.

[71] A. Ortona, P. Fino, C. D'Angelo, S. Biamino, G. D'Amico, D. Gaia, S. Gianella, Ceramics International, 38 (2012) 3243-3250.

[72] F. Monteverde, D. Alfano, R. Savino, Corrosion Science, 75 (2013) 443-453.

[73] C.A. Wang, M.F. Wang, Frontiers of Materials Science, 7 (2013) 184-189.

[74] K. Shugart, B. Patterson, D. Lichtman, S.Y. Liu, E. Opila, Journal of the American Ceramic Society, 97 (2014) 2279-2285.

[75] W. Tan, K. Li, H. Li, J. Zhang, C. Ni, A. Cao, C. Ma, Vacuum, 116 (2015) 124-129.

[76] L. Pienti, L. Silvestroni, E. Landi, C. Melandri, D. Sciti, Ceramics International, 41 (2015) 1367-1377.

[77] K. Shugart, E. Opila, Journal of the American Ceramic Society, 98 (2015) 1673-1683.

[78] A.K. Georgiev, M.A. Misheva, G.H. Toumbev, Dokladi Na Bolgarskata Akademiya Na Naukite, 38 (1985) 1141-1143.

[79] S. Takahashi, T. Sato, K. Shimakage, Denki Kagaku, 63 (1995) 140-146.

[80] A.G. Metcalfe, N.B. Elsner, D.T. Allen, E. Wuchina, M. Opeka, E. Opila, Oxidation of hafnium diboride, 2000.

[81] N. Richet, P. Lespade, P. Goursat, E. Laborde, Oxidation resistance of HfB2-SiC coatings for protection of carbon fiber based composites, in: H. Mandal, L. Ovecoglu (Eds.) Euro Ceramics Viii, Pts 1-3, 2004, pp. 1047-1050.

[82] F. Monteverde, L. Scatteia, Journal of the American Ceramic Society, 90 (2007) 1130-1138.

[83] P. Lespade, N. Richet, P. Goursat, Acta Astronautica, 60 (2007) 858-864.

[84] R. Licheri, R. Orru, C. Musa, A.M. Locci, G. Cao, Journal of Alloys and Compounds, 478 (2009) 572-578.

[85] X.H. Zhang, L. Weng, J. Han, S.H. Meng, W.B. Han, International Journal of Applied Ceramic Technology, 6 (2009) 134-144.

[86] C.F. Hu, Y. Sakka, B. Jang, H. Tanaka, T. Nishimura, S.Q. Guo, S. Grasso, Journal of the Ceramic Society of Japan, 118 (2010) 997-1001.

[87] D. Sciti, V. Medri, L. Silvestroni, Scripta Mater, 63 (2010) 601-604.

[88] D.W. Ni, G.J. Zhang, Y.M. Kan, P.L. Wang, Int J Appl Ceram Tec, 7 (2010) 830-836.

[89] L. Weng, W. Han, C. Hong, Materials Science-Poland, 29 (2011) 248-252.

[90] D.W. Ni, G.J. Zhang, F.F. Xu, W.M. Guo, Scripta Mater, 64 (2011) 617-620.

[91] M. Mallik, K.K. Ray, R. Mitra, Journal of the European Ceramic Society, 31 (2011) 199-215.

[92] D.W. Ni, J.X. Liu, G.J. Zhang, Journal of the European Ceramic Society, 32 (2012) 3627-3635.

[93] M. Mallik, A.J. Kailath, K.K. Ray, R. Mitra, Journal of the European Ceramic Society, 32 (2012) 2545-2555.

[94] R.K. Enneti, M.G. Bothara, S.J. Park, S.V. Atre, Ceramics International, 38 (2012) 4369-4372.

[95] E. Zapata-Solvas, D.D. Jayaseelan, H.T. Lin, P. Brown, W.E. Lee, Journal of the European Ceramic Society, 33 (2013) 1373-1386.

[96] C.M. Carney, T.A. Parthasarathy, M.K. Cinibulk, International Journal of Applied Ceramic Technology, 10 (2013) 293-300.

[97] H.J. Li, D.J. Yao, Q.G. Fu, L. Liu, Y.L. Zhang, X.Y. Yao, Y.J. Wang, H.L. Li, Carbon, 52 (2013) 418-426.

[98] C.J. Leslie, E.E. Boakye, K.A. Keller, M.K. Cinibulk, DEVELOPMENT OF CONTINUOUS SiC FIBER REINFORCED HfB2-SiC COMPOSITES FOR AEROSPACE APPLICATIONS, in: N.P. Bansal, J.P. Singh, S.W. Ko, R.H.R. Castro, G. Pickrell, N.J. Manjooran, K.M. Nair, G. Singh (Eds.) Processing and Properties of Advanced Ceramics and Composites V, 2013, pp. 3-12.

[99] V.G. Sevastyanov, E.P. Simonenko, A.N. Gordeev, N.P. Simonenko, A.F. Kolesnikov, E.K. Papynov, O.O. Shichalin, V.A. Avramenko, N.T. Kuznetsov, Russian Journal of Inorganic Chemistry, 59 (2014) 1361-1382.

[100] V.G. Sevastyanov, E.P. Simonenko, A.N. Gordeev, N.P. Simonenko, A.F. Kolesnikov, E.K. Papynov, O.O. Shichalin, V.A. Avramenko, N.T. Kuznetsov, Russian Journal of Inorganic Chemistry, 59 (2014) 1298-1311.

[101] D.L. Hu, Q. Zheng, H. Gu, D.W. Ni, G.J. Zhang, Journal of the European Ceramic Society, 34 (2014) 611-619.

[102] V.G. Sevastyanov, E.P. Simonenko, A.N. Gordeev, N.P. Simonenko, A.F. Kolesnikov, E.K. Papynov, O.O. Shichalin, V.A. Avramenko, N.T. Kuznetsov, Russian Journal of Inorganic Chemistry, 60 (2015) 1360-1373.

[103] D.V. Grashchenkov, O.Y. Sorokin, Y.E. Lebedeva, M.L. Vaganova, Russian Journal of Applied Chemistry, 88 (2015) 386-393.

[104] C.M. Carney, T.S. Key, COMPARISON OF THE OXIDATION PROTECTION OF HfB2 BASED ULTRA-HIGH TEMPERATURE CERAMICS BY THE ADDITION OF SiC OR MoSi2, 2015.

[105] C.J. Leslie, E.E. Boakye, K.A. Keller, M.K. Cinibulk, International Journal of Applied Ceramic Technology, 12 (2015) 235-244.

[106] R.E.B. N. B. Pilling, J. Inst. Met. , 29 (1923) 529-591.

[107] D. Sciti, L. Silvestroni, S. Guicciardi, D.D. Fabbriche, A. Bellosi, Journal of Materials Research, 24 (2011) 2056-2065.

[108] E.L. Courtright, J.T. Prater, G.R. Holcomb, G.R. Stpierre, R.A. Rapp, Oxid Met, 36 (1991) 423-437.

[109] C.B. Bargeron, R.C. Benson, A.N. Jette, T.E. Phillips, Journal of the American Ceramic Society, 76 (1993) 1040-1046.

[110] S. Shimada, M. Inagaki, K. Matsui, Journal of the American Ceramic Society, 75 (1992) 2671-2678.

[111] S. Shimada, K. Nakajima, M. Inagaki, Journal of the American Ceramic Society, 80 (1997) 1749-1756.

[112] C. Verdon, O. Szwedek, A. Allemand, S. Jacques, Y. Le Petitcorps, P. David, Journal of the European Ceramic Society, 34 (2014) 879-887.

[113] D.L. Deadmore, NASA Technical Note, (1964).

[114] S.H. M. C. L. Patterson, and L. L. Fehrenbacher, Mater. Manuf. Process. , 11 (1996) 367-379.

[115] M. Patterson, NASA report, (1999).

[116] Y.L. Wang, X. Xiong, G.D. Li, H.F. Liu, Z.K. Chen, W. Sun, X.J. Zhao, Corrosion Science, 66 (2013) 177-182.

[117] C.F. Hu, L.F. He, F.Z. Li, L. Wu, J.Y. Wang, M.S. Li, Y.W. Bao, Y.C. Zhou, L.F. He, F.Z. Li, L. Wu, International Journal of Applied Ceramic Technology, 7 (2010) 697-703.

[118] Y.J. Wang, H.J. Li, Q.G. Fu, H. Wu, D.J. Yao, H.L. Li, Surface & Coatings Technology, 206 (2012) 3883-3887.

[119] Y.-l. Wang, X. Xiong, X.-j. Zhao, G.-d. Li, Z.-k. Chen, W. Sun, Corrosion Science, 61 (2012) 156-161.

[120] P.C. G. R. Anstis, B. R. Lawn, D. B. Marschall, J. Am. Ceram. Soc. , 64 (1981) 533-538.

[121] J.-M. Ting, R.Y. Lin, Journal of Materials Science, 29 (1994) 1867-1872.

[122] J.P. Kelly, O.A. Graeve, Acta Materialia, 84 (2015) 472-483.

[123] R.C. Bradt, J. Am. Ceram. Soc., 50 (1966).

[124] A.H.H. A. Domingues-Rodriguez, Surf. Interf. Ceram. Mater. , 173 (1988) 761-776.

[125] H.P.L. J. Wang, R. Stevens, J. Mater. Sci. , 7 (1992) 5397-5430.

[126] C. Zhang, B. Boesl, L. Silvestroni, D. Sciti, A. Agarwal, Materials Science and Engineering: A, 674 (2016) 270-275.

Appendix 1: Elemental identification on the ultrafine particles

The EDS mapping and point analysis results suggested that the ultrafine particles (point 1) were mainly HfO_2 and shown in Figure A1.
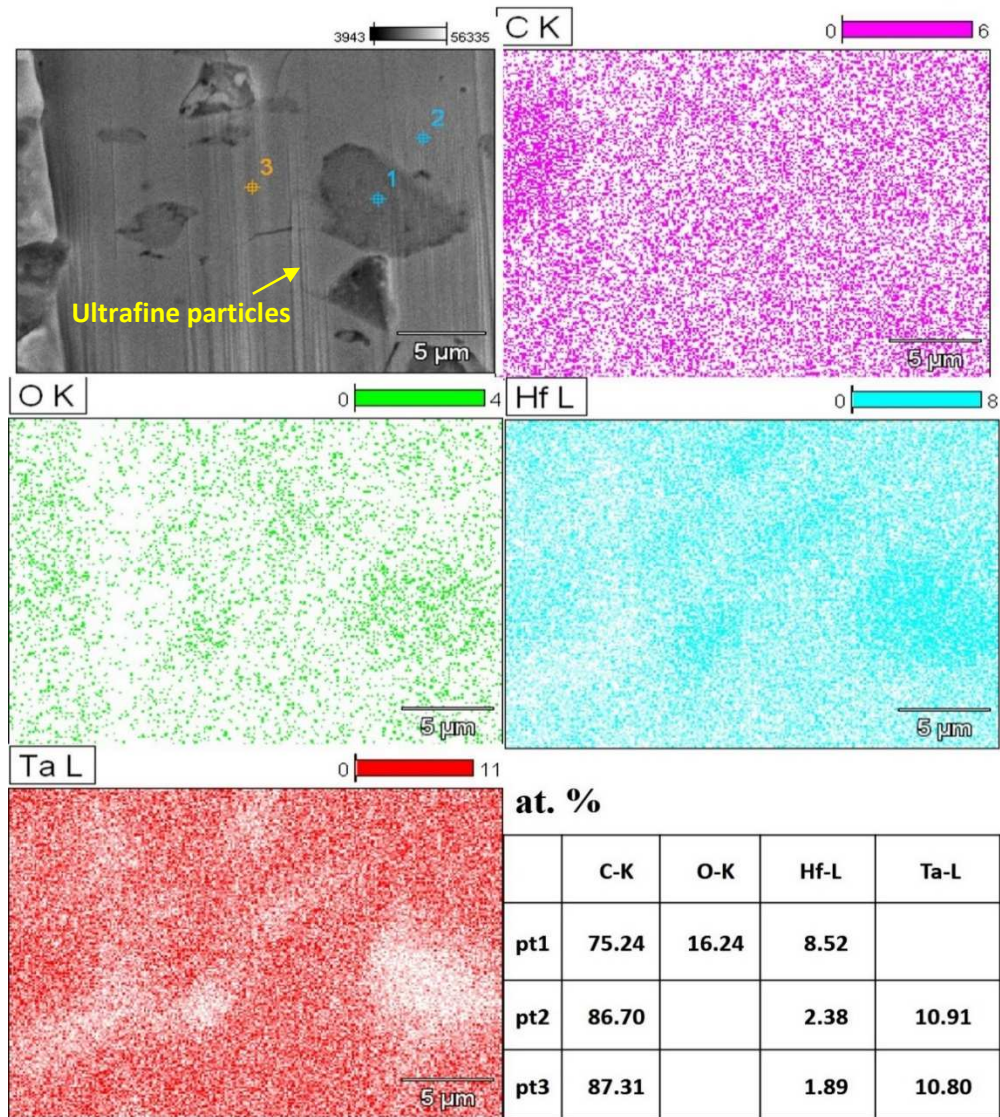

Fig. A1. EDS mapping and point analysis on the ultrafine particles from the FIB sectioned surface.

Appendix 2: The enthalpies of mixing calculations for the three solid solutions formation

The enthalpy of mixing (ΔH_{mix}) was calculated as the enthalpy difference between the products (solid solution) and the reactants (TaC and HfC). The enthalpies of the reactants were taken as the formation enthalpy of TaC and HfC, as shown below: [28]

H_{TaC} =-38497 + 1.332T (Cal/mol), T: 298-3000K;

H_{HfC} =-48500 + 3.262T (Cal/mol), T: 298-2600K.

The temperature T was taken as the sintering temperature 1850 ℃, 2123 K. Given the molecular weight of TaC and HfC are 192.96 g/mol and 190.5 g/mol respectively, and total powder weight was 15 g. The enthalpies of formations for 3 mixed carbides samples were tabulated in Table A1.

The enthalpies of products were calculated by using the bonding energies of TaC and HfC. The bonding energies of TaC and HfC are 16.92 eV and 16.45 eV respectively. [5] The enthalpies of three mixed carbides samples were also summarized in Table A1.

Table A1: Enthalpies of mixing calculations for T80H20, T50H50, and T20H80

Unit: kJ	$H_{products}$	$H_{reactants}$	ΔH_{mix}
T80H20	126.95	-12.06	139.01
T50H50	126.36	-12.69	139.05
T20H80	125.78	-13.32	139.10

Appendix 3: Gibbs free energy calculation for the reaction between Ta_2O_5 and HfC

The Gibbs free energy of the reaction:

$$Ta_2O_5 + HfC = HfO_2 + TaC + CO$$

Was calculated by using Factsage software:

$$\Delta G \ (kJ) = -0.14T - 759.76 \qquad T: 500\text{-}2000 \ ^oC$$

It is negative for the temperature range of present study, hence the above reaction was feasible during the SPS process.

VITA

CHENG ZHANG

EDUCATION:

Sept. 2006 – May 2010   Bachelor of Science (B.S.) in Materials Science and Engineering, East China University of Science and Technology, Shanghai, China

Sept. 2010 – May 2012   Master of Science (M.S.) in Materials Science and Engineering, Florida International University, Miami, FL

Jan. 2014 – Dec. 2016   Doctoral Candidate (Ph.D) in Materials Science and Engineering, Florida International University, Miami, FL

PUBLICATIONS AND PRESENTATION:

1. Cheng Zhang, B. Boesl, L. Silvestrioni, D. Sciti, and A.Agarwal. Deformation Mechanism in Graphene Nanoplatelet Reinforced Tantalum Carbide using High Load In situ Indentation. *Mater. Sci. Eng.: A*, **674**(2016): 270-275.

2. P. Nautiyal, C. Rudolf, A. Loganathan, Cheng Zhang, B. Boesl, and A. Agarwal. Directionally Aligned Ultra-Long Boron Nitride Nanotube Induced Strengthening of Aluminum-Based Sandwich Composite. *Adv. Eng. Mater.*, DOI: 10.1002/adem.201600212.

3. D. Ward, A. Gupta, S. Saraf, Cheng Zhang, T.S. Sakthivel, S. Barkam, A. Agarwal, and S. Seal. Functional NiAl-graphene Oxide Composite as a Model Coating for Aerospace Component Repair. *Carbon*, **105**(2016): 529-543.

4. Cheng Zhang, A. Nieto, and A. Agarwal. Ultrathin Graphene Tribofilm Formation During Wear of Al2O3-Graphene Nanoplatelet Composites. *Nanomaterials and Energy*, **5**(2016): 1-9.

5. A. Nieto, R. Dua, Cheng Zhang, S. Ramaswamy, B. Boesl, and A. Agarwal. Three Dimensional Graphene Foam/Polymer Hybrid as a High Strength Biocompatible Scaffold. *Adv. Funct. Mater.*, **25**(2015): 3916-3924.

6. M. Lordeus, A. Estrada, D. Stewart, R. Dua, Cheng Zhang, A. Agarwal, and S. Ramaswamy. Graphene Nanoplatelet Reinforced Silicone for the Valvular Prosthesis Application. *J. Long-term Eff. Med.*, **25**(2015): 95-103.

7. D. Lahiri, J. karp, A.K. Keshri, <u>Cheng Zhang</u>, G.S Dulikravich, L.J. Kecskes, and A. Agarwal. Scratch Induced Deformation Behavior of Hafnium Based Bulk Metallic Glass at Multiple Load Scales. *J. Non-Cryst. Solids*, **410**(2015): 118-126.

8. D. Lahiri, F. Hec, M. Thiesse, A. Durygin, <u>Cheng Zhang</u>, and A. Agarwal. Nanotribological Behavior of Graphene Nanoplatelet Reinforced Ultrahigh Molecular Weight Polyethylene Composites. *Tribo. Inter.*, **70**(2014): 165-169.

9. A. Nieto, A. Kumar, D. Lahiri, <u>Cheng Zhang</u>, S. Seal, and Arvind Agarwal. Oxidation Behavior of Graphene Nanoplatelet Reinforced Tantalum Carbide Composites in High Temperature Plasma Flow. *Carbon* **67**(2014): 398-408.

10. S. B. Pitchuka, B. Boesl, <u>Cheng Zhang</u>, D. Lahiri, A. Nieto, G. Sundararajan, and A. Agarwal. Dry Sliding Wear of Sprayed Aluminum Amorphous/Nanocrystalline Alloy Coatings. *Surf. Coat. Techn.*, **238**(2014): 118-125.

11. <u>Cheng Zhang</u>, U. Chaudhary, D. Lahiri, A. Godavarty, and A. Agarwal, Photo-catalytic Activity of Spark Plasma Sintered TiO2-Graphene Nanoplatelet Composite *Scripta Materialia*, **68**(2013): 719-722.

12. <u>Cheng Zhang</u>, U. Chaudhary, S. Das, S. Thomas, and A. Agarwal, Effect of Porosity on Photocatalytic Activity of Plasma Sprayed TiO2 Coating. *J.Therm Spray Techn.*, **22**(2013): 1193-1200.

(List of 12 out of 17 journal articles, 1 more paper is under review in peer reviewed journals)

13. Oral presentation: A Study of the Mechanisms of Deformation in Graphene Nanoplatelet Reinforced Tantalum Carbide Using In Situ Indentation. Materials Science & Technology 2015, Columbus, OH.

(List of 1 out of 4 conference presentation, 2 more presentations will be given in Oct. 2016 at MS&T 2016, Salt Lake City, UT.)